Spectroscopy and Chemistry of Microperoxidases

Thesis by

Donald Low

In Partial Fulfillment of the Requirements
for the Degree of
Doctor of Philosophy

California Institute of Technology
Pasadena, California

Submitted May 9, 1997

© 1997
Donald W. Low
All Rights Reserved

Acknowledgement:

I remember a postdoc from my undergrad lab saying that if I went to Caltech to work for Harry Gray, I'd have a chance to work with *the* best people. I think if I knew where to find that postdoc now, I'd thank him and tell him that he was right. Of course, part of the package of best people that come with working for Harry is Harry himself. He's been a tremendous provider of support - moral and scientific. Jay Winkler has been a super co-advisor, and he and Harry together had most of the bases covered for me. And of course there are my friends and coworkers. When I first joined the group, there was a solid core of senior grad students and postdocs who showed me around the lab and provided an exciting atmosphere to work in. Staying up late working was fun, because I-Jy Chang, Mark McCleskey, Mike Hill, Julia Hodge and Debbie Wuttke were here working too. They were the role models who I looked up to when I was a young grad student, and I have to thank them for the many fun discussions of science and various other topics. Eva Birnbaum and Kara Bren were my fellow first-years, and I only wish that they could have stayed a little longer instead of leaving me in their dust, because things weren't quite the same after they left. Kara and I became great friends, and I'm happy to see her career off to an amazing start already (sniff sniff). I watched Eva and Mark's friendship grow into a beautiful marriage, and I consider them two very fortunate people. Jack Mizoguchi and I gladly ate a zillion free gourmet meals together (thanks Harry). Toshi Takeuchi and Yonchu Jenkins were my companions for many ski trips, tennis matches, movies and dinners out, and they are dear friends. I have to thank Julia for introducing me to mountain biking on that rainy day at Chantry Flat. Kevin Hoke and I have ridden hundreds if not a thousand miles together up in the San Gabriels, and I probably will never find a better biking buddy. Hans Nikol, Arnd Bottcher, Gary Mines and Bill Connick were parts of many fun moments that I won't forget. Sakena Abedin was the first undergraduate to work for me in the lab and she convinced me that I should stay and finish my degree. Chris Chang and Grace Yang did a fantastic job, and I'm very proud of them. Cindy Quezada tried her best to teach me how to dance and became a fellow X-Files addict. Jason Telford and Sonya Franklin shared many pleasant lunches with me at the Ath. Akif Tezcan never let me forget that it was my job as senior grad student to answer questions and showed me how to throw a mean hammer. Jens Duus was my excellent host and collaborator at Carlsberg in Denmark. Angelo Di Bilio introduced me to Buster's, and gave me some wise advice when I badly needed it. Finally, I can't forget to thank my dad. He may not know it, but he was the first scientist I ever knew. I remember him telling me when I was a very small child, that in theory, *anything is possible*. How true.

Dedication

My aunty tells me that my grandfather was a gambling sort. He liked nothing better than to place a wager on a game of cards. As a gambler, he certainly knew something about chance and luck, so surely he was pleased when my mother was born, his eighth child on the eighth day of the eighth month of the year. You see, to a Chinese person, the word for eight, *ba*, sounds like the word for luck, *fa*, and 3 eight's in a row is considered to be a *very* lucky thing indeed.

I've never quite figured out the puzzle of how my mother's side came to live in Tahiti, an island about as remote and removed from everywhere else as you can imagine, but that is where my mother was born and lived as a child. Most people would consider living in Tahiti very lucky indeed, since it is truly an island paradise, complete with clear blue lagoons, sandy white beaches and unspoilt tropical forests full of birds and animals (if you've never been there you should go). But something in my mother told her that there was more to the world than the confines of a tiny island home, and so she left her Polynesian life behind and came to America where she met my father and decided to settle down and raise a family.

Growing up here, she always made sure I had what I needed to do well in my studies, but she never made the mistake of being unrealistic. Most of the time, she just sent me off with a simple 'do your best.' I know she didn't understand all the things I did or why I did them, but she was always nothing but supportive of me. I owe her an enormous debt of gratitude; I consider myself lucky to have known her and been her son all these years, and my thesis is largely the product of her loving support and the values she instilled in me.

Table of Contents

Acknowledgement iii
Dedication - A Word on Luck iv
Table of Contents v
List of Tables vii
List of Figures viii
Abstract xi
Chapter 1: Heme Peroxidases and Cytochrome P450 1
Introduction 2
Peroxidases 2
Cytochrome P450 10
Research Overview 17
References and Notes 18
Chapter 2: Preparation, Purification and Characterization of Microperoxidases 21
Introduction 22
Experimental Section 24
Materials 24
Methods 24
Results and Discussion 42
Conclusion 48
References and Notes 49
Chapter 3: Paramagnetic NMR Spectroscopy of Microperoxidase-8 51
Introduction 52
Results and Discussion 52
Conclusion 84
Experimental Section 85
References and Notes 87
Chapter 4: Photo-initiated Oxidation of Microperoxidase-8, Cytochrome *c* Peroxidase and Myoglobins. Comparison of Oxidation Chemistries. 90
Introduction 91
Results and Discussion 97
Flash-Quench Oxidation of MP8 97
Flash-Quench Oxidation of CcP 112
Photo-induced Oxidation of Myoglobins 122
Comparisons of Results from Oxidation of Proteins and Models 126
References and Notes 128

Chapter 5: Covalent Modification of Microperoxidases by Reverse Proteolysis..... 131
Introduction..... 132
Experimental Section..... 134
Materials..... 134
Methods..... 135
General Peptide Coupling Reactions..... 135
Resonance Raman Spectroscopy..... 157
Miscellaneous..... 162
Results and Discussion..... 162
Peptide Chemistry - Preparation of X23 Microperoxidases..... 162
Addition of D-Amino Acids..... 165
Addition of Amino Acid Hydrazides..... 166
Intramolecular Ligand Binding in X23MP10's..... 167
UV-visible Spectroscopy..... 167
Resonance Raman Spectroscopy of X23 Microperoxidases..... 170
Conclusions..... 186
References and Notes..... 192
Chapter 6: Preparation, Spectroscopy and Electron Transfer Reactions of Manganese Microperoxidase-8..... 195
Introduction..... 196
Results and Discussion..... 196
Preparation and Characterization of apo-MP8 and MnMP8..... 196
Photo-initiated Oxidation of Mn(III)MP8..... 205
Conclusion..... 212
Experimental Section..... 213
References..... 215
Chapter 7: Resonance Raman Studies of Ferrous Carbonmonoxy Microperoxidase-8 and Cytochrome *c*..... 216
Introduction..... 217
Results and Discussion..... 219
Static Raman and UV-visible Spectroscopy of Fe(II)-CO MP8 and cyt *c*..... 219
Time-Resolved Measurements..... 224
Conclusions..... 232
Experimental Section..... 233
References..... 234

List of Tables

Chapter 3

Table 3.1: ^{1}H Chemical Shifts 56
Table 3.2: Comparison of Heme Methyl Proton Chemical Shifts 64
Table 3.3: Observed and Calculated Dipolar Shifts 76
Table 3.4: Selected ^{1}H Relaxation Times at 250 MHz 79
Table 3.5: Amide-H-Hα Coupling Constants 82
Table 3.6: NOE Contacts in MP8-CN 83

Chapter 6

Table 6.1: UV-vis Absorption Maxima for Mn-Substituted Heme Proteins 204
Table 6.2: Pseudo-First Order Rate Constants for Oxidation of MnMP8 211
Table 6.3: Bimolecular Rate Constants for Oxidation of MnMP8 211

List of Figures

Chapter 1

Figure 1.1: Catalytic Cycle of Cytochrome *c* Peroxidase 4
Figure 1.2: Crystal Structure of Cytochrome *c* Peroxidase 6
Figure 1.3: Crystal Structure of Cytochrome P450CAM 12
Figure 1.4: Mechanism for P450 Hydroxylations 15

Chapter 2

Figure 2.1: FPLC Purification of MP9 26
Figure 2.2: UV-vis Spectra of MP9 and MP8 28
Figure 2.3: MALDI Mass Spectrum of MP9 30
Figure 2.4: FPLC Purification of MP8 33
Figure 2.5: MALDI Mass Spectrum of MP8 35
Figure 2.6: FPLC Purification of Ac-MP8 38
Figure 2.7: MALDI Mass Spectrum of Ac-MP8 40
Figure 2.8: Low Temperature UV-Vis Spectrum of Ac-MP8 . . . 43
Figure 2.9: Magnetization Saturation Curves for Ac-MP8 and MP8-CN 45

Chapter 3

Figure 3.1: ^{1}H-NMR Spectrum of Ac-MP8 53
Figure 3.2: ^{1}H-NMR Spectra of MP8-CN 57
Figure 3.3: NOESY Spectrum of MP8-CN 59
Figure 3.4: Curie Plots for MP8-CN and Ac-MP8 62
Figure 3.5: HMQC Spectrum of MP8-CN 68
Figure 3.6: Heme Methyl ^{13}C Chemical Shifts 70
Figure 3.7: Structures of Cytochrome *c* and MP8 Fragment . . . 72
Figure 3.8: Orientation of the Magnetic Tensor in MP8-CN . . . 74
Figure 3.9: Magnitudes of Chi Based on the Magnetic Tensor 77
Figure 3.10: TOCSY Spectrum of MP8-CN 80

Chapter 4

Figure 4.1: Schematic of Nanosecond Experiments Table 95

Figure 4.2: Absorption Spectra of Ferric and Ferryl Ac-MP8 98
Figure 4.3: Single-wavelength Transient Absorption for the Oxidation of MP8 100
Figure 4.4: Soret Region Transient Absorption Spectra 103
Figure 4.5: Q-Band Region Transient Absorption Spectra 105
Figure 4.6: Dependence of Oxidation Rates on MP8 Concentration 108
Figure 4.7: UV-Visible Spectra of Cytochrome *c* Peroxidase . . . 114
Figure 4.8: Transient Absorption Spectrum of Oxidized Cytochrome *c* Peroxidase 116
Figure 4.9: Comparison Between CcP Oxidation and Ru(III) Decay Rates 118
Figure 4.10: Steady State Photooxidation of the EtSH form of H93G SW Mb 124

Chapter 5

Figure 5.1: FPLC Purification of H23MP10 137
Figure 5.2: MALDI Mass Spectrum of H23MP10 139
Figure 5.3: FPLC Purification of W23MP10 142
Figure 5.4: Fluorescence Spectrum of W23MP10 144
Figure 5.5: MALDI Mass Spectrum of W23MP10 146
Figure 5.6: FPLC Purification of M23MP10 149
Figure 5.7: MALDI Mass Spectrum of M23MP10 151
Figure 5.8: FPLC Purification of Y23MP10 153
Figure 5.9: MALDI Mass Spectrum of Y23MP10 155
Figure 5.10: FPLC Purification of γ23MP10 158
Figure 5.11: MALDI Mass Spectrum of γ23MP10 160
Figure 5.12: Calibration Curve for the SPEX 750 M Raman Monochromator 163
Figure 5.13: Titration of H23MP10 168
Figure 5.14: Titration of MP9 171
Figure 5.15: EPR Spectrum of H23MP10 Low pH Form 173
Figure 5.16: Titration of M23MP10 175
Figure 5.17: UV-vis Spectra of Reduced X23MP10 Peptides 177

Figure 5.18: Resonance Raman Spectra of H23MP10 at pH 7 and pH 2 180
Figure 5.19: Raman Spectra of Oxidized and Reduced Y23MP10 182
Figure 5.20: Raman Spectra of MP8 at pH 2 and pH 7 184
Figure 5.21: Q-Band Excited Raman Spectrum of H23MP10 . . . 187
Figure 5.22: Raman Spectrum of Reduced H23MP10 189

Chapter 6

Figure 6.1: UV-vis Spectrum of apo-MP8 198
Figure 6.2: Mass Spectra of apo-MP8 and MnMP8 200
Figure 6.3 UV-vis Spectra of Mn(III) and Mn(IV)=O MP8 . . . 202
Figure 6.4: Static and Transient Absorption Spectra of Mn(IV)=O MP8 207
Figure 6.5: Derivation of Second Order Rates Constants for Oxidation of MnMP8 209

Chapter 7

Figure 7.1: UV-vis Spectrum of Fe(II)-CO MP8 220
Figure 7.2: Raman Spectrum of Fe(II)-CO MP8 222
Figure 7.3: Static and Transient Raman Spectra of Fe(II)-CO MP8 226
Figure 7.4: Transient Absorption Spectra of Photolyzed Fe(II)-CO MP8 228
Figure 7.5: Static and Transient Raman Spectra of Photolyzed Fe(II)-CO Cytochrome *c* 230

Abstract

Microperoxidases (MP) fragments of horse cytochrome *c* (cyt *c*) were prepared and used as models for heme proteins. The spin state and electronic structure of the ferric heme octapeptide fragment (MP8) was investigated by NMR, EPR, UV-visible, resonance Raman and magnetic susceptibility methods. The heme iron is in equilibrium between S = 5/2 and S = 1/2 spin states. NMR studies on the ferric cyanide complex of MP8 indicates that residues 14-18 form a rigid structural motif in cyt *c* that is preserved in MP8. The imidazole of His18 is oriented along the α–γ meso axis of the heme in both MP8 and cyt *c*. The reactivity of ferric MP8 towards single-electron transfer oxidations was investigated by nanosecond flash-photolysis methods. Spectroscopic and kinetic evidence indicate that the MP8 porphyrin π cation radical is readily generated by oxidation with photochemically generated $Ru(bpy)_3^{3+}$, and is an intermediate in the formation of ferryl MP8. The analogous oxidation reaction was also investigated in manganese substituted MP8, and high-valent manganese-oxo MP8 was detected by nanosecond transient absorption. The single electron transfer oxidation of cytochrome *c* peroxidase (CcP) and thiol bound H93G sperm whale myoglobin were also explored. Reverse proteolysis reactions were used to modify the C-terminus of the heme nonapeptide (MP9). Histidine, methionine, tyrosine and tryptophan amides were readily added by trypsin catalyzed peptide synthesis reactions in aqueous DMF solutions. The intramolecular ligand binding properties of the X23MP10 (X = H, M, Y) series was examined by UV-visible and resonance Raman methods. H23MP10 readily forms a low-spin bis-histidine ligated heme center, Y23MP10 appears to bind phenolate at high pH, and M23MP10 does not appear to bind its methionine thioether. The ferrous carbonmonoxy form of MP8 (Fe(II)-CO MP8) was prepared and its photochemistry was explored by transient absorption and resonance Raman methods. Fe(II)-CO MP8 photolysis reactions were used for comparison with cyt *c* folding reactions initiated by CO photodissociation.

Chapter 1: Heme Peroxidases and Cytochrome P450

Introduction

The heme group is at once perhaps both the most ubiquitous and versatile cofactor found in bioinorganic chemistry. An iron protoporphyrin IX (occasionally with minor peripheral modifications) is found at the heart of proteins that carry out such diverse roles as oxygen binding (myoglobins and hemoglobins), electron transfer (the cytochromes) and complex multi-electron redox chemistry (peroxidases, catalases, cytochrome *c* oxidase, and cytochromes P450). The chemical nature of the heme cofactor common to all of these classes of proteins is dictated by the surrounding protein through axial ligand interactions and residues present in the active site pocket near the heme. It is therefore of interest to examine the relationships between heme protein structure and reactivity in order to identify the specific interactions that are responsible for this remarkably diverse chemistry. This chapter will be devoted to a brief discussion of the properties of highly oxidized heme protein intermediates, as well as recent insights into the chemistry of heme oxidases and their models that are relevant to the experiments in this thesis.

Peroxidases

The peroxidases are enzymes that catalyze the two-electron reduction of hydrogen peroxide to water, with subsequent oxidation of either a redox-active protein, as in cytochrome *c* peroxidase (CcP), or a small molecule substrate, as in horseradish peroxidase (HRP). Study of the relationship between the peroxidase active site structure and reactivity is an active area of research. Both CcP and HRP contain in their active sites a single heme with an axial histidine imidazole ligand hydrogen bonded to a carboxylate side chain. The hydrogen bonding to the axial histidine renders it more electron donating to the heme, and this is thought to facilitate cleavage of bound hydroperoxide species during catalysis by stabilizing highly oxidized iron species that are intermediates in the reactions. A recent X-

ray absorption study of peroxidases and myoglobins showed that the iron-imidazole bond is significantly shorter in wild-type CcP (d_{Fe-N} = ~ 2.1 Å) than in wild-type Mb (d_{Fe-N} = ~ 1.9 Å), reflecting the increased donor strength of the hydrogen-bonded peroxidase imidazole. The same study showed that elimination of the D235-H175 hydrogen bond in CcP by site-directed mutagenesis results in elongation of the imidazole-iron bond distance to ~ 2.1 Å, comparable to wild-type Mb.[1]

The ferric heme in the resting state of HRP has been shown by NMR and resonance Raman spectroscopy to be a five-coordinate center. The five-coordinate heme reacts with added hydrogen peroxide to initially form compound 0 (cmp 0), which is thought to be a ferric hydroperoxide complex. Heterolytic cleavage of bound hydroperoxide results in oxidation of the heme to the compound I (cmp I) level, (two electrons above the ferric state) and the generation of one equivalent of water. Single electron reduction of cmp I yields the red cmp II form of the protein. Reduction of cmp II by substrate returns the peroxidase to its resting ferric state, as illustrated in the catalytic cycle of CcP (Figure 1.1). Although there are no well-defined crystallographically characterized Fe(IV)=O porphyrin species, a Fe(IV)=O porphyrin radical formulation for HRP cmp I and a neutral Fe(IV)=O for HRP cmp II are supported by extensive physical measurements. The optical absorption spectrum of HRP cmp I strongly resembles that of known $^2A_{2u}$ radical porphyrins, leading to the initial suggestion that the second oxidizing equivalent was contained in the porphyrin π system, and not on iron or on a protein amino acid.[2] Mossbauer spectra of both HRP cmp I and II exhibit a similar resonance with a isomer shift of approximately 0.03 mm s^{-1}, indicative of the Fe(IV) oxidation state in both cases.[3,4] Temperature-dependent broadening of the Mossbauer resonance in the cmp I spectrum was attributed to weak coupling to a porphyrin centered radical. The Mossbauer of cmp II does not exhibit this line broadening, as expected for a non-radical Fe(IV)=O heme. The position of HRP

Figure 1.1: The catalytic cycle of CcP. The protein is oxidized by hydrogen peroxide to the compound I state, a ferryl porphyrin with a W191 radical. Reduction by cyt *c* gives compound II, which has been shown to be a ferryl porphyrin in a pH-dependent equilibrium with a ferric porphyrin - W191 radical form. Reduction by a second equivalent of cyt *c* yields the starting ferric peroxidase.

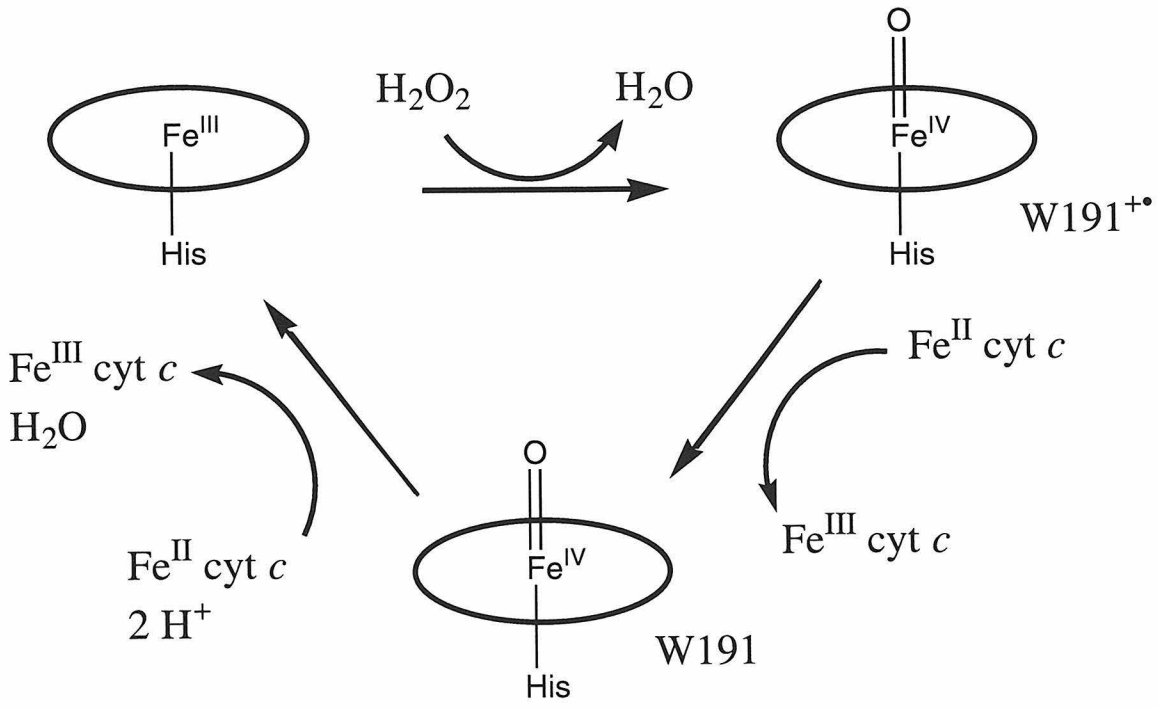
H_2O_2
H_2O
Fe^{III}
His
O
Fe^{IV}
His
$W191^{+\bullet}$
Fe^{II} cyt *c*
Fe^{III} cyt *c*
H_2O
Fe^{II} cyt *c*
$2\ H^+$
O
Fe^{IV}
His
W191
Fe^{III} cyt *c*

Figure 1.2: Top: Crystal structure of cytochrome *c* peroxidase at 1.7 Å resolution. Bottom: Close-up of the CcP active site. Important residues in the distal (R48, H52) and proximal (D235, H175, W191) pockets are highlighted.

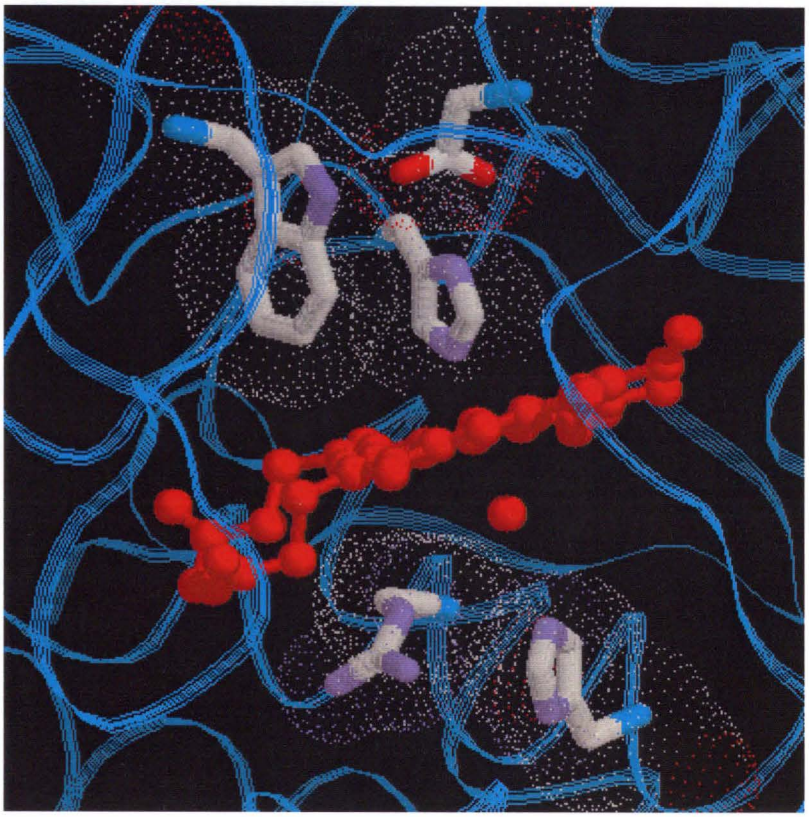

cmp I and II X-ray absorption edges at significantly higher energies than ferric HRP also are consistent with the presence of Fe(IV).[5] Early magnetic susceptibility measurements on HRP cmp I indicated three unpaired electrons per protein, consistent with an Fe(IV) center coupled ferromagnetically to a free radical.[6] ^{17}O ENDOR spectroscopy on HRP cmp I suggests the presence of a single oxygen atom bound to the Fe(IV) center.[7] No strong couplings between protons and iron were found by ENDOR, providing evidence against cmp I containing an Fe(IV)-OH species. The Fe=O stretching frequency of HRP cmp II appears in resonance Raman spectra as an oxygen isotope sensitive band at 779 cm^{-1}.[8] An iron-oxygen distance of approximately 1.6 Å determined by EXAFS measurements on HRP cmp I and small molecule analogs is also consistent with an iron-oxygen double bond. The high-field ^{1}H NMR spectrum of HRP cmp I shows several heme substituent resonances shifted far out of the diamagnetic envelope, but few non-heme signals are affected by cmp I paramagnetism, consistent with spin density localized in the heme π system, as expected for a porphyrin radical.[9]

CcP cmp I (also known as compound ES), like HRP cmp I, also contains an Fe(IV)=O center; however, the second oxidation equivalent has been shown conclusively by ENDOR studies on isotopically enriched proteins to be located on a tryptophan indole side chain that resides in the proximal pocket (W191).[10] Further ENDOR studies have determined that in CcP cmp I, the W191 radical indole ring exists as a protonated cation radical.[11] Studies on the W191G mutant of CcP suggest that the indole ring of W191 occupies a region of the protein that is unusually rich in negative charge, stabilizing monovalent cations that occupy the site, accounting in part for the remarkable stability of this organic radical.[12] The anomalous EPR properties of the W191 radical have been rationalized by a bimodal distribution of couplings with the nearby paramagnetic ferryl ion.[13] The initial product of CcP oxidation by peroxide may be a ferryl porphyrin radical species similar to HRP cmp I, which then reacts to form the relatively stable W191 radical

form of CcP cmp I. Such a radical porphyrin intermediate has not heretofore been detected in the native protein; however, a radical porphyrin intermediate has been observed by rapid-scanning stopped-flow absorption spectroscopy when the W191F mutant is allowed to react with hydrogen peroxide.[14] Oxidation of CcP by hydrogen peroxide and subsequent intraprotein electron transfer result in little structural rearrangement of the protein, as shown by a Laue X-ray structure. No changes in structure were observed at the W191 site; however, the Laue structure does show a small change in the iron atom position and the presence of electron density consistent with the presence of an oxo ligand.[15]

The reduction of hydrogen peroxide by CcP to give CcP cmp I is orders of magnitude faster than the analogous reaction in Mb; clearly, the nature of the active site pocket surrounding the heme promotes binding and reduction of peroxide by CcP. The effects of the distal histidine (H52) and arginine (R48) on CcP catalysis were investigated by reactivity studies on mutant proteins. The rate of peroxide reduction by H52L CcP is dramatically (ca. 10^5 fold) slower than that of WT CcP.[16] The pH dependence of peroxide reduction kinetics suggests that the distal histidine serves to facilitate peroxide binding to the heme iron by acting as a base.[16] R48 is thought to assist in the cleavage of the O-O bond ("pull"). Indeed, R48K and R48L mutants were found to react with peroxide with rates close to (ca. two fold slower) those observed for the WT enzyme at low peroxide concentrations; however, the rates of O-O bond scission, estimated from peroxide saturation kinetics, were found to be ca. 250 and 1950 s^{-1}, ~ 100-fold slower than WT CcP.[17] R48 is also thought to stabilize oxidized forms of CcP by making a hydrogen bond to the ferryl oxygen.[15]

The nature of the reaction between CcP and its redox partner, cytochrome *c* (y-cyt *c*), is still under discussion. Liu and coworkers reported that photoinduced electron transfer from ruthenium-modified cytochrome *c* bound to CcP reduced the cmp I W191 radical center selectively over the ferryl center, and that CcP cmp II reduction also occurred through reduction of a ferric W191 radical form.[18] The structure of a 1:1 complex between

CcP and y-cyt *c* at high ionic strength has been reported by Pelletier and Kraut, who note that the shortest path between the bound cytochrome and the peroxidase radical center moves up the peptide backbone from A194 to W191.[19] Based on these and additional studies in which the contact region between CcP and cyt *c* is modified by mutagenesis, the authors suggest a single electron transfer pathway from cyt *c* to W191.[18-20] However, it has also been suggested that two different binding modes of the cytochrome may explain the two different sites of reduction. Solution studies on metal-substituted CcP's under low ionic strength conditions have pointed to two distinct binding domains for cyt *c* with different efficiencies for electron transfer.[21,22] A recent study by Miller and coworkers showed that only the high affinity site (as shown in the Pelletier and Kraut structure) is redox active, and that the binding of cytochrome to the second, lower affinity site affects the electron transfer kinetics by facilitating the rate-limiting dissociation of the cyt *c* bound in the high affinity site.[23] The increased electron transfer reactivity of the tryptophan center is not due to favorable thermodynamics - the driving force for reduction of the tryptophan cation radical is comparable to that found for reduction of the ferryl porphyrin. Increased electronic coupling or a reduced reorganization energy associated with electron transfer to the tryptophan could account for the high reactivity of the W191 radical.

Clearly, the reactivity of peroxidase enzymes involves an interplay between different redox-active groups, and the paradigm that metal-based chemistry dominates the reactivity of metalloenzymes is clearly no longer valid. The relationships between the metal center, the porphyrin, and oxidizable cofactors are currently under investigation.

Cytochrome P450

Cytochrome P450 enzymes are capable of catalyzing hydroxylation and epoxidation reactions of hydrocarbon substrates using dioxygen as an oxidant under very mild conditions.[24] In addition, P450 enzymes have distinctive spectroscopic characteristics (the

ferrous carbonmonoxy form of the protein has a split Soret band, with one component appearing at 450 nm) that lead to the prediction of axial ligation by a cysteine thiolate group. This combination of unusual reactivity and unique spectroscopic properties has made cytochrome P450 one of the most widely studied heme enzymes. Several P450 isozymes have been crystallographically characterized, and each has heme axial ligation provided by a conserved proximal cysteine residue (Figure 1.3). The structural aspects of bacterial and microsomal P450's have been recently compared and the members of the P450 family are postulated to possess similar general folds in spite of low sequence homology.[25] The distal pockets of P450 enzymes differ from peroxidase enzymes in that they are largely hydrophobic; most of distal residues are aromatic, although some polar residues are present, and these are postulated to serve as general bases for the deprotonation of bound hydroperoxide during catalysis. Hydroxylation reactions catalyzed by P450 require protons that ultimately are derived from water. Several possibilities exist for solvent channels from the exterior of the protein to the active site, and it is reasonable that adventitious water in the active site pocket acts as a proton donor. In particular, D251 and T252 are thought to participate in delivery of protons to the active site.[26] Indeed, hydroxylation of camphor is greatly slowed and an unusual spectral intermediate is observed during catalysis by the D251E $P450_{CAM}$ mutant, possibly the ferric peroxide species resulting from reduction of the ferrous dioxygen form.[27]

Figure 1.3: Top: Crystal structure of reduced $P450_{CAM}$ at 2.2 Å resolution with a product hydroxycamphor bound. Bottom: Close-up of the $P450_{CAM}$ active site. The axial C357 ligand and the bound product, 5-exo-hydroxycamphor, are highlighted.

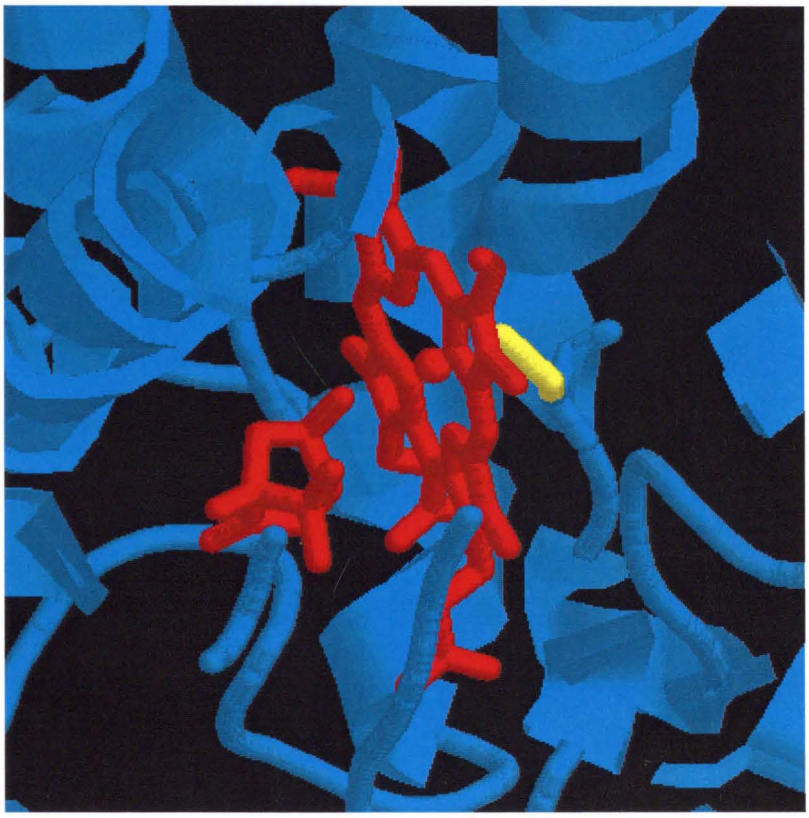

High-valent metal-oxo species analogous to peroxidase compounds I and II may be the active species in P450 catalyzed hydroxylation reactions; however, these intermediates have not been observed due to the nature of P450's catalytic cycle (Figure 1.4). In the reaction cycle of $P450_{CAM}$, a soluble P450 that has been extensively characterized by spectroscopic and crystallographic methods, the resting ferric protein has a six-coordinate, low-spin iron center, with an axially bound water molecule. Binding of camphor to the protein results in extrusion of coordinated water, resulting in a high-spin ferric center. Electron transfer then occurs from P450's redox partner, putiradoxin, resulting in a ferrous center that binds dioxygen. This form of $P450_{CAM}$, analogous to the oxy form of Mb, is the final observed intermediate in the reaction cycle of wild type protein. In the rate-determining step of the cycle, a second electron is transferred to the oxy-heme, resulting in rapid turnover of the bound camphor substrate into oxidized product and regeneration of the resting state of the protein.

Groves and coworkers have proposed an "oxygen-rebound" mechanism in which a high-valent iron-oxo species similar to peroxidase cmp I abstracts a hydrogen atom from the hydrocarbon substrate, resulting in a metal-hydroxyl and an organic radical. These radicals then collapse ("rebound") to yield the hydroxylated product and the reduced metal center (Figure 1.4). This mechanistic proposal has been probed by the use of radical clock substrates that undergo rearrangement in their cation or neutral radical forms. Such radical clock studies are consistent with the generation of a substrate radical during catalysis. Estimated rates for the rebound step, measured with the ultrafast radical substrate clock 2-t-butoxy-3-phenylcyclopropylmethane, are exceedingly high, suggesting that radical recombination occurs on approximately the same timescale as a single molecular vibration. Other proposals for P450 reactivity implicate ferric peroxide species as the active hydroxylating agent; however, the Groves mechanism is preferred by most investigators.

Figure 1.4: Top: The reaction cycle for generation of highly oxidized species and hydroxylation of substrate in cytochrome $P450_{CAM}$. Bottom: The oxygen rebound mechanism for the reaction of the postulated iron-oxo intermediate in P450 catalysis.

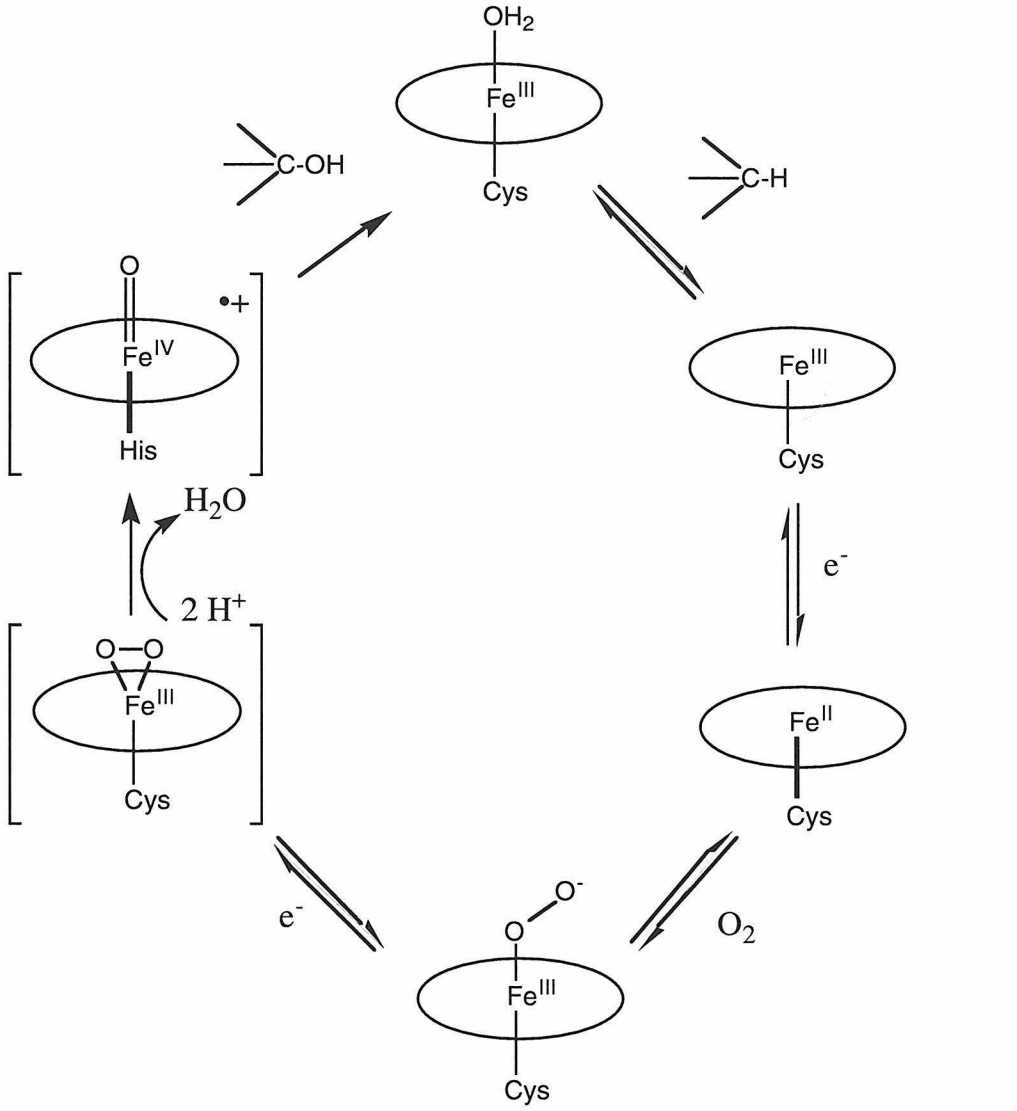
OH2
Fe III
Cys
C-OH
C-H
O
•+
Fe IV
His
Fe III
Cys
H2O
2 H+
e-
O—O
Fe III
Cys
Fe II
Cys
e-
O2
O-
O
Fe III
Cys

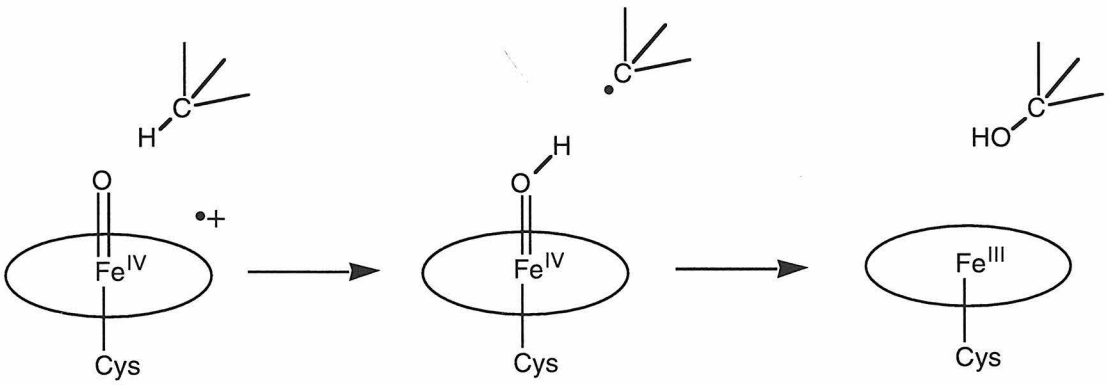
H
C
O
•+
Fe IV
Cys
C
H
O
Fe IV
Cys
HO
C
Fe III
Cys

Models of the P450 active site (both protein-based and synthetic) have succeeded in reproducing the spectroscopic features of the ferric state of the protein. The ferric thiolate-bound forms of H93G and the H93C mutant of SW Mb both have optical spectra that strongly resemble the high-spin form of ferric P450. However, the distinctive spectroscopy of the reduced form of P450 has not been duplicated in any model system. Reduction of the proteins under carbon monoxide atmosphere results in a species with a Soret absorption at approximately 420 nm, possibly due to dissociation of the thiolate ligand and coordination of the distal histidine. There are also presently very few well-characterized models for the putative oxidized forms of P450, namely the thiolate-coordinated ferryl or ferric peroxide complexes.

Research Overview

Many of the experiments reported in this thesis were done with the goal of developing a useful model peroxidase system, and the reactivity of this system was investigated in an attempt to elucidate the oxidation-reduction chemistry of heme proteins. The structures of microperoxidase-8 (MP8) and other heme peptides were studied by NMR, optical, and resonance Raman spectroscopic methods. The relative reactivities towards oxidation of porphyrins and their chelated metal ions were probed by nanosecond flash-photolysis. Studies of the heme peptide MP8 demonstrated that the porphyrin ring is in general more reactive than the ferric center with outer-sphere oxidants. Reaction products with an oxidized metal center appear to be derived exclusively from porphyrin radical intermediates. The single electron oxidation of ferric MP8 to ferric radical and ferryl states is formally the reverse reaction performed by peroxidase cmp II when oxidizing substrates. It is reasonable, therefore, to believe that reduction of peroxidase cmp II may proceed through a porphyrin radical intermediate. It is known that small molecule substrates of peroxidases are oxidized at the heme edge, consistent with involvement of a

porphyrin-centered oxidizing equivalent. Initial studies on MP8 were subsequently extended to intact heme proteins, including HRP and CcP. High-valent metal-oxo and porphyrin-radical species were observed in both cases. Thiolate-bound forms of axial-ligand mutants of myoglobin were also investigated, in hopes of generating highly oxidized thiolate bound heme analogs of the P450 reactive intermediate; unfortunately, no such product was observed.

References and Notes

(1) Sinclair, R.; Hallam, S.; Chen, M.; Chance, B.; Powers, L. *Biochemistry* **1996**, *35*, 15120-15128.

(2) Dolphin, D.; Forman, A.; Borg, D. C.; Fajer, J.; Felton, R. H. *Proc. Natl. Acad. Sci. U. S. A.* **1971**, *68*, 614-618.

(3) Maeda, Y.; Morita, Y. *Biochem. Biophys. Res. Comn.* **1967**, *29*, 680-685.

(4) Moss, T. H.; Ehrenberg, A.; Bearden, A. J. *Biochemistry* **1969**, *8*, 4159-4162.

(5) Penner-Hahn, J. E.; McMurry, T. J.; Renner, M.; Latos-Grazynsky, L.; Eble, K. S.; Davis, I. M.; Balch, A. L.; Groves, J. T.; Dawson, J. H.; Hodgson, K. O. *J. Biol. Chem.* **1983**, *258*, 12761-12764.

(6) Theorell, H.; Ehrenberg, A. *Arch. Biochem. Biophys.* **1952**, *41*, 442-461.

(7) Roberts, J. E.; Hoffman, B. M.; Rutter, R.; Hager, L. P. *J. Am. Chem. Soc.* **1981**, *103*, 7654-7656.

(8) Terner, J.; Sitter, A. J.; Reczek, C. M. *Biochim. Biophys. Acta* **1985**, *828*, 73-80.

(9) LaMar, G. N.; deRopp, J. S.; Smith, K. M.; Langry, K. C. *J. Biol. Chem.* **1981**, *256*, 237-243.

(10) Sivaraja, M.; Goodin, D. B.; Smith, M.; Hoffman, B. M. *Science* **1989**, *245*, 738-740.

(11) Huyett, J. E.; Doan, P. E.; Gurbiel, R.; Houseman, A. L. P.; Sivaraja, M.; Goodin, D. B.; Hoffman, B. M. *J. Am. Chem. Soc.* **1995**, *117*, 9033-9041.

(12) Miller, M. A.; Han, G. W.; Kraut, J. *Proc. Natl. Acad. Sci. USA* **1994**, *91*, 11118-11122.

(13) Houseman, A. L. P.; Doan, P. E.; Goodin, D. B.; Hoffman, B. M. *Biochemistry* **1993**, *32*, 4430-4443.

(14) Erman, J. E.; Vitello, L. B.; Mauro, J. M.; Kraut, J. *Biochemistry* **1989**, *28*, 7992-7995.

(15) Fulop, V.; Phizackerly, R. P.; Soltis, S. M.; Clifton, I. J.; Wakatsuki, S.; Erman, J.; Hajdu, J.; Edwards, S. L. *Structure* **1994**, *2*, 201-208.

(16) Erman, J. E.; Vitello, L. B.; Miller, M. A.; Shaw, A.; Brown, K. A.; Kraut, J. *Biochemistry* **1993**, *32*, 9798-9806.

(17) Vitello, L. B.; Erman, J. E.; Miller, M. A.; Wang, J.; Kraut, J. *Biochemistry* **1993**, *32*, 9807-9818.

(18) Liu, R.-Q.; Miller, M. A.; Han, G. W.; Hahm, S.; Geren, l.; Hibdon, S.; Kraut, J.; Durham, B.; Millett, F. *Biochemistry* **1994**, *33*, 8678-8685.

(19) Pelletier, H.; Kraut, J. *Science* **1992**, *258*, 1748-1755.

(20) Miller, M. A.; Liu, R.-Q.; Geren, S. H. L.; Hibdon, S.; Kraut, J.; Durham, B.; Millet, F. *Biochemistry* **1994**, *33*, 8686-8693.

(21) Zhou, J. S.; Hoffman, B. M. *Biochemistry* **1994**, *265*, 1693-1696.

(22) Stemp, E. D. A. *Biochemistry* **1993**, *32*, 10848-10865.

(23) Miller, M. A. *Biochemistry* **1996**, *35*, 15791-15799.

(24) Sono, M.; Roach, M. P.; Coulter, E. D.; Dawson, J. H. *Chem. Rev.* **1996**, *96*, 2841-2887.

(25) Hasemann, C. A.; Kurumbail, R. G.; Boddupali, S. S.; Peterson, J. A.; Deisenhofer, J. *Structure* **1995**, *2*, 41-62.

(26) Poulos, T. L.; Raag, R. *FASEB J.* **1992**, *6*, 674-679.

(27) Gerber, N. C.; Sligar, S. G. *J. Biol. Chem.* **1994**, *269*, 4260-4266.

Chapter 2: Preparation, Purification and Characterization of Microperoxidases

Introduction

Small molecule models of heme proteins have been invaluable to investigations of the chemistry of heme proteins. Since the preparation and oxygen-binding properties of the "picket fence" porphyrins (the first successful truly functional synthetic heme protein models) were reported by Collman and coworkers,[1] the field of small molecule modeling of heme proteins has evolved to incorporate ever more complex substitution of the porphyrin in order to more closely mimic the intricate chemistry of heme proteins themselves.[2-4] More sophisticated models feature coordinating groups such as imidazole covalently attached to the porphyrin to mimic protein-derived axial ligands[5] ("tailed" porphyrins), and/or steric hindrance over the distal face of the porphyrin to simulate the crowded environment of a heme protein's active site pocket ("capped" and "strapped" porphyrins). Synthetic routes to these molecules, however, are often long and sometimes tedious. In addition, many of these synthetic models are not soluble in water, a desirable property for studies relevant to biological systems.

An attractive small molecule model system related to synthetic tailed porphyrins that is readily prepared and highly water soluble are the fragments of cyt *c* commonly referred to as microperoxidases (MP's).[6] Heme-containing hydrolytic fragments of cyt *c* were among the first well-characterized products of the enzymatic cleavage of proteins: MP11 was first characterized by Tuppy and Paleus in 1955[7] who quickly recognized its peroxidase activity.[8] Reports of the preparation of the smaller common MP fragments, MP8[9] and MP9,[10] soon followed. We have prepared and made extensive use of MP fragments in the studies reported in this thesis. These molecules consist of the active site heme of cyt *c* covalently attached to a short peptide segment that includes the axial H18 residue.[6,8,11-15] The use of selective proteases to effect the hydrolysis of the protein ensures controlled proteolysis. The length of the attached peptide can be controlled by

variation of the hydrolytic conditions: treatment of cyt *c* with trypsin yields MP9 as the predominant heme-containing product (amino acids 14-22 of h-cyt *c*), while treatment with pepsin gives MP11 (11-21). Sequential treatment with both pepsin and trypsin gives the widely used MP8 fragment (14-21). Acetylation of the amino terminus of MP8 inhibits the formation of peptide aggregates.[13,16] Purification by FPLC is simple and efficient, leading to pure material as gauged by mass spectrometry and NMR spectroscopy.

The spectroscopic and magnetic properties of ferric MP8 have been investigated by several independent groups. Kassner and coworkers used Evans method solution magnetic susceptibility measurements to determine the magnetic moment of MP8 in mixed aqueous-organic solvents and assigned the spin state to be a thermal equilibrium between high (S = 5/2) and low (S = 1/2) spin states.[17] Van Wart and coworkers employed resonance Raman spectroscopy in conjunction with magnetic circular dichroism (MCD) and electron paramagnetic resonance (EPR) spectroscopies, and concluded that the high spin state is in equilibrium with an intermediate spin form (S = 3/2).[12,16] Munro and Maruqes conclude from optical spectroscopy that acetyl MP8 exists as an equilibrium between an admixed S = 5/2 <-> 3/2 and a pure S = 1/2 state.[13] In order to further investigate the electronic structure of the MP8 iron center, we have investigated the nature of the iron spin state by directly measuring the low-temperature absorption spectrum (at 77 K) and magnetic susceptibility (1.8 K) in alcoholic solvents. Alcoholic solvents were selected because they are known to inhibit aggregation of MP's (aggregation of acetyl MP8 has been shown to be predominantly a π–π stacking phenomenon,[18] and the more hydrophobic environment provided by alcoholic solvents aids in their dispersion) and have favorable properties for low-temperature optical studies (methanol-ethanol mixtures are commonly used low-temperature glassing solvents).

Experimental Section

Materials: All reagents were used as received and were of the highest available quality. h-cyt *c*, trypsin and pepsin were obtained from Sigma. The trypsin used was treated with TPCK or DPCC to inhibit any chymotrypsin present in the preparation. Deionized water was further purified by a Barnstead Nano-Pure system and filtered through a 2 μM membrane before use in FPLC purifications. Acetonitrile (Omni-Solve grade) and trifluoroacetic acid used in FPLC purification were obtained from VWR. Acetic anhydride was obtained from Aldrich. Potassium phosphate buffers were typically 0.1 M ionic strength, and their pH was checked with a Beckman pHI-32 pH meter standardized against pH 4 and 7 buffer solutions (VWR).

Methods:

Procedures for the preparation and isolation of MP fragments have been reported previously by others.[7,9-11,16,19] These procedures with some modifications have been used here. All Amicon ultrafiltrations were done with a YM1 membrane in a stirred cell under 40 psi argon. A standard protocol was used for preparative FPLC purification of most MP fragments. Buffer A was 0.1% TFA in water, and buffer B was 60% acetonitrile 40% water with 0.1% added TFA. The solution containing the crude MP fragment was applied to a Pharmacia PepRPC 16/10 column, and very hydrophilic contaminants were removed by washing for 10 minutes with 20% B. A flow rate of 5 mL/minute was used for most runs. After 10 minutes at 20% B, a gradient to 60% B was initiated (25 min), during which the heme-containing MP fragment was observed to elute from the column and was collected. For multiple runs, a loop program was used, where the column was cleaned by washing with 10 minutes of 100% B and re-equilibrated with 20% B for 10 minutes before the standard program was run again. Matrix-assisted laser desorption (MALDI) mass spectra were collected by Dr. Gary Hathaway on a PerSeptives Biosystems ELITE

mass spectrometer in the Beckman Institute Peptide and Protein Analytical Laboratory. Routine optical spectra were collected with a Hewlett-Packard 8452A diode array spectrophotometer. Solution concentrations of MP fragments were determined spectrophotometrically using $\varepsilon = 1.57\ mM^{-1}\ cm^{-1}$ at 396 for MP8 in neutral solution,[11] and $\varepsilon = 1.59\ mM^{-1}\ cm^{-1}$ at 396 nm for MP9 in neutral solution.[20] Peptides were typically stored in the refrigerator as lyophilized solids.

MP9: 1 g of h-cyt *c* was dissolved in 200 mL water. The pH was adjusted to 8 with concentrated ammonium hydroxide. 50 mg of DPCC treated trypsin was added in a single portion, and the resulting red solution was allowed to stand overnight. The volume was reduced to approximately half by ultrafiltration. Solid ammonium sulfate was added until the mixture became turbid. Water was added to clarify the solution, which was then placed in a refrigerator (4° C) overnight. The precipitate was collected by centrifugation (5 k RPM, 20 min), and dissolved in 0.1% aqueous TFA solution. Excess ammonium sulfate was removed and the MP9 solution was concentrated by ultrafiltration. The concentrated crude MP9 was purified by 3 runs of the standard FPLC protocol. MP9 typically elutes from the column at approximately 45% B (Figure 2.1). The optical absorption spectrum of a dilute solution of MP9 in pH 7 buffer is typical of high spin ferric porphyrins, with a Soret at 396 nm (Figure 2.2). A molecular mass of 1635 (1506 + 128, the mass of MP8 plus the additional K residue) is expected and a value of 1634.0 was found from MALDI mass spectra (Figure 2.3).

MP8: 200 mg of h-cyt *c* was dissolved in water. The pH was adjusted to 2 using 1 M hydrochloric acid. The color of the solution turns from red to brown. 5.5 mg of pepsin dissolved in water was added. The solution was allowed to stand for 1/2 hour before a second 5.5 mg of pepsin was added. The brown solution was allowed to stand overnight. Concentrated ammonium hydroxide was added to the solution to adjust the pH

Figure 2.1: Crude MP9 purified on PepRPC 16/10 column, using water-acetonitrile buffer gradient (0-60%). The MP9 is the large fraction eluting at approximately 45% buffer B indicated by the arrow. Flow rate: 5 mL/min, absorption monitored at 254 nm.

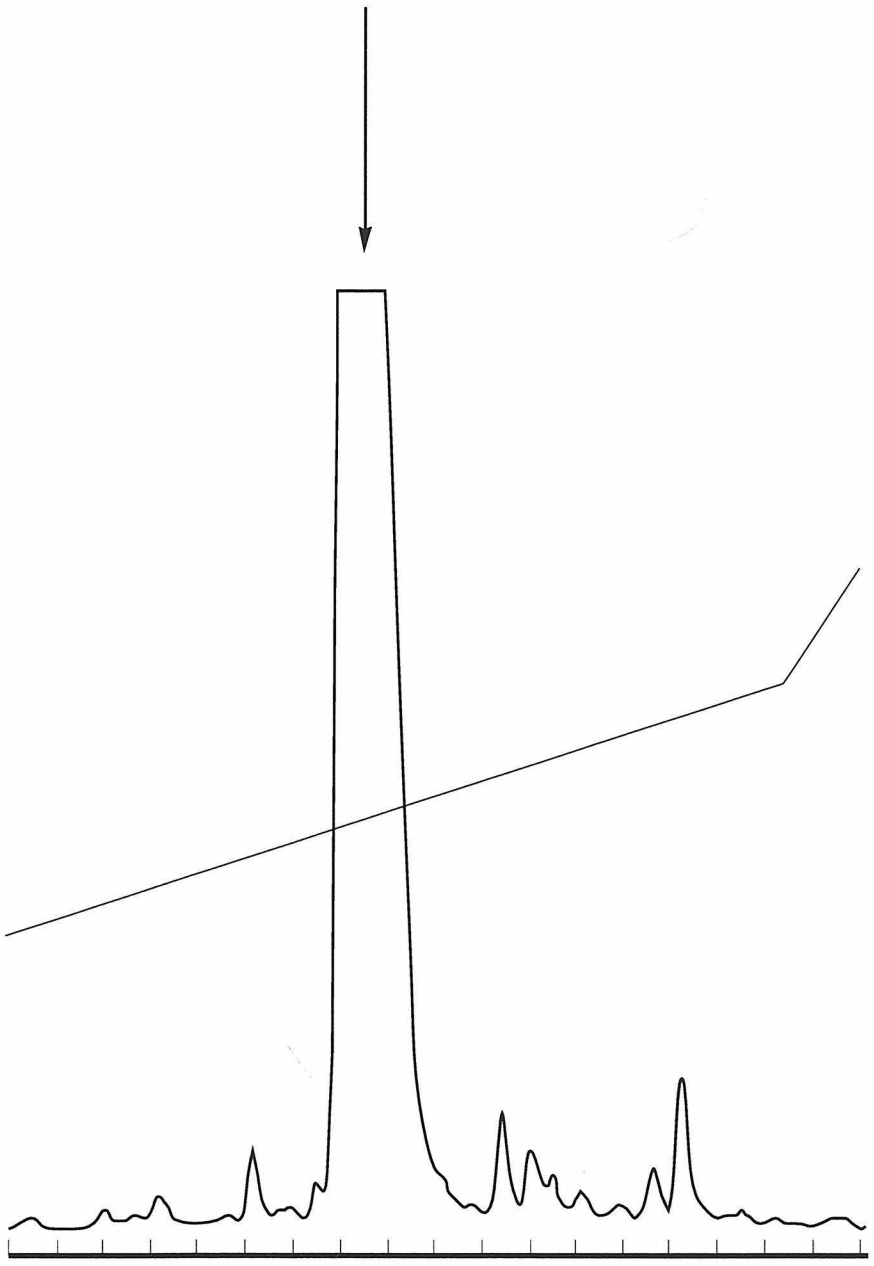

Figure 2.2: Optical spectra of MP9 in pH 6.3 100 mM phosphate buffer (top) and MP8 in pH 7.0 100 mM phosphate (bottom). The Q-band regions are shown magnified by 3 to show detail. ε is given in M^{-1} cm^{-1}.

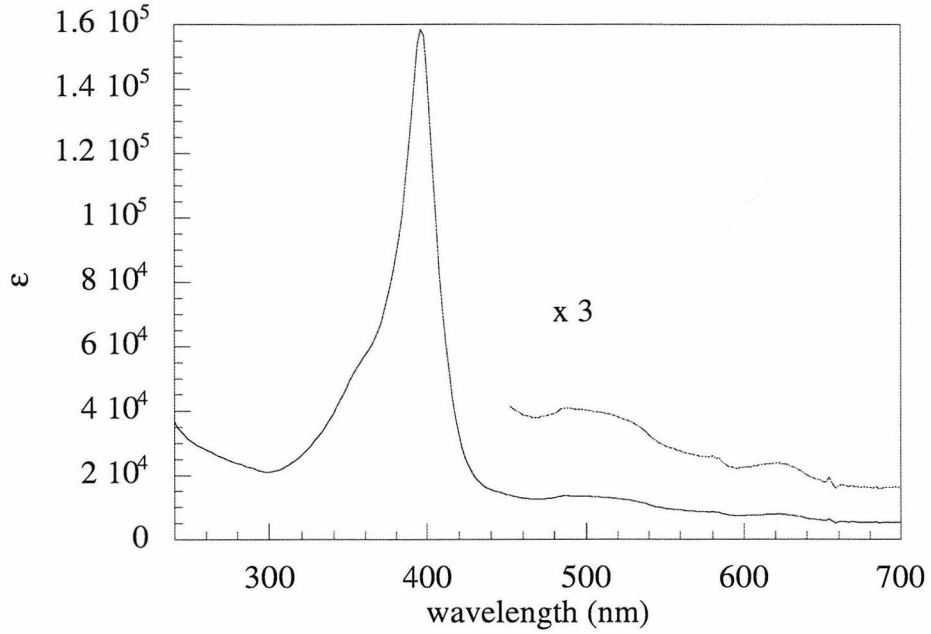
1.6 10^5
1.4 10^5
1.2 10^5
1 10^5
8 10^4
6 10^4
4 10^4
2 10^4
0
ε
x 3
300
400
500
600
700
wavelength (nm)

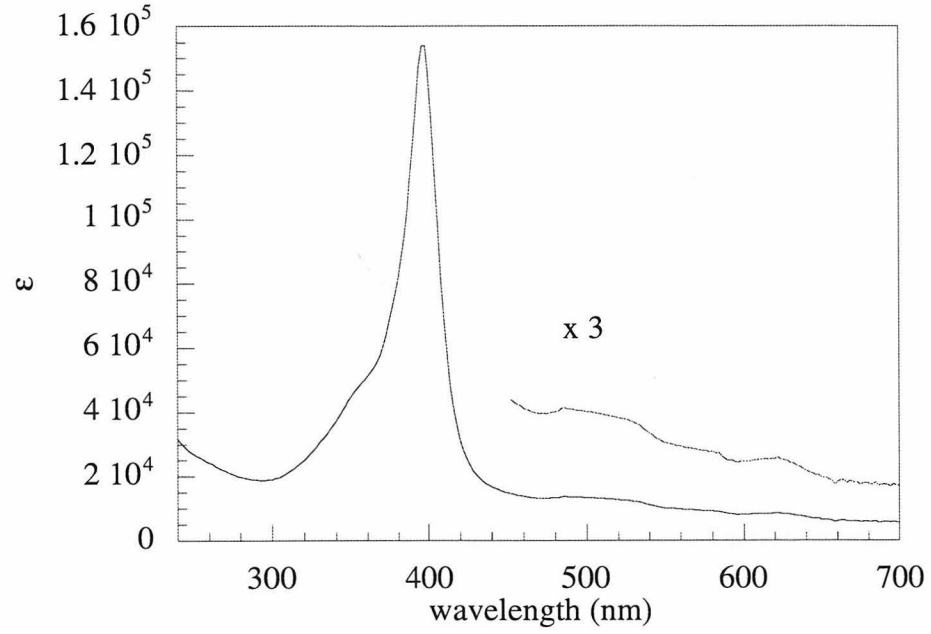
1.6 10^5
1.4 10^5
1.2 10^5
1 10^5
8 10^4
6 10^4
4 10^4
2 10^4
0
ε
x 3
300
400
500
600
700
wavelength (nm)

Figure 2.3: MALDI-TOF mass spectrum of MP9. Sample was approximately 20 μM in peptide, ca. 30% acetonitrile/water 0.1% TFA. Masses were calibrated with acetyl angiotensin and ANF.

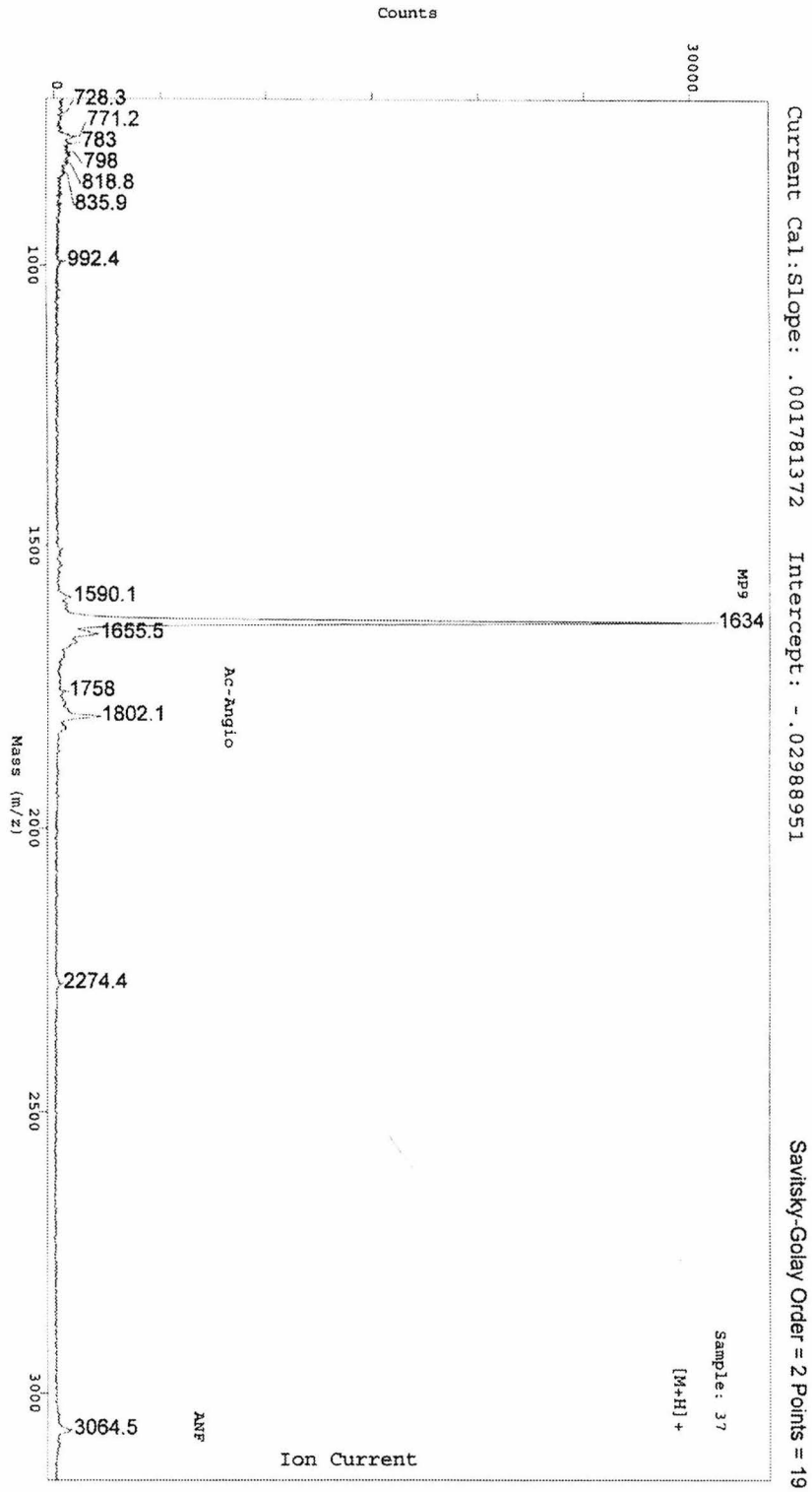
Counts
30000
0
728.3
771.2
783
798
818.8
835.9
992.4
1000
1500
1590.1
1655.5
1758
1802.1
2000
2274.4
2500
3000
3064.5
Mass (m/z)
Ion Current
Ac-Angio
ANF
MP9
1634
Sample: 37
[M+H]+
Current Cal:Slope: .001781372 Intercept: -.02988951
Savitsky-Golay Order = 2 Points = 19

to 8.5, and 11 mg of trypsin dissolved in water was added. The reaction was allowed to proceed overnight. The total volume of the mixture was brought to 20 mL by dilution with water, and 11 g of ammonium sulfate was added to precipitate the crude MP8. The solid was collected by centrifugation (5 k RPM, 20 min), and the supernatant was discarded. The solid material was redissolved in 0.1% aqueous TFA, washed 2x and concentrated in an Amicon stirred cell (50 mL, YM1 membrane). The concentrated crude MP8 solution was purified by the standard FPLC protocol described above. Under the standard FPLC conditions, MP8 elutes at approximately 45% B (Figure 2.4). The major colored fraction was collected, and its purity assayed by mass spectrometry and UV-visible spectroscopy. The optical spectrum of MP8 in neutral solution is very similar to that of MP9 with a Soret band at 396 nm and two relatively weak transitions in the visible region (Figure 2.2). A mass of 1506 was expected for the aquo form of MP8 (Fe C_{34} H_{32} N_4 O_4 was used for an iron protoporphyrin IX, giving a mass of 616, and four protons are added as a result of the thioether condensation for a total of 620 for the heme *c*, a mass of 870 was calculated for the neutral peptide; however , the mass of two protons are subtracted since the cysteines bind the heme as thioethers, giving a value of 868, 868 + 620 + 18 = 1506 amu expected, and a value of 1506.3 was obtained from MALDI mass spectra (Figure 2.5). Very little fragmentation is observed in the MALDI mass spectra taken in the linear mode. Occasionally a small amount of a fragment with mass 617.2 was observed, and this was attributed to cleavage of the thioether bonds and the rearranged protonated heme fragment is detected. A similar fragmentation pattern was also observed in the fast-atom bombardment mass spectra of heme peptides;[21] however, the extent of the fragmentation is much smaller for the MALDI ionization method employed here. Peaks corresponding to the mass of the MP with an associated sodium are often observed, as apparently, a small amount of adventitious sodium is present even in FPLC purified samples.

Figure 2.4: Crude MP8 purified on PepRPC 16/10 column, using water-acetonitrile buffer gradient (0-60%). The MP8 product is the large fraction eluting at approximately 45% buffer B indicated by the arrow. Flow rate: 5 mL/min, absorption monitored at 254 nm.

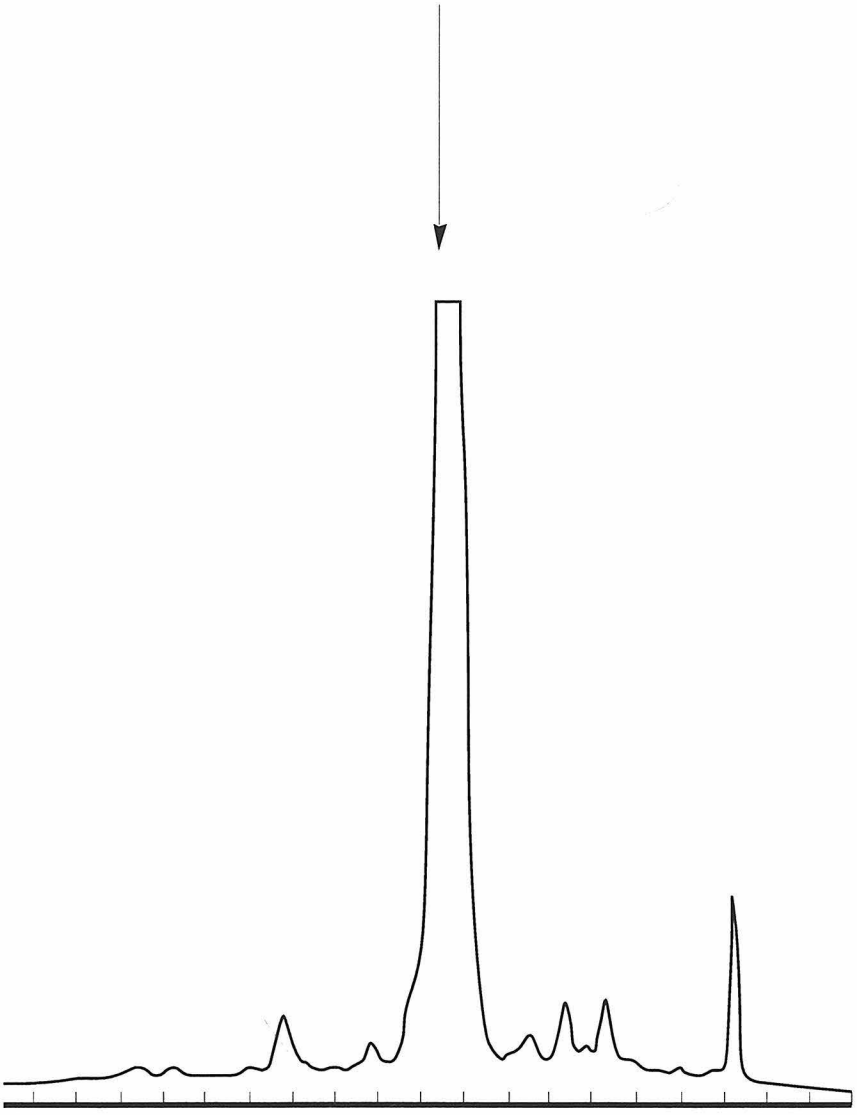

Figure 2.5: MALDI-TOF mass spectrum of MP8. Sample was approximately 20 μM in peptide, ca. 30% acetonitrile/water 0.1% TFA. Masses calibrated against acetyl angiotensin.

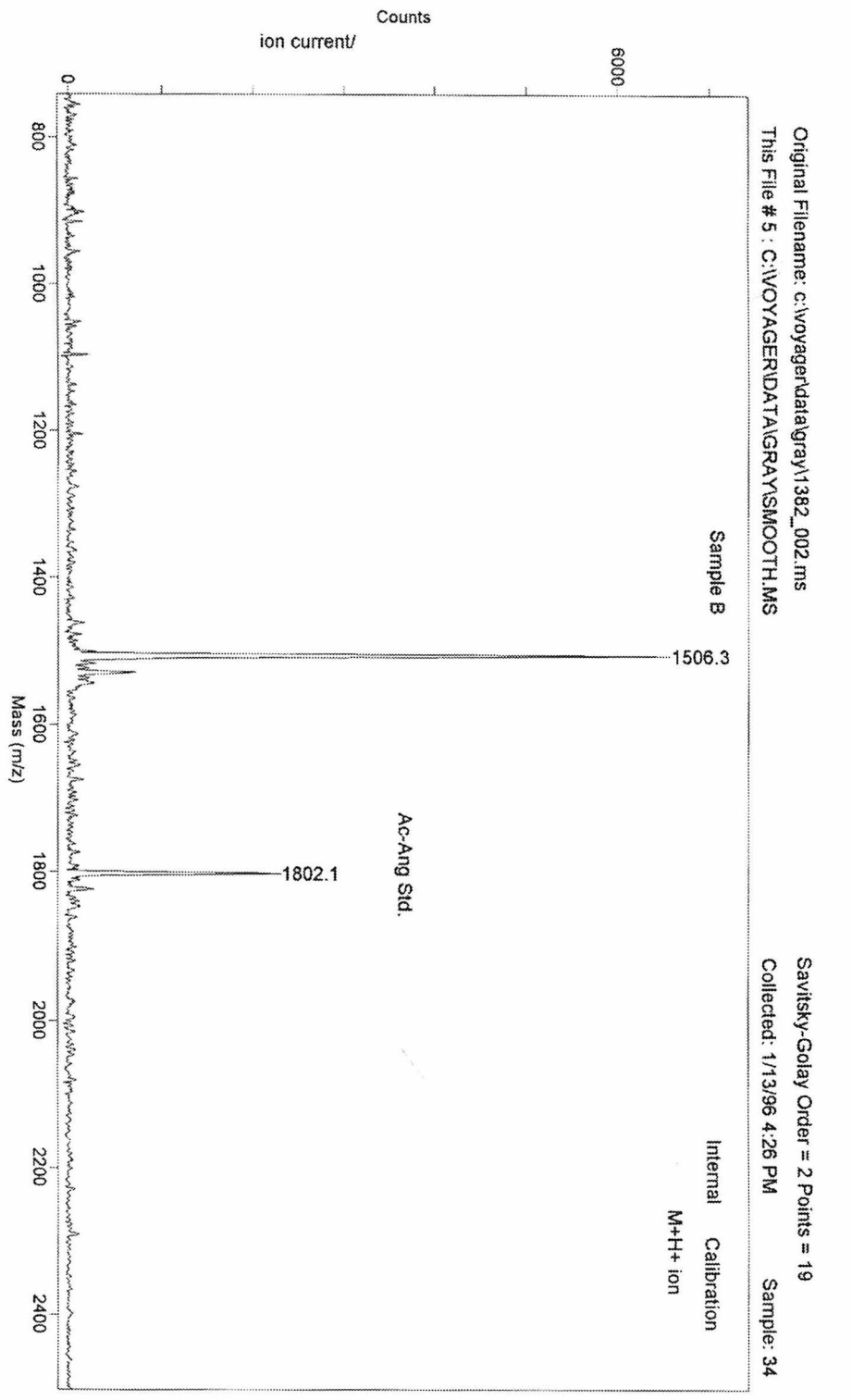
Original Filename: c:\voyager\data\gray\1382_002.ms
This File # 5 : C:\VOYAGER\DATA\GRAY\SMOOTH.MS
Savitsky-Golay Order = 2 Points = 19
Collected: 1/13/96 4:26 PM
Sample: 34
Counts
ion current/
6000
0
800
1000
1200
1400
1600
1800
2000
2200
2400
Mass (m/z)
Sample B
1506.3
Ac-Ang Std.
1802.1
Internal Calibration
M+H+ ion

N-acetyl MP8: Purified MP8 was dissolved in 0.1 M potassium bicarbonate buffer, pH 9. A 500-fold excess of acetic anhydride was added in 10 portions over the course of an hour, with continuous stirring. Gas evolution was observed, and the pH was maintained at 9 by addition of small amounts of sodium hydroxide solution if needed. Bicarbonate salts were removed from the sample by either gel filtration (Sephadex G-25) or ultrafiltration. The acetylated material was purified from any remaining starting material by the standard FPLC protocol. As expected, the acetylated material is more hydrophobic and elutes later than the starting material, eluting at approximately 56% B (Figure 2.6). The identity and purity of the material was verified by MALDI mass spectrometry, which showed a dominant peak at 1550 amu (1549 calculated) and no evidence of starting material or side products (Figure 2.7). The yields of acetylated MP8, therefore, are essentially quantitative.

77 K absorption measurements: Low-temperature absorption measurements were made with a Cary-14 spectrophotometer with an OLIS computer control retrofit. Low temperatures were achieved by placing the sample cuvette in a specially designed dewar with a copper block cooled by a liquid nitrogen bath. The formation of condensation on the windows of the dewar was suppressed by directing a stream of compressed air at the window surface.

Low-temperature magnetic susceptibility: Low-temperature magnetic susceptibility measurements were done by Jeff Clites using the Superconducting Quantum Interference Device (SQUID) in the Beckman Institute. Samples (60 μL, 200 μM in acetyl MP8, or 500 μM in acetyl MP8 with excess cyanide) were placed in house-made Teflon sample containers for measurement. Measurements were made at 1.8 K by sweeping the applied magnetic field and observing the induced sample magnetization.

Figure 2.6: FPLC purification of acetyl MP8. The large peak is the Ac-MP8 product.

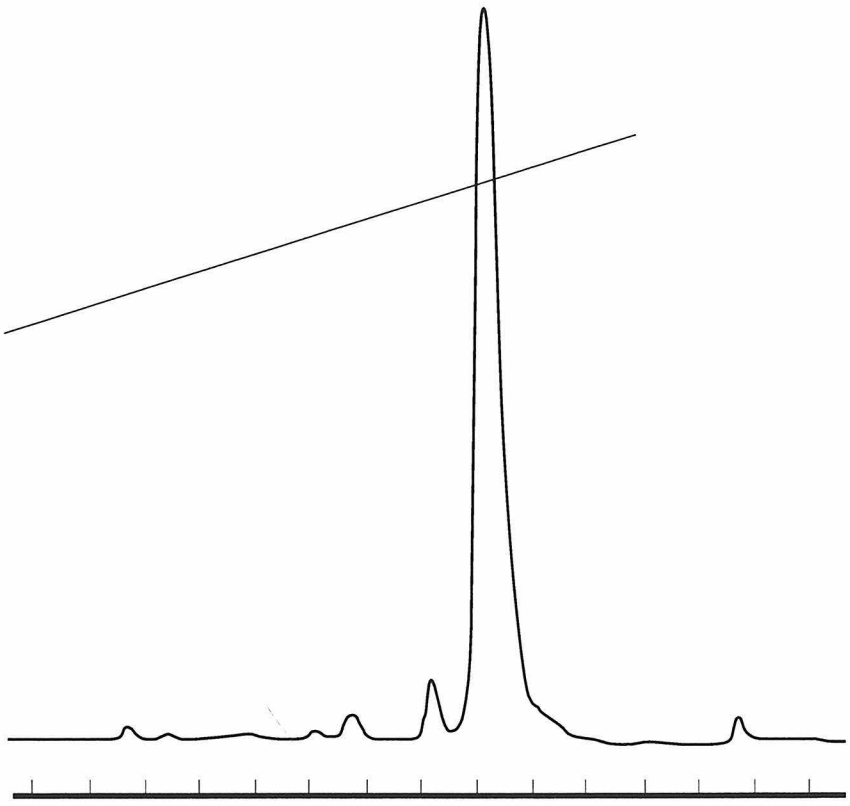

Figure 2.7: MALDI-TOF mass spectrum of acetyl MP8. Sample was approximately 20 μM in peptide in water 0.1% TFA. Masses standardized using bradykinin.

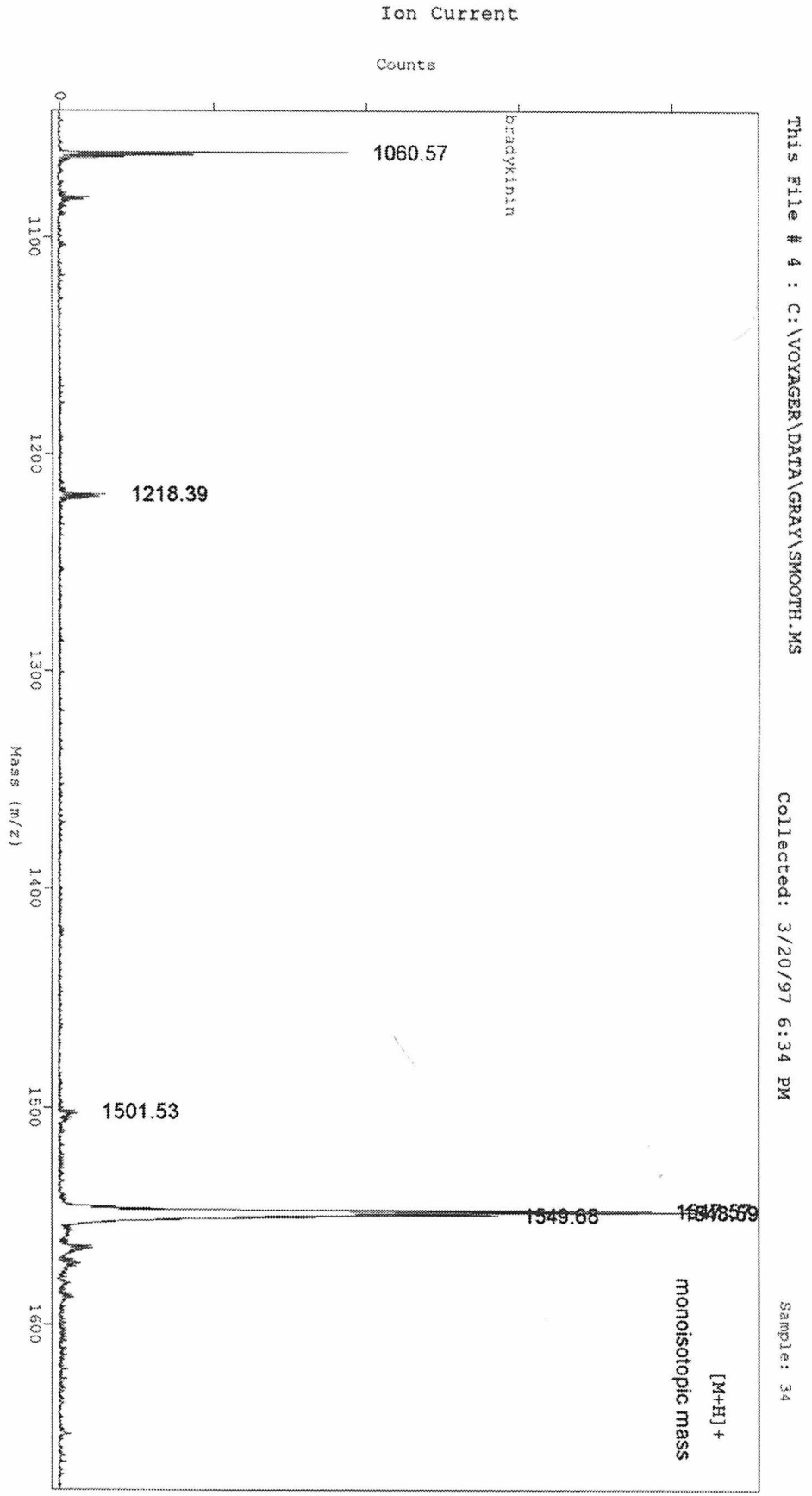
Ion Current
Counts
0
bradykinin
1060.57
1218.39
1501.53
1549.68
1648.59
1100
1200
1300
1400
1500
1600
Mass (m/z)
This File # 4 : C:\VOYAGER\DATA\GRAY\SMOOTH.MS
Collected: 3/20/97 6:34 PM
Sample: 34
[M+H]+
monoisotopic mass

Results and Discussion

The optical spectrum of resting MP8 prepared as above in neutral phosphate buffer is entirely consistent with reported spectra.[11,12,15] This spectrum is typical of a high-spin ferric center, and there is no evidence in the room temperature optical spectrum of the presence of a second spin state (Figure 2.2). Cooling an alcoholic solution of MP8 to 77 K in a liquid nitrogen bath, however, results in a distinct color change from brownish-green to a deep forest green. The low temperature optical spectrum reveals that in addition to significant band sharpening and an increase in intensity due to the temperature change, the Soret band is shifted strongly to the red from 397 nm at room temperature to 404 nm at 77 K. Additionally, two broad Q-bands appear at 554 and 524 nm (Figure 2.8). These features are qualitatively similar to those of a low spin ferric porphyrin, such as the ferric-cyano form of MP8, which also has a red-shifted Soret band (410 nm) and a broad Q band at 538 nm.[22]

The magnetic susceptibility of MP8 at extremely low temperatures was measured using a SQUID magnetometer. A sample of acetyl MP8 with no added exogenous ligands was run, and the results were compared with those from a sample of acetyl MP8 with an excess of cyanide ligand present, to ensure the presence of a low-spin chromophore. Both samples show a saturating magnetization characteristic of a paramagnetic material. The curvature of the magnetization was fit to a Brillouin function using a Kaleidagraph macro. The fits were corrected for the diamagnetic contributions from the solvent. The data from both samples were most consistent with the presence of a low-spin iron center, with 0.59 ± 0.04 spins on average found for the met-cyano MP8 compared to 0.64 ± 0.04 spins for the acetyl MP8 (Figure 2.9). While the slightly higher value found for the acetyl MP8 may indicate the presence of a small amount of intermediate

Figure 2.8: Room temperature and 77 K absorption spectra of acetyl MP8 in methanol/ethanol solution (glass). Broken line: room temperature solution spectrum. Solid line: 77 K glass.

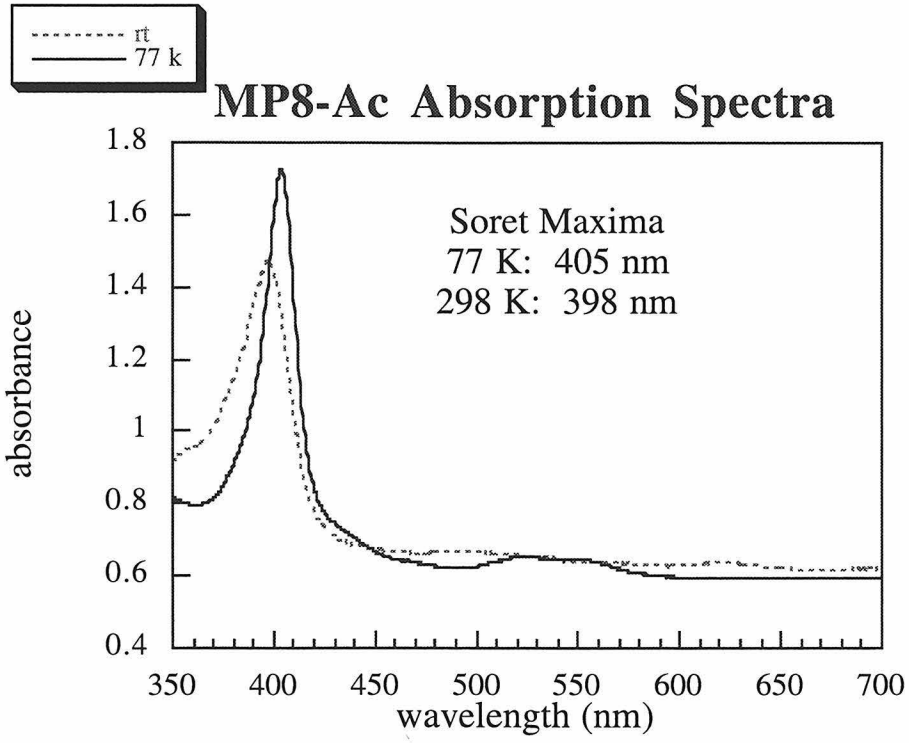
rt
77 k
MP8-Ac Absorption Spectra
Soret Maxima
77 K: 405 nm
298 K: 398 nm
absorbance
1.8
1.6
1.4
1.2
1
0.8
0.6
0.4
350
400
450
500
550
600
650
700
wavelength (nm)

Figure 2.9: Magnetization saturation curves obtained from SQUID measurements. Top: 200 μM acetyl MP8 in methanol, 1.8 K. Bottom: 500 μM acetyl MP8 in methanol with excess cyanide added. The curve through the data points is a least-squares fit to the Brillouin function. The value for m1 is the number of unpaired spins per molecule based on the fit.

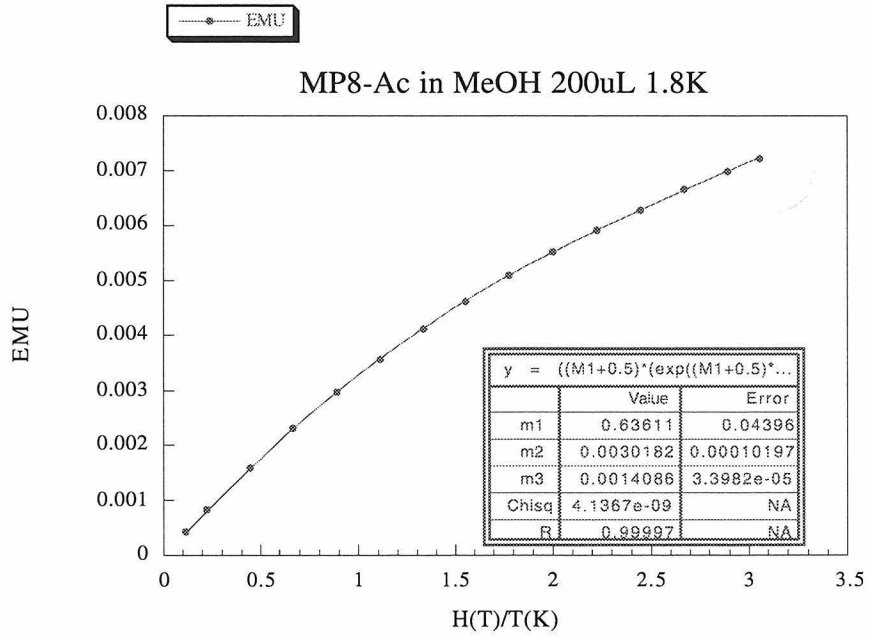
EMU
MP8-Ac in MeOH 200uL 1.8K
EMU
H(T)/T(K)
0.008
0.007
0.006
0.005
0.004
0.003
0.002
0.001
0
0
0.5
1
1.5
2
2.5
3
3.5
y = ((M1+0.5)*(exp((M1+0.5)*...
Value
Error
m1 0.63611 0.04396
m2 0.0030182 0.00010197
m3 0.0014086 3.3982e-05
Chisq 4.1367e-09 NA
R 0.99997 NA

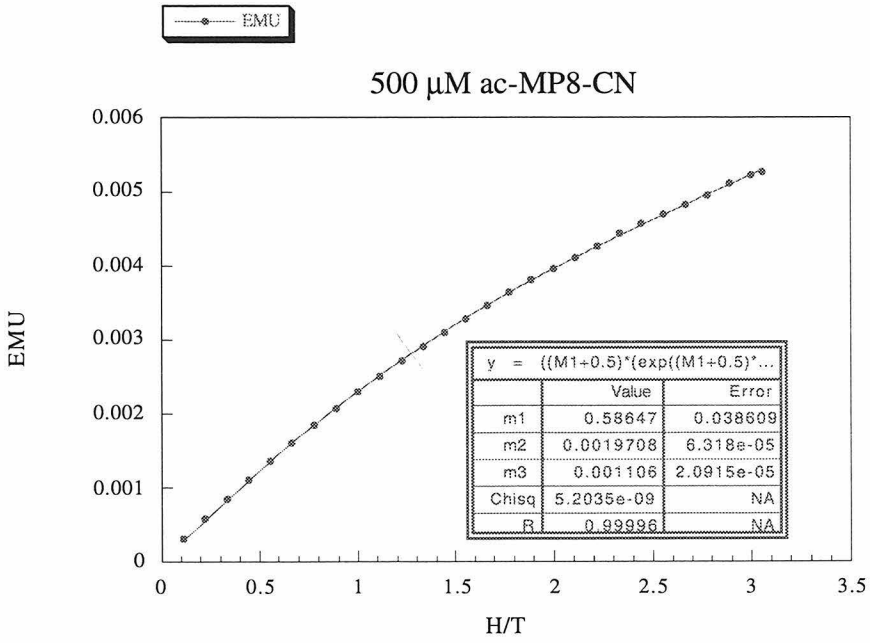
EMU
500 µM ac-MP8-CN
EMU
H/T
0.006
0.005
0.004
0.003
0.002
0.001
0
0
0.5
1
1.5
2
2.5
3
3.5
y = ((M1+0.5)*(exp((M1+0.5)*...
Value
Error
m1 0.58647 0.038609
m2 0.0019708 6.318e-05
m3 0.001106 2.0915e-05
Chisq 5.2035e-09 NA
R 0.99996 NA

spin state at low temperature, the error ranges for the two samples overlap, so within the error of the measurement, the two samples exhibit identical magnetic properties, and therefore the low temperature spin state of acetyl MP8 is S = 1/2.

The high, intermediate and low spin states of ferric iron porphyrins each has a characteristic EPR signature with significantly different g-values. X-band EPR spectra of ac-MP8 in a frozen methanol glass (77 K) were also consistent with the presence of a S = 1/2 state in equilibrium with an S = 5/2 state. Spectra taken feature both a resonance at approximately g = 6.1 characteristic of an axially-symmetric high spin system, as well as a rhombic signal at approximately g = 2 (g_X = 2.7, g_Y = 2.4, g_Z = 1.7), indicating the presence of a low-spin chromophore. No EPR signals in the region g = 3-4 were present as expected for a pure intermediate spin system.[23]

These studies of the magnetic properties monomeric acetyl MP8 in alcoholic solutions are in good agreement with those of Kassner and coworkers,[17] as well as with a recent study of the spin state of acetylated MP11 by Carraway et al.,[24] who conclude that both systems are S = 5/2 <-> S = 1/2 thermal equilibria. The results presented here are also easily reconciled with the observations of Munro and coworkers,[13] who conclude from the spectroscopic properties of acetyl MP8 in aqueous solutions that acetyl MP8 is a thermal equilibrium between a quantum admixed S = 5/2 <--> S = 3/2 state and an S = 1/2 state,[13] but differ significantly from those of Wang and coworkers who suggest the presence of an equilibrium between pure S = 5/2 and S = 3/2 spin states.[12] While we find no evidence for the S = 3/2 component of the quantum admixed high spin state proposed by Munro, the difference may be attributed simply to the nature of the solvent. Alcohols are known to be weaker field ligands than water, and the weaker ligand field should favor the S= 5/2 component of the quantum admixture. Our EPR and magnetic susceptibility measurements exclude the possibility of any significant contribution a pure S = 3/2 state in acetyl MP8 in methanolic solutions, and these results may be extended to neutral and acidic aqueous solutions. An S = 3/2 state is attained only in the cases of 5 coordinate porphyrin

complexes of a weak axial ligand; well characterized examples include 5-coordinated perchlorate complexes of tetraphenylporphyrins.[25] Since acetyl MP8 has no detectable S = 3/2 character in solutions of methanol, a weaker field ligand than water, it is unlikely that acetyl MP8 will form five-coordinate intermediate-spin complexes in aqueous solutions.

Conclusion

Both MP8 and MP9 fragments were successfully prepared from modified literature procedures, and their identities were confirmed by mass spectrometry. MP8 was also prepared in its acetylated form. The spin state of ferric MP8 in aqueous and mixed-aqueous alcoholic solvents appears to be predominantly an S = 5/2 <-> S = 1/2 thermal equilibrium, based on results from magnetic susceptibility, EPR and optical methods.

References and Notes

(1) Collman, J. P.; Gagne, R. R.; Reed, C. A.; Halbert, T. R.; Lang, G.; Robinson, W. T. *J. Am. Chem. Soc.* **1975**, *97*, 1427-1439.

(2) Collman, J. P.; Brauman, J. I.; Iverson, B. L.; Sessler, J. L.; Morris, R. M.; Gibson, Q. H. *J. Am. Chem. Soc.* **1983**, *105*, 3052-3064.

(3) Momenteau, M.; Reed, C. A. *Chem. Rev.* **1994**, *94*, 659-698.

(4) Tsuchida, E.; Komatsu, T. *Meth. Enzym.* **1994**, *231*, 167-193.

(5) Traylor, T. G.; Berzinis, A. P. *J. Am. Chem. Soc.* **1980**, *102*, 2844-2846.

(6) Adams, P. A.; Baldwin, D. A.; Marques, H. M. In *Cytochrome c : a multidisciplinary approach*; R. A. Scott and A. G. Mauk, Eds.; University Science Books: Sausalito, CA, 1996; pp 635-692.

(7) Tuppy, H.; Paleus, S. *Acta Chem. Scand.* **1955**, *9*, 353-364.

(8) Paleus, S.; Ehrenberg, A.; Tuppy, H. *Acta Chem. Scand.* **1955**, *9*, 365-374.

(9) Harbury, H. A.; Loach, P. A. *J. Biol. Chem.* **1960**, *235*, 3640-3645.

(10) Tuppy, H.; Bodo, G. *Monatshefte Chem.* **1954**, *85*, 1182-1186.

(11) Aron, J.; Baldwin, D. A.; Marques, H. M.; Pratt, J. M.; Adams, P. A. *J. Inorg. Biochem.* **1986**, *27*, 227-243.

(12) Wang, J.-S.; Tsai, A.-L.; Heldt, J.; Palmer, G.; Van Wart, H. E. *J. Biol. Chem.* **1992**, *267*, 15310-15318.

(13) Munro, O. Q.; Marques, H. M. *Inorg. Chem.* **1996**, *35*, 3752-3767.

(14) Othman, S.; Lirzin, A. L.; Desbois, A. *Biochemistry* **1993**, *32*, 9781-9791.

(15) Baldwin, D. A.; Marques, H. M.; Pratt, J. M. *J. Inorg. Biochem.* **1986**, *27*, 245-254.

(16) Wang, J.-S.; Van Wart, H. E. *J. Phys. Chem.* **1989**, *93*, 7925-7931.

(17) Huang, Y.-P.; Kassner, R. *J. Am. Chem. Soc.* **1981**, *103*, 4927-4932.

(18) Urry, D. W.; Pettegrew, J. W. *J. Am. Chem. Soc.* **1967**, *89*, 5276-5283.

(19) Peterson, J.; Saleem, M. M. M.; Silver, J.; Wilson, M. T. *J. Inorg. Biochem.* **1983**, *19*, 165-178.

(20) Baldwin, D. A.; Mabuya, M. B.; Marques, H. M. *S. Afr. J. Chem.* **1987**, *40*, 103-110.

(21) Carraway, A. D.; Burkhalter, R. S.; Timkovich, R.; Peterson, J. *J. Inorg. Biochem.* **1993**, *52*, 201-207.

(22) Blumenthal, D. C.; Kassner, R. J. *J. Biol. Chem.* **1980**, *255*, 5859-5863.

(23) Kintner, E. T.; Dawson, J. H. *Inorg. Chem.* **1991**, *30*, 4892-4897.

(24) Carraway, A. D.; McCollum, M. G.; Peterson, J. *Inorg. Chem.* **1996**, *35*, 6885-6891.

(25) Kastner, M. E.; Scheidt, W. R.; Mashiko, T.; Reed, C. A. *J. Am. Chem. Soc.* **1978**, *100*, 666-667.

Chapter 3: Paramagnetic NMR Spectroscopy of Microperoxidase-8

Introduction

The heme group of MP8 has been characterized extensively by spectroscopic methods.[1-7] One method that potentially could reveal information about both the octapeptide conformation and the heme electronic structure is paramagnetic NMR spectroscopy.[8,9] However, the NMR spectra of MP8 in buffered aqueous solutions are very poorly resolved, owing to extensive aggregation and the presence of a high-spin iron center.[10] These problems can be overcome by making measurements on the low-spin ferric-cyanide derivative[11] in methanolic solutions. Indeed, we have obtained highly resolved ^{1}H and ^{13}C NMR spectra of MP8 under these conditions. Analysis of the results suggests that the loop formed by residues 14-18 is extremely rigid and retains the gross structural features of the intact cytochrome, including a fixed axial ligand orientation.

Results and Discussion

As discussed in the previous chapter, acetyl MP8 appears be a predominantly S = 5/2 system in aqueous and methanolic solutions at room temperature. The ^{1}H NMR spectra of acetyl MP8 in aqueous phosphate buffer are highly complex: the resonances are extremely broad, and the sample appears to contain a heterogeneous mixture of species. Meso protons appear far upfield in the aqueous samples, suggesting the presence of 5-coordinate hemes in the mixture.[12] The ^{1}H NMR spectra of methanolic solutions of acetyl MP8 are also heterogeneous, with at least 2 distinct species present; however, the line widths have decreased dramatically, suggesting that aggregation is less significant in the presence of the methanol. In 70% d_4-MeOH, heme methyl resonances are found in the region corresponding to high-spin ferric hemes at 67.8, 67.2, 63.9 and 54.5 ppm (Figure 3.1). In addition, sharp resonances are found at 18.3 and 16.7 ppm that may be due to a low-spin ferric component present at the high concentrations used in NMR experiments. The upfield meso signals do not appear in the methanolic samples.

Figure 3.1 250 MHz ^{1}H-NMR spectrum of acetyl MP8 in d_4-methanol at 300 K.

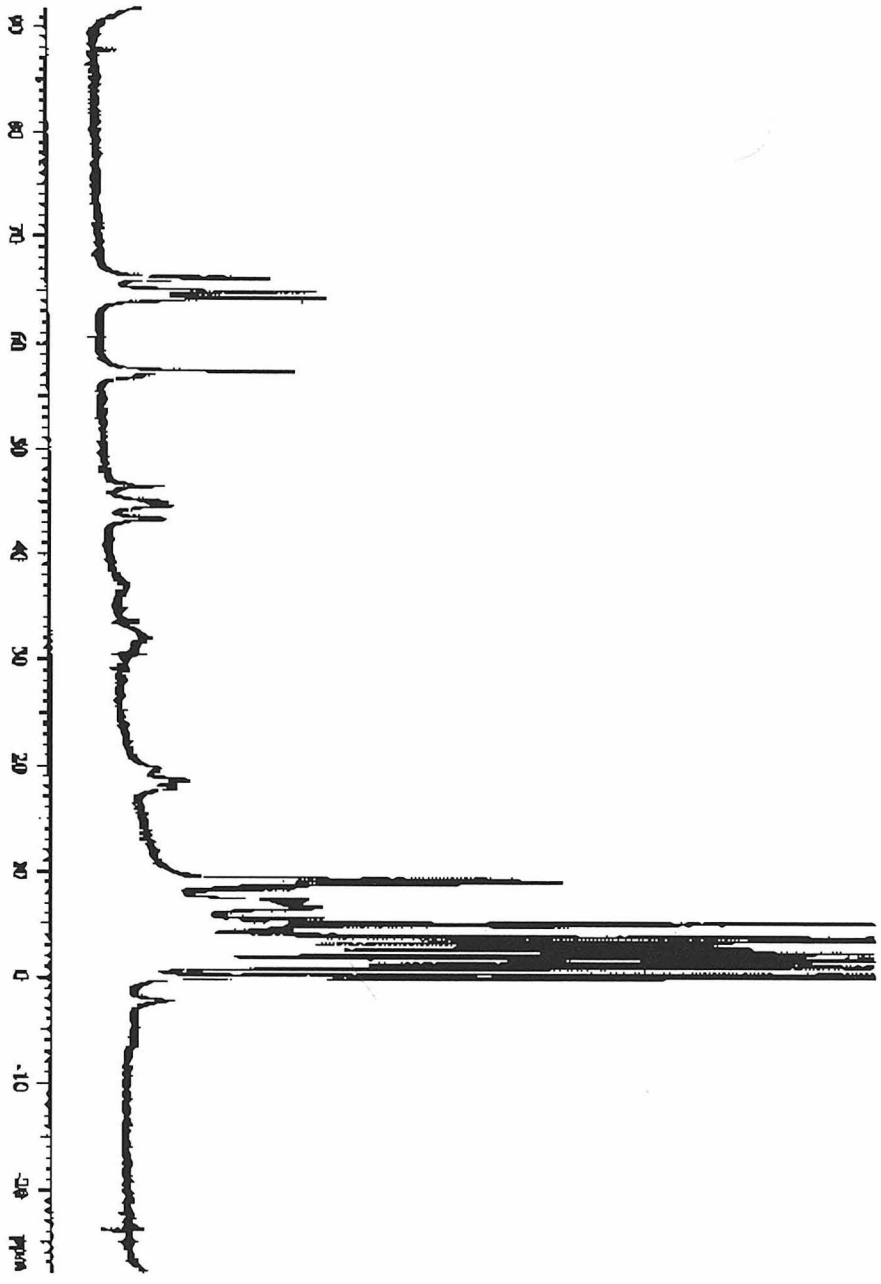
ppm
-10
0
10
20
30
40
50
60
70
80
90

Therefore, MP8 appears to be 6-coordinate in both high and low spin forms in methanol. Variable temperature experiments strongly indicate that the ferric center in acetyl MP8 under these conditions is a non-ideal magnetic center, possibly due to rapid exchange between aggregated and monomeric forms, or a thermal spin equilibrium process (*vide infra*).

In order to decrease the complexity of the samples for NMR investigation, axial ligands were added to NMR samples to favor the presence of monomeric species. Addition of excess sodium cyanide to a brown methanolic solution of MP8 results in a deep red species whose electronic absorption (Soret λ_{max} 410 nm) and resonance Raman (441.6 nm excitation, ν_4 = 1373, ν_3 = 1503, ν_2 = 1585, ν_{10} = 1642 cm^{-1}) properties are typical of a low-spin (S = 1/2) heme.[20] The 600 MHz 1-D ^1H NMR spectrum of a 5 mM solution of MP8-CN in 90% d_4-MeOH / 10% H_2O at 300 K is shown in Figure 3.2. Spectra taken of samples of MP8-CN in buffered aqueous solutions feature broad peaks that suggest extensive aggregation in solution, while spectra obtained from methanolic solutions have sharp spectral features, indicating minimal aggregation. The spectrum of MP8-CN features several peaks shifted well out of the diamagnetic envelope due to the effects of the paramagnetic ferric ion. The heme methyl substituents resonate between 10-25 ppm, a region typical for analogous S = 1/2 met-cyano heme proteins.[12] The heme substituents are expected to exhibit only dipolar couplings to each other, and therefore NOESY spectroscopy was employed to assign their resonances (Table 3.1). A NOESY spectrum with a 200 ms mixing time features a self-consistent set of NOESY cross peaks, leading to an unambiguous assignment of the heme substituents (Figure 3.3). The 3-proton-intensity signals at 16.4 and 23.2 ppm both show dipolar couplings to the upfield shifted 1-proton signal at - 0.99 ppm, and are therefore assigned to the methyl groups at positions 1 and 8 and the δ-meso proton, respectively. The methyl resonance at 21.7 ppm exhibits dipolar connectivities to a 1-proton signal at - 0.86 ppm (β - meso) and methylene protons at 3.42 and 4.36 ppm, and therefore is assigned as the 5-CH_3. The methyl resonance at 10.6 shows the dipolar connectivities expected for the 3-CH_3, with cross peaks to a 1-proton

Table 3.1: ^{1}H Chemical Shifts

A: Heme Substituents

Substituent	δ (ppm)
1-CH_3	16.41
2α-H	0.89
2β-CH_3	0.74
α-meso	4.67
3-CH_3	10.57
4α-H	-0.63
4β-CH_3	0.27
β-meso	-0.86
5-CH_3	21.73
6α-CH_2	3.42, 4.36
6β-CH_2	0.81, 0.91
γ- meso	8.09
7α-CH_2	4.20, 4,68
7β-CH_2	1.05, 1.20
8-CH_3	23.24
δ-meso	-0.99

B: Peptide Resonances (ppm)

Residue	amide	α	β1	β2	γ	other
Cys 14		2.82	2.71	3.12		
Ala 15	-	5.61	1.90			
Gln 16	10.36	4.39	1.85	2.01	2.28	6.76, 7.42
Cys 17	7.87	5.36	1.05	2.31		
His 18	11.16	9.39	8.72	11.80		
Thr 19	9.74	5.49	4.98		1.91	
Val 20	9.08	4.95	2.69		1.48	1.52
Glu 21	8.46	4.71	2.42	2.54	2.72	

Figure 3.2: 250 MHz ^{1}H-NMR spectra of MP8-CN (5 mM MP8, 15 mM KCN) in d_4-methanol at 300 K before (upper spectrum) and after (lower spectrum) the addition of 10% H_2O. Heme methyl resonances are labeled A-D; paramagnetically shifted His18 resonances are labeled E-G; γ, β, and δ meso proton resonances are labeled H, I, and J, respectively. Resonance K is due to the heme 4α proton. The resonances that appear between 7-12 ppm upon addition of water are backbone and Gln amide protons.

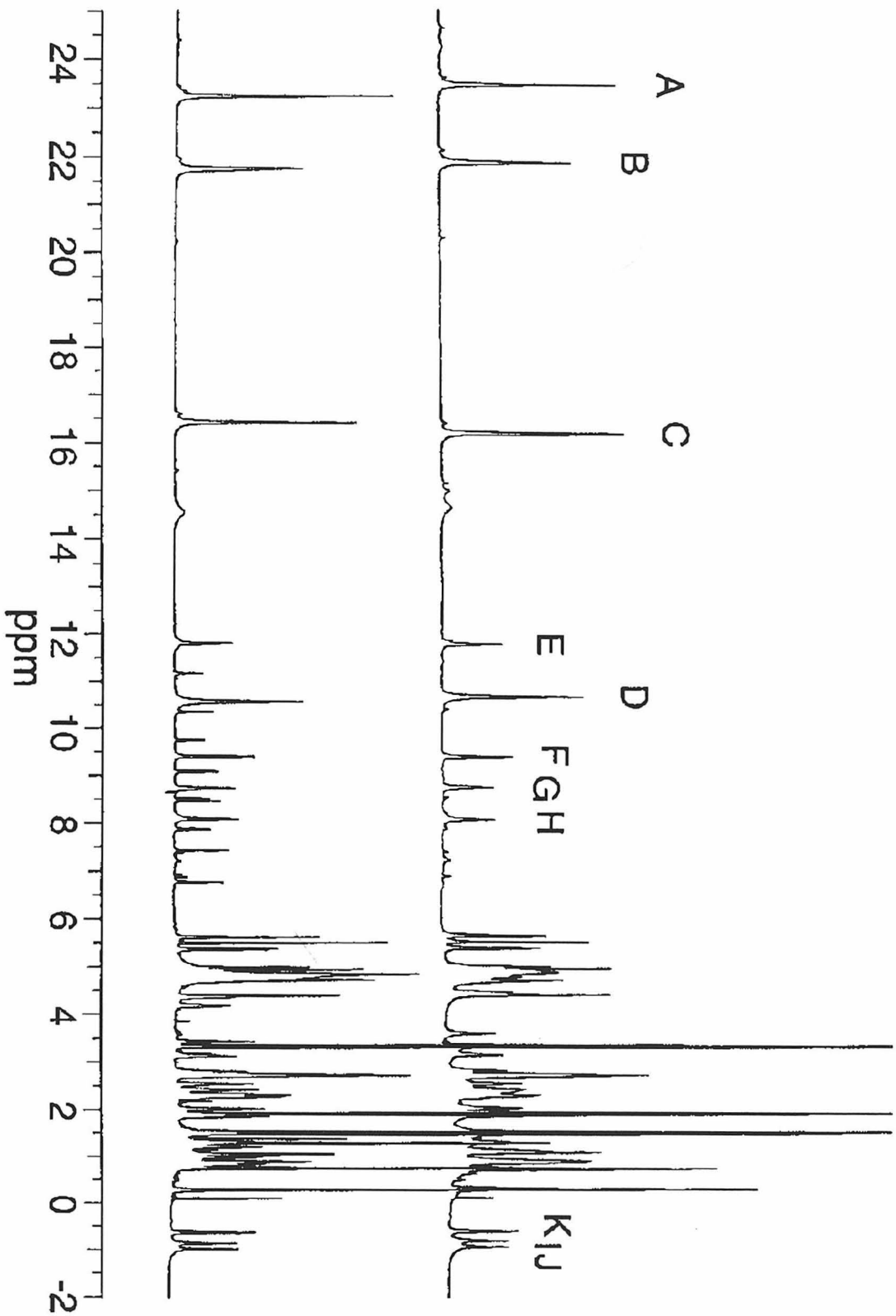
A
B
C
D
E
F
G
H
I
J
K
24
22
20
18
16
14
12
10
8
6
4
2
0
-2
ppm

Figure 3.3: 600 MHz NOESY spectrum of MP8-CN in d_4-methanol at 300 K. 200 ms mixing time.

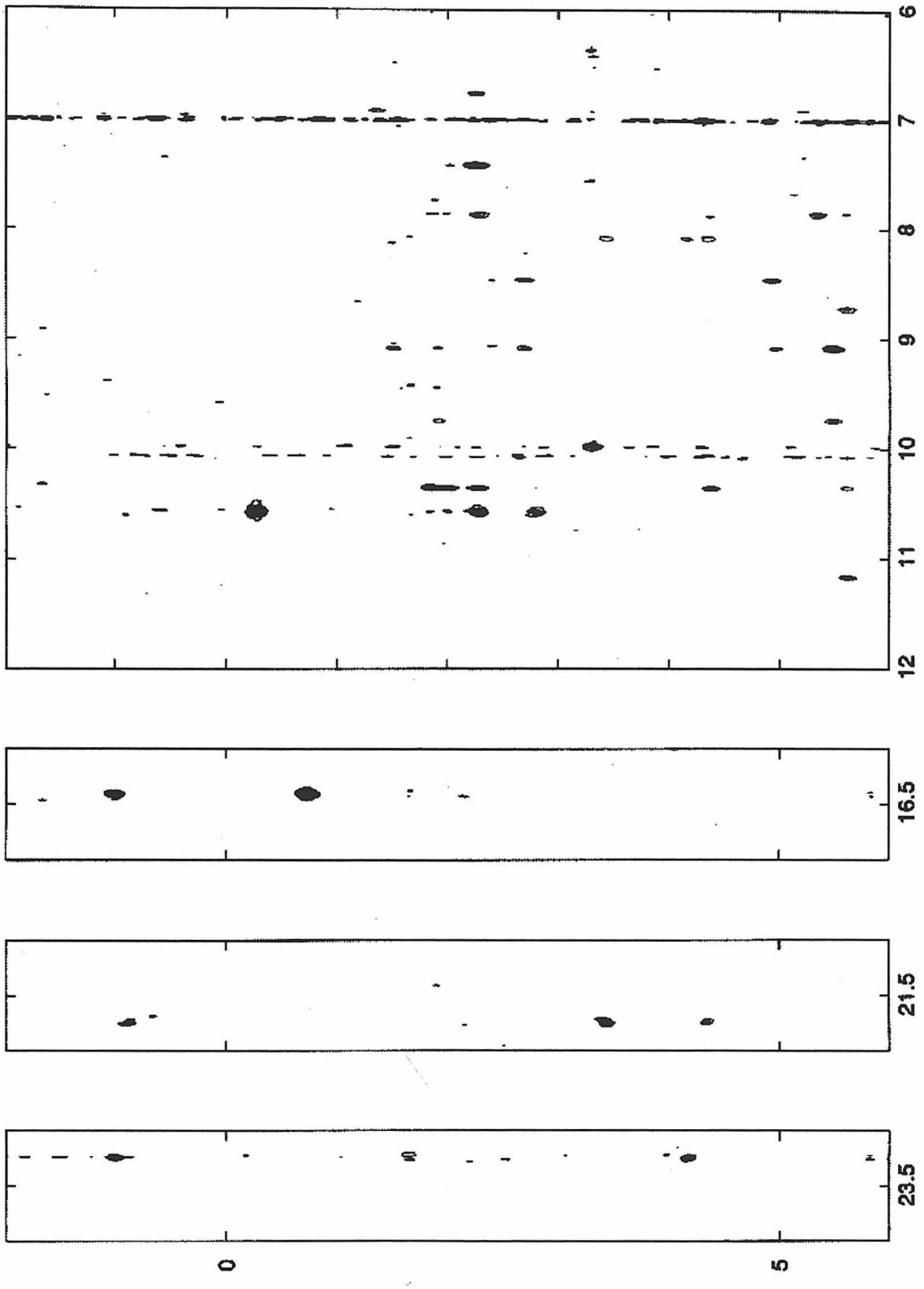
6
7
8
9
10
11
12
16.5
21.5
23.5
0
5

singlet at 4.67 ppm (α-meso) and to the 4β-CH_3. The resonance at 23.2 ppm exhibits a NOESY cross peak to protons assigned to a propionate methylene unit, establishing its identity as the 8-CH_3. In contrast to the sample of acetyl MP8 without cyanide, the four heme methyl resonances of MP8-CN were found to obey the Curie law in VT experiments over a wide range of temperatures (Figure 3.4), indicating that the binding of cyanide to the iron center results in an exclusively low-spin heme, as expected. Deviations from the Curie dependence at higher temperatures may be due to dissociation of cyanide or the axial H18 ligands. Acetyl MP8 was found to have markedly non-linear behavior for its heme methyl groups. The chemical shifts still tend to increase with decreasing temperatures, and the behavior seen here for acetyl MP8 is qualitatively different from that found for the heme methyls of spin-equilibrium systems that exhibit anti-Curie temperature dependences.[13,14]

The observed pattern of heme substituent chemical shifts is very similar to those observed in the cyanide-bound forms of *Saccharomyces cerevisiae* Ala80 iso-1-cytochrome *c* (Ala80-y-cyt *c*), h-cyt *c,* and MP11 (Table 3.2). The methyl groups of MP8 resonate with a mean shift of 17.99 ppm and a spread of 12.3 ppm, compared with a mean shift of 17.1 ppm and a spread of 11.3 ppm for MP11, and a mean shift of 17.1 ppm and spread of 11.2 ppm for met-cyano Ala80-y-cyt *c*.[15-17] The chemical shift dispersion and mean chemical shift of the heme methyls are largely determined by the fixed orientations of the heme axial ligands. Freely rotating or axially symmetric ligands result in relatively small values for mean shift and spread: ferric hemin imidazole cyanide has a spread of only 4.6 ppm and a mean methyl shift of 11.0 ppm.[18] After the replacement of methionine with an axially symmetric ligand such as cyanide, the imidazole orientation is then the primary factor in determining the rhombic axes. The similarity of the results for cyanide derivatives of MP8, Ala80-y-cyt *c*, and h-cyt *c* indicates a common fixed imidazole orientation in the heme *c* systems with the imidazole ring plane aligned with the α and γ meso positions. Our finding that the gross orientation is preserved even in the absence of a large portion of the polypeptide chain, including Pro30, reported to provide a hydrogen bond to the

Figure 3.4: Curie plots for both Fe(III)-cyano MP8 and acetyl MP8 in d_4-methanol. The MP8-CN Curie plots only deviate from ideal magnetic behavior at high temperatures. The temperature dependence of the heme methyl chemical shifts of acetyl MP8l; however, are likely to be non-linear due to equilibrium between monomeric and aggregated forms of the peptide.

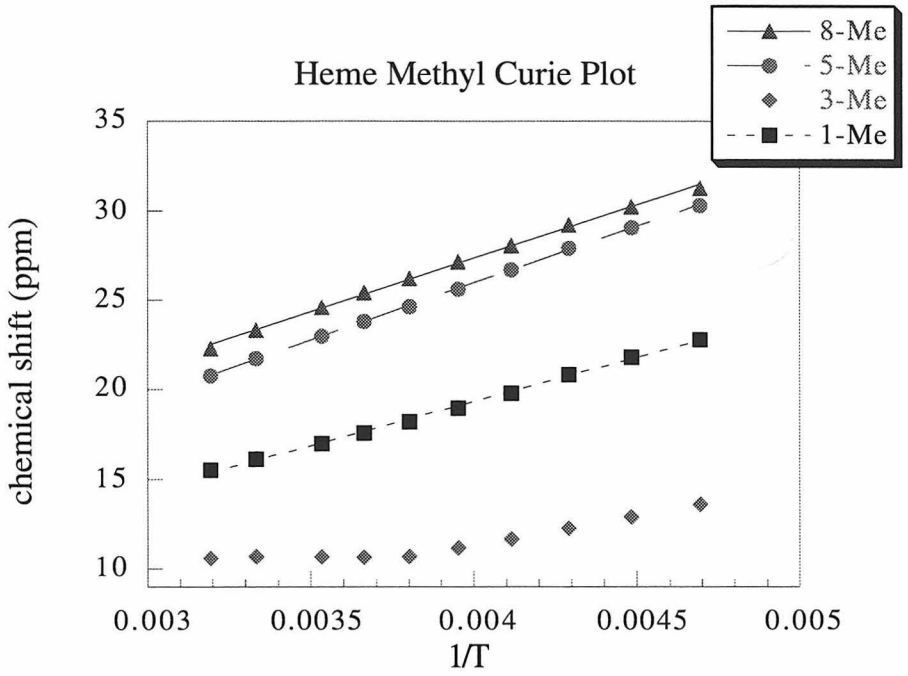
Heme Methyl Curie Plot
8-Me
5-Me
3-Me
1-Me
chemical shift (ppm)
35
30
25
20
15
10
0.003
0.0035
0.004
0.0045
0.005
1/T

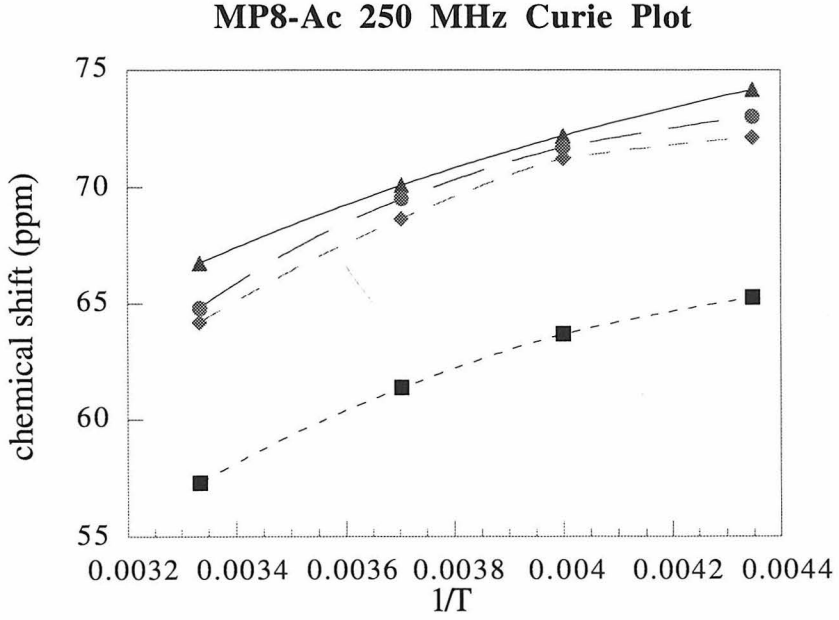
MP8-Ac 250 MHz Curie Plot
chemical shift (ppm)
75
70
65
60
55
0.0032
0.0034
0.0036
0.0038
0.004
0.0042
0.0044
1/T

Table 3.2: Comparison of Heme Methyl ^{1}H Chemical Shifts*

	Mean Shift (ppm)	Dispersion (ppm)
MP8-CN	17.99	12.3
MP11-CN	17.14	11.3
Ala80-y-cyt *c*- CN	17.10	11.2
ferric hemin-Im-CN	11.03	4.6

	Methyl Chemical Shift (ppm)
MP8-CN	(8) 23.2; (5) 21.7; (1) 16.4; (3) 10.6
Ala80-y-cyt *c*-CN	(8) 22.5; (5) 19.5; (1) 15.4; (3) 11.3

* ^{1}H δ values for MP11-CN, Ala80-y-cyt *c*-CN, and ferric hemin-Im-CN from refs. 15-17.

imidazole,[19] suggests that the rigid loop of residues 14-18 fixes the orientation of the axial imidazole, modulating the distribution of heme spin density.

^{13}C NMR spectroscopy has been employed to investigate paramagnetic heme systems.[20-23] Studies have focused on heme methyl chemical shifts, since, to a first approximation, dipolar contributions to their chemical shifts may be neglected and only the contact contribution from the iron need be considered. An HMQC spectrum of MP8-CN in methanol-d_4 is shown in Figure 3.5. The paramagnetic shifts felt by heme substituents in MP8 are paired: substituents on opposite sides of the porphyrin ring experience similar paramagnetic shifts (Figure 3.6). Turner has observed a similar phenomenon in the ^{13}C spectra of ferricytochrome c_3, in which axial imidazoles are found oriented along the α–γ meso axis.[21] An examination of the crystal structure of native cytochrome *c* reveals that the histidine in this case is also oriented along the α–γ meso axis;[24] and our data confirm that this orientation is preserved even in the MP8 active site (Figure 3.7).

In principle, NMR spectroscopy can be used to determine the orientation of the principle magnetic axes of the heme iron. A commonly used method uses the chemical shifts of peptide residues in both diamagnetic and paramagnetic forms in conjunction with coordinates from X-ray crystal structures to determine the dipolar shifts experienced by resonanting protons at various points in the protein structure.[25] A least-squares fitting routine is then used to determine the magnitudes and orientation of the magnetic axes. Information on the iron magnetic tensor may be also be extracted from an analysis of EPR g-values and dipolar shifts of the heme methyl carbons.[21] The metal-centered contact shift contribution to the total chemical shifts of the heme methyl carbons is estimated by separating the diamagnetic shift contribution from the total observed shift. The contributions from dipolar shifts and ligand centered contact shifts are considered negligible. Turner describes the contact shift contribution to the heme methyls in terms of 5 parameters, c_1 and c_5, the coefficients of the wavefunctions for the two porphyrin LUMO's at the pyrrole positions, assuming a D_{4h} symmetric porphyrin (assigned fixed

values of 0.164 and 0.074); ε, a Boltzman constant related to the energy separation between the two LUMO's under a rhombic perturbation that lifts their degeneracy; Q the electron-nuclear hyperfine coupling constant and θ, the orbital mixing parameter, related to the orientation of the magnetic axes.[26]

From this analysis, (the z axis was assumed to be approximately normal to the heme plane) y for the MP8 heme was estimated to be -41.2°. Thus, the magnetic y axis lies roughly along the heme meso α–γ axis with a slight tilt towards pyrrole positions 3 and 7 (Figure 3.8). Using this magnetic tensor in conjunction with the coordinates from the crystal structure of h-cyt *c*, the magnitude of dipolar shifts can be estimated using Eq. 1:

$$(1)\ \frac{\Delta B}{B} = \frac{\mu_0}{8\pi N_A |r|^3}\left[2\chi_z/3 - \chi_x/3 - \chi_y/3)(1 - 3\cos 2\theta) + (\chi_y - \chi_x)\sin 2\theta \cos(2\phi)\right]$$

Where N_A is Avagadro's number, χ_q is magnetic susceptibility along axis q, and r, θ and ø are the polar coordinates that define the position of the resonating nucleus, with the iron atom as the origin. A comparison of the calculated and observed MP8 ^{1}H shifts based on the h-cyt *c* structure (using reduced h-cyt *c* as a diamagnetic reference) is shown in Table 3.3 and graphically in Figure 3.9. The chi value between the observed and calculated shifts is a very rough measure of the deviation from the crystal structure position for a particular group in MP8, taking into account both the magnitude of the difference observed, as well as the gradient of the dipolar field near the resonanting nucleus.[27] The chemical shifts for the valine methyl groups were averaged in this calculation. Chi values tend to be larger at the C terminus and smaller in the 14-18 region, consistent with our prediction from NOE's that the 14-18 region is structurally intact in MP8. The calculation is least reliable for amide protons, since these are expected to have significant chemical shift differences due to solvent interactions (e.g. hydrogen bonding).

All of the resonances from the peptide portion of MP8 except those of His18 fall within the diamagnetic region, and assignments were made with a combination of 2-D methods (Table 3.1b). The effects of iron paramagnetism are also reflected in the His18

proton relaxation times (Table 3.4). Isolated spin systems were located in TOCSY spectra corresponding to each of the eight amino-acid residues (Figure 3.10). In neat d_4-MeOH solutions, no resonances are observed due to amide protons; however, upon addition of 10% H_2O to methanolic solutions, 9 new resonances are observed in the 5-10 ppm region where amide proton resonances are expected, and these are assigned to the amide protons of Cys14, Gln16, Cys17, His18, Thr19, Val20, and Glu21. Amide proton resonances from residues within the region of the peptide loop anchored to the heme show informative amide-α J couplings: Cys17 ^3J = 11 Hz; Gln16 ^3J = 4.7 Hz; His18 ^3J = 7.7 Hz. For comparison, coupling constants were calculated using the Karplus relation;[28] torsional angles were taken from the crystal structure of h-cyt c.[24] Reasonable agreement between calculated and experimental J values was found for amide protons in the 14-18 loop, providing additional support for our finding that the structure of this loop in native cytochrome is retained in the peptide (Table 3.5). Dipolar couplings observed between heme thioether substituents are consistent with rigid conformations at heme positions 2 and 4: strong NOESY cross peaks are observed between the 2-β CH_3 and the 1-CH_3 and a medium intensity cross peak is observed between the 2-α methine and the α-meso protons. The 4-α methine proton shows a strong cross peak to the β-meso proton and the 4-β CH_3 dipole couples strongly to the 3-CH_3. Eleven interresidue NOESY cross peaks and eleven additional cross peaks between peptide and heme substituents were located and qualitatively classified in spectra taken in 90% d_4-MeOH/ 10% H_2O solutions (Table 3.6).

NOESY spectra of Ala80-y-cyt c feature four cross peaks from heme pyrrole and meso substituents to peptide residues in the loop region.[17] Three of these involve cysteine α and β protons on the peptide; these also appear in NOESY spectra of MP8-CN. The fourth contact involves the ε and γ protons of Gln16, and its absence in spectra of MP8-CN is likely due to a change in the conformation of the flexible side chain. At least one sequential interresidue NOE was found to each of the amino-acid residues except His18. Of the eleven interresidue NOE correlations found, eight arise from contacts within the

Figure 3.5: 600 MHz ^{1}H-^{13}C HMQC spectrum of 5 mM MP8-CN, d_4-methanol, 300 K.

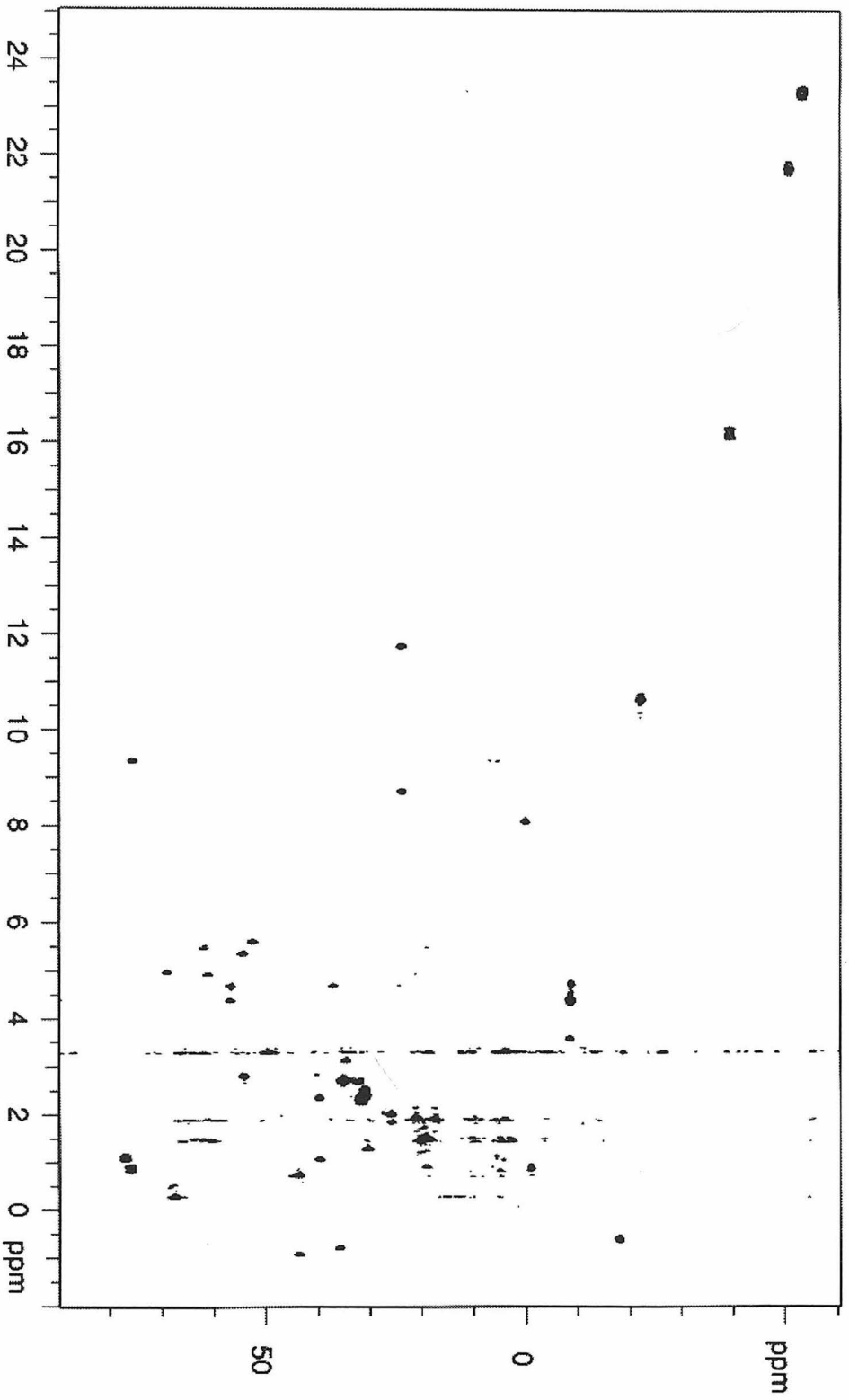
24
22
20
18
16
14
12
10
8
6
4
2
0 ppm
50
0
ppm

Figure 3.6: Estimated paramagnetic ^{13}C chemical shifts of heme substituents.

Heme Substituent ^{13}C Paramagnetic Shifts

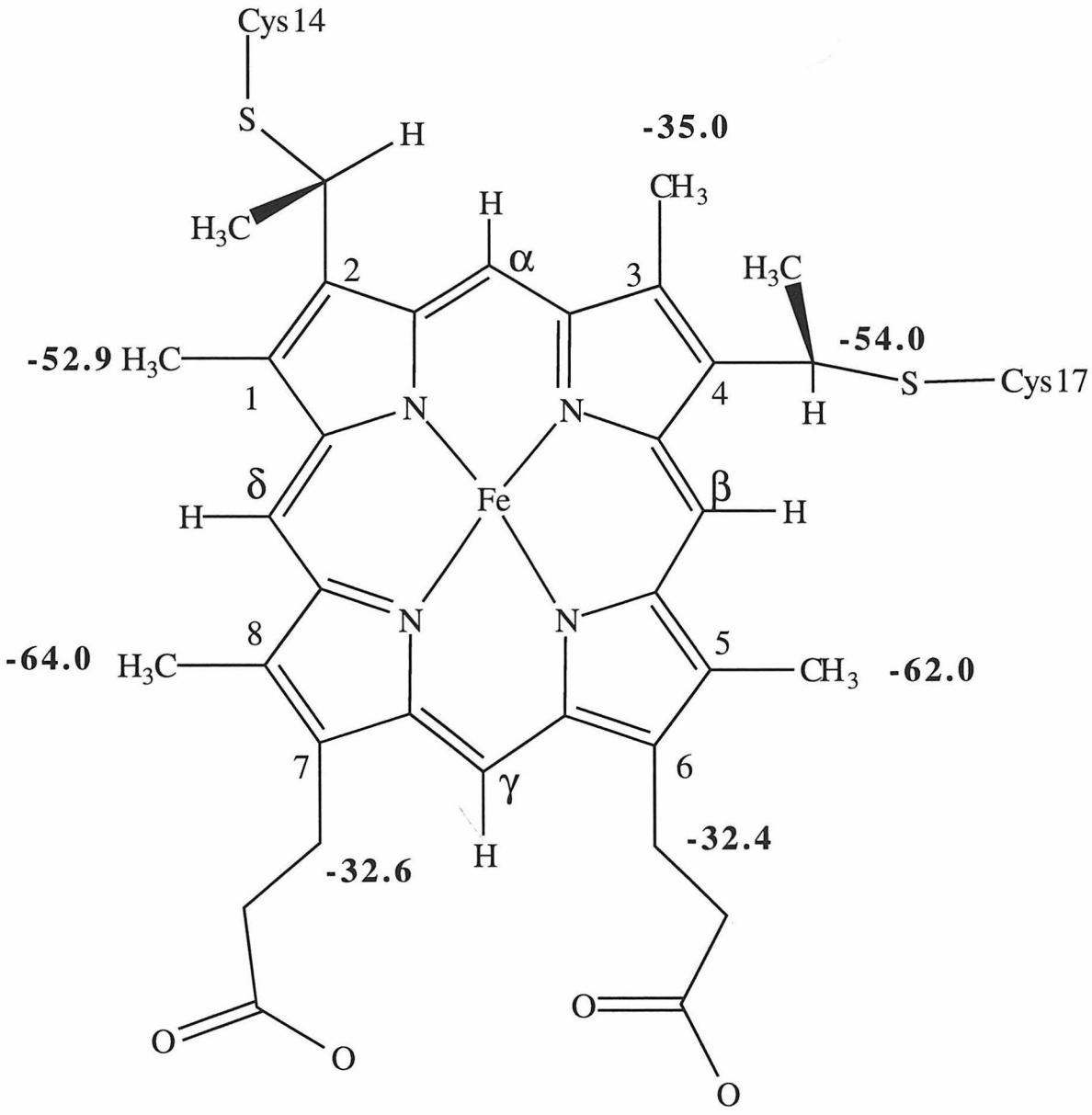

Figure 3.7: Top: Structure of h-cyt *c* with heme and residues 14-21 highlighted (coordinates from ref. 24). Middle: Fragment of h-cyt *c* structure corresponding to MP8. Bottom: Orientation of the His18 imidazole in h-cyt *c*.

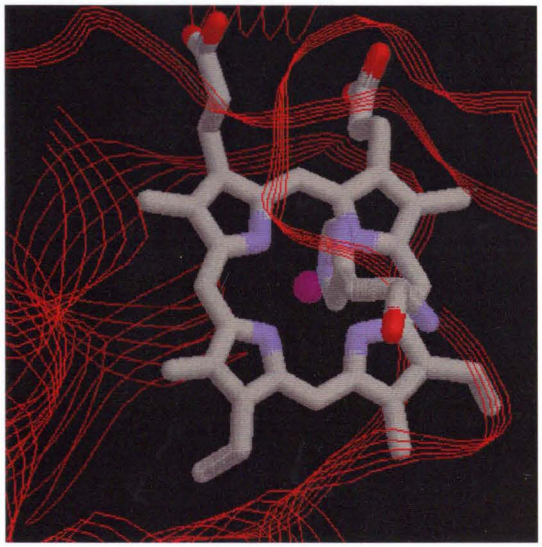

Figure 3.8: The orientation of the magnetic tensor y axis in relation to the heme *c* in MP8-CN is indicated by the arrow. The z axis of the tensor is assumed to be perpendicular to the heme normal.

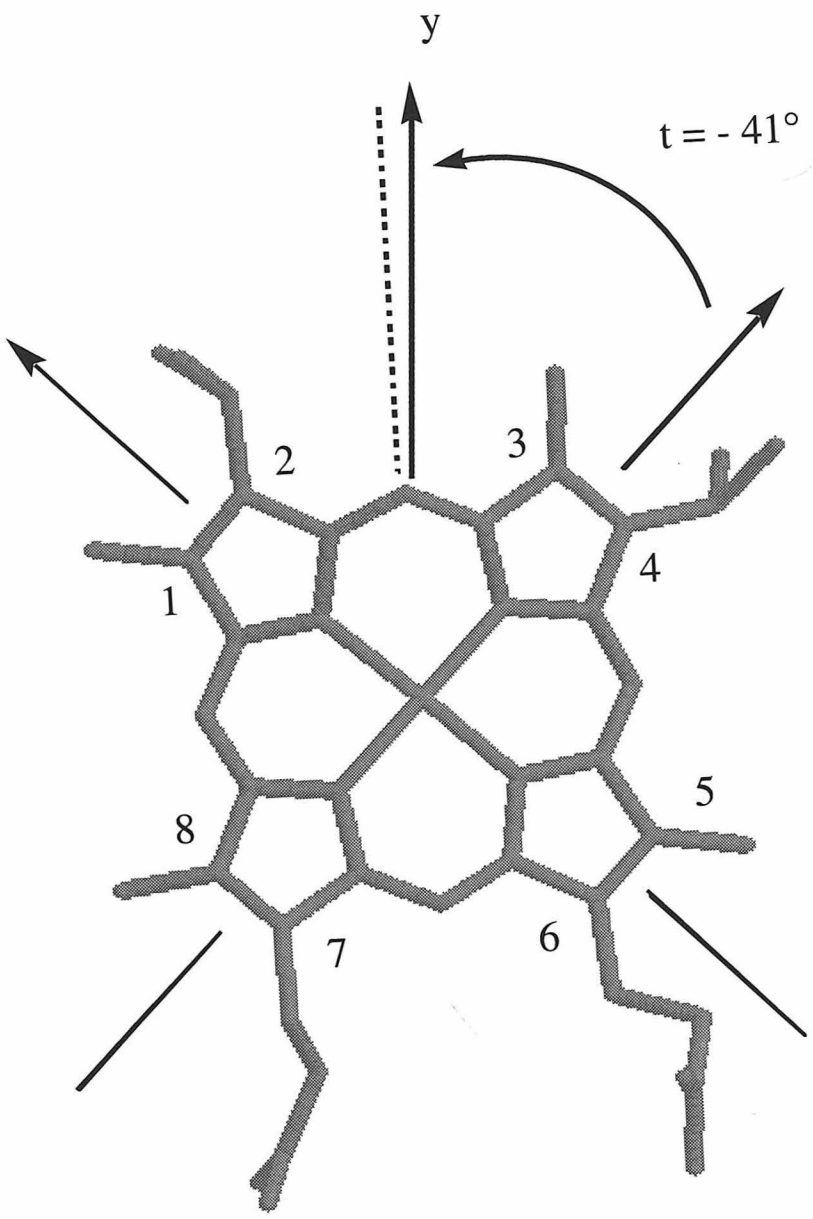
y
t = - 41°
1
2
3
4
5
6
7
8

Table 3.3: Observed and Calculated Dipolar Shifts for Peptide Protons

Residue	Proton	δ_{dip} observed	δ_{dip} calculated	chi
Gln16	NH	0.338	1.64	5.77
Cys17	NH	1.841	0.96	1.23
His18	NH	4.161	4.82	0.64
Thr19	NH	3.189	1.82	2.80
Val20	NH	1.080	1.23	0.94
Glu21	NH	0.751	-0.55	13.36
Cys14	Hα	-1.025	-2.14	1.54
Ala15	Hα	1.486	1.88	1.21
Gln16	Hα	0.352	0.44	0.62
Cys17	Hα	1.206	1.13	0.12
His18	Hα	7.278	5.75	0.90
Thr19	Hα	1.752	0.83	3.45
Val20	Hα	1.005	1.00	0.03
Glu21	Hα	0.386	0.40	0.27
Cys14	Hβ	-0.291	2.47	2.6
Ala15	Hγ	0.502	0.59	0.79
Gln16	Hβ	-0.286	-0.18	0.66
Cys17	Hβ	-1.135	0.64	0.76
His18	Hβ	7.640	9.38	0.85
Thr19	Hβ	1.287	0.48	4.75
Thr19	Hγ	1.029	0.81	1.73
Val20	Hβ	0.405	1.31	7.89
Val20	Hγ	0.607	1.54	5.84
Glu21	Hβ	0.362	0.30	1.50

Figure 3.9: Magnitudes of chi (the deviation between calculated and observed dipolar shifts based on the magnetic tensor derived from ^{13}C contact shifts and EPR g-values for MP8-CN and h-cyt *c* crystal structure coordinates) plotted against residue number and classified by proton type. Light solid fill: alpha protons; medium solid fill: side-chain gamma protons; dark solid fill: beta protons; crosshatched fill: amide protons.

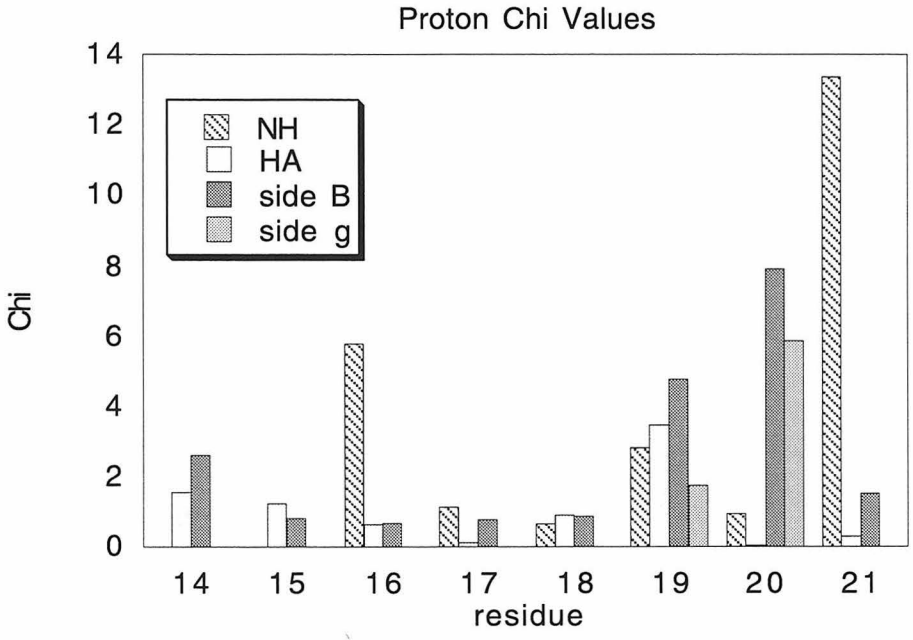
Proton Chi Values
Chi
14
12
10
8
6
4
2
0
NH
HA
side B
side g
14
15
16
17
18
19
20
21
residue

Table 3.4: Selected ^{1}H Relaxation Times (ms) at 250 MHz

Resonance	T_1	T_2
5-CH_3	83	41
1-CH_3	110	n/d
3-CH_3	127	53
γ-meso	36	38
β-meso	47	30
Cys14β	257	n/d
Ala15α	206	227
Ala15β	278	n/d
Gln16γ	186	n/d
Cys17α	381	n/d
His18β	60	n/d
His18α	126	n/d
Thr19γ	281	118
Val20γ	276	n/d

Figure 3.10: 600 MHz TOCSY spectrum of 5 mM MP8-CN in d_4-methanol at 300 K. 80 ms spinlock time, DIPSI spinlock.

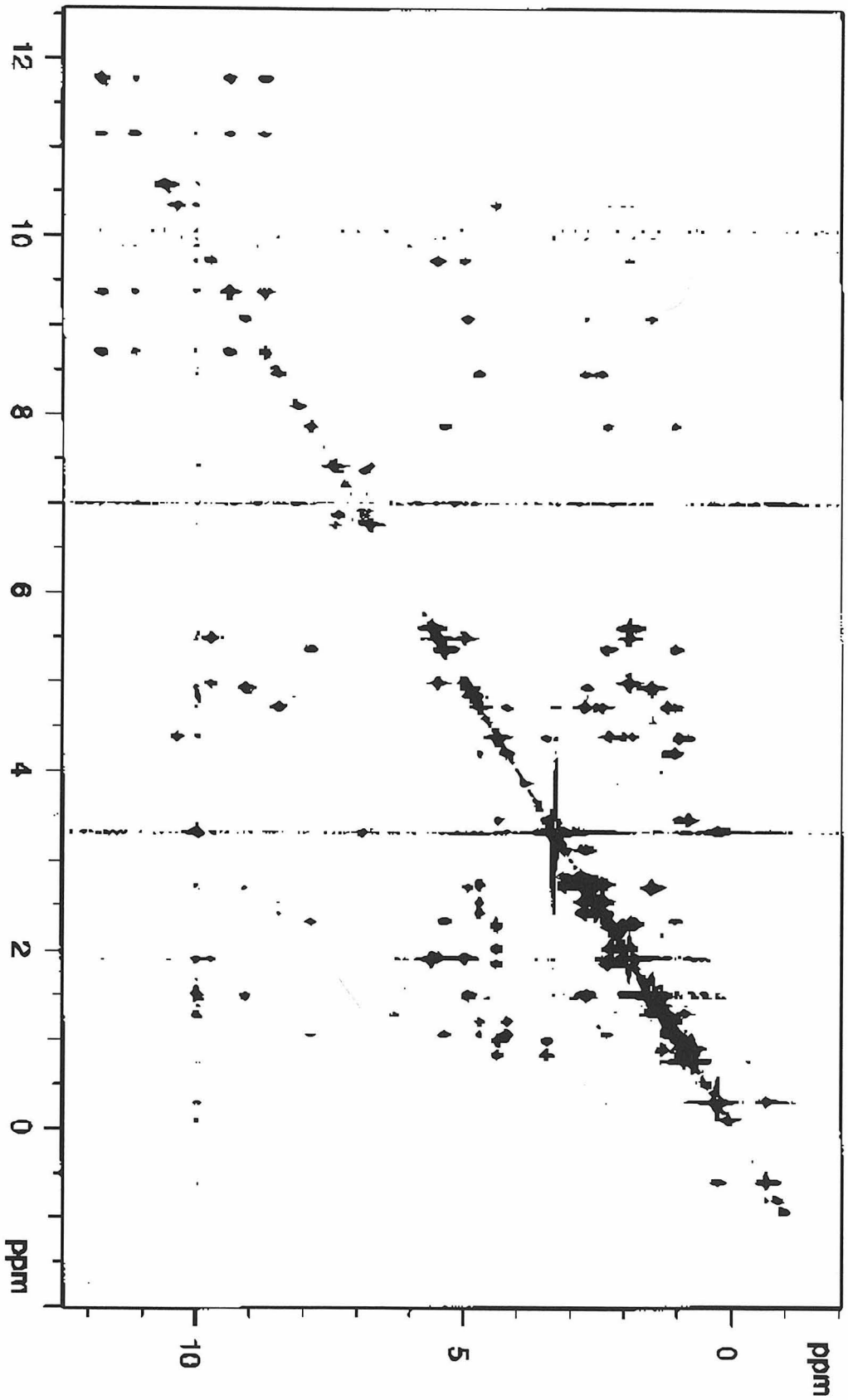
12
10
8
6
4
2
0
ppm
10
5
0
ppm

Table 3.5: Amide-H - Hα Coupling Constants

Residue	∠ NH – Hα (deg)*	Calculated $J_{HH'}$ (Hz)**	Observed $J_{HH'}$ (Hz)
Gln16	-124.4	4.7	4.7
Cys17	178.3	9.7	11.0
His18	143.0	7.1	7.6
Thr19	178.4	9.7	7.3
Val20	171.7	9.6	8.3
Glu21	-149.1	7.8	7.3

* From the crystal structure of h-cyt *c* (ref. 24).

** Calculated using the Karplus equation (ref. 31) and H-N-C-H torsional angles obtained from the h-cyt *c* crystal structure (ref. 28).

Table 3.6A: Heme-Peptide NOE Contacts

Heme Substituent	Peptide Substituent	Intensity Classification
2α	Cys14 α	M
2β	Cys14 α	W
2α	Cys14 β1	W*
α-meso	Cys14 α	W*
3-CH_3	Cys14 α	M
3-CH_3	Gln16 γ	M
3-CH_3	Gln16 β2	W
3-CH_3	Gln16 NH	VW
4α	Cys17 β1	M*
β-meso	Cys17 β1	VW
4β	Cys17 β	VW

*Correlation also found in Ala80-y-cyt *c* (ref. 24).

Table 3.6B: Interresidue NOE Contacts

Peptide Substituents	Intensity Classification
Cys14 β1, Ala15 α,	W
Ala15 α - Gln16 NH,	W
Gln16 α- Cys17 NH,	W
Cys17 NH - His18 NH,	W
Thr19 α- Val20 NH,	S
Thr 19 β - Val20 NH,	W
Val20 α- Glu21 NH,	W
Val20 β - Glu21 NH,	VW
His18 β1 - Ala15 β,	W
His18 β1 - Ala15 α,	M
His18 NH - Ala15 α,	W
Cys17 NH - Ala15 α,	W

VW = very weak, W = weak, M = moderate, S = strong

Cys-Ala-Gln-Cys-His region, consistent with a rigid loop conformation. Two sets of resonances from Ala15 and His18 show NOE contacts across the 14-18 loop. Similar intermediate-range NOESY contacts are found between residues 15 and 18 of Ala80-y-cyt *c* and oxidized h-cyt *c*.[29,30] Outside the loop formed by residues 15-18, Val20 was found to have a large amide-α coupling, 8.7 Hz, and the other amide protons show couplings to neighboring alpha protons of approximately 7 Hz, typical of fast rotational averaging on the NMR time scale, consistent with a more flexible C-terminal peptide domain.[34]

Conclusion

While the orientation of the methionine in native cytochrome *c* is believed to be the major determining factor in heme electronic asymmetry, recent work has shown that the fixed histidine orientation may also be important.[21] Heme electronic asymmetry could play a role in electron transfer by modulating the electronic coupling to the heme iron,[31] suggesting a functional role for imidazole orientation in these reactions. Immobilization of an axial ligand also will minimize changes in metal-ligand bond lengths and lower the inner-sphere reorganization energy associated with oxidation or reduction of the heme.[32] The heme and loop region 14-18 comprise a minimal heme active site that retains structural integrity even when isolated from its protein matrix, as reflected in the protein-like NMR spectroscopy of MP8. This rigid loop is highly conserved among *c* cytochromes and perhaps has evolved to orient the axial imidazole along the α–γ meso axis and modulate electron flow through the protein.

Experimental Section

Preparation of ferric MP8-CN. Microperoxidase-8 was prepared by peptic and tryptic digestion of h-cyt *c* (Sigma) and purified by reverse-phase FPLC as described previously.[33] A three-fold excess of solid sodium cyanide was added to NMR samples. Methanol-d_4 and D_2O were used as received from Cambridge Isotopes.

NMR Spectroscopy. ^1H NMR experiments were performed at 250.13 (DRX 250) and 600.13 MHz (AMX 600) on Bruker instruments, both with VTU2000 temperature control units; $1D^{13}C$ spectra were obtained on an AM 500 spectrometer operating at 125.7 MHz. Accurate temperature control proved to be important for stability in 2D experiments, as several signals are very temperature sensitive. All experiments were done at 300 K. Assignments were made using Pronto software (Carlsberg) on Silicon Graphics Indigo workstations.[34] All experiments were performed with presaturation of the water signal by Gaussian-shaped selective pulses offset from the carrier frequency by phaseramps, using built-in Bruker software. One-dimensional ^1H spectra were acquired using sweep widths up to 20000 Hz at 600 MHz and 12500 Hz at 250 MHz. Two-dimensional ^1H spectra were obtained with sweep widths of 17850 Hz in both dimensions at 600 MHz, 4k points in F2 and 1k points in F1. The data were processed using standard Bruker software with zerofilling to a final size of 2k x 2k complex points, and the data were multiplied by shifted squared sinebell windowfunctions prior to Fourier transform. NOESY spectra[35] were obtained with several mixing times from 50 to 300 ms, a presaturation time of 900 ms, and 32 to 48 scans per increment. TOCSY spectra were obtained using a DIPSI spinlock[36] with a spinlock power of 6000 Hz, a spinlock time of 80 ms, and 40 scans per increment. For both types of 2D spectra, quadrature detection in F1 was done by the Ruben-States-Haberkorn method.[37] Nonselective ^1H T_1 measurements[38] were made both at 250 and 600 MHz using the inversion-recovery method and 16 different delays from 100 μs to 5 s,

with a 5-s delay between scans. The data were analyzed using standard Bruker software with a 3-variable parameter fit. Estimates of T_2 relaxation times were made with a CPMG sequence[39] fitting the data to a single exponential decay. Assignments of ^{13}C data were based on 2D HMQC spectra measured both at 250 and 600 MHz. The sweep width in F1 was 42000 Hz at the 150.9 MHz resonance frequency for ^{13}C on the AMX600 and this was covered by 256 points using TPPI quadrature detection[40] and 420 scans per increment. The points were extended to 512 real points prior to Fourier transform by linear prediction and zerofilled to a final size of 2k x 2k complex points. The orientation of the magnetic tensor axes was determined by Professor David Turner of the University of Southhampton, UK.

References and Notes

(1) Wang, J.-S.; Wart, H. E. V. *J. Phys. Chem.* **1989**, *93*, 7925-7931.

(2) Silin, V. I.; Talaikyte, Z.; Kulys, J. *Vibrational Spectroscopy* **1993**, 345-351.

(3) Othman, S.; Lirzin, A. L.; Desbois, A. *Biochemistry* **1994**, *33*, 15437-15448.

(4) Kintner, E. T.; Dawson, J. H. *Inorg. Chem.* **1991**, *30*, 4892-4897.

(5) Kobayashi, N.; Osa, T. *Chem. Pharm. Bull.* **1989**, *37*, 3105-3107.

(6) Othman, S.; Lirzin, A. L.; Desbois, A. *Biochemistry* **1993**, *32*, 9781-9791.

(7) Wang, J.-S.; Tsai, A.-L.; Heldt, J.; Palmer, G.; Wart, H. E. V. *J. Biol. Chem.* **1992**, *267*, 15310-15318.

(8) Bertini, I.; Turano, P.; Vila, A. J. *Chem. Rev.* **1993**, *93*, 2833-2932.

(9) Bertini, I.; Luchinat, C. *NMR of Paramagnetic Molecules in Biological Systems*; Benjamin/Cummings: Menlo Park, CA, 1986, pp 319.

(10) Smith, M.; McLendon, G. *J. Am. Chem. Soc.* **1981**, *103*, 4912-4921.

(11) Blumenthal, D. C.; Kassner, R. J. *J. Biol. Chem.* **1980**, *255*, 5859-5863.

(12) Rajarathnam, K.; LaMar, G. N.; Chiu, M. L.; Sligar, S. G.; Singh, J. P.; Smith, K. M. *J. Am. Chem. Soc.* **1991**, *113*, 7886-7892.

(13) Goff, H.; Shimomura, E. *J. Am. Chem. Soc.* **1980**, *102*, 31-37.

(14) Wu, J.-z.; La Mar, G. N.; Yu, L. P.; Lee, K.-B.; Walker, F. A.; Chiu, M. L.; Sligar, S. G. *Biochemistry* **1991**, *30*, 2156-2165.

(15) Kimura, K.; Peterson, J.; Wilson, M.; Cookson, D. J.; Williams, R. J. P. *J. Inorg. Biochem.* **1981**, *15*, 11-25.

(16) Satterlee, J. D. *Inorg. Chim. Acta* **1983**, *79*, 195-196.

(17) Bren, K. L.; Gray, H. B.; Banci, L.; Bertini, I.; Turano, P. *J. Am. Chem. Soc.* **1995**, *117*, 8067-8073.

(18) Traylor, T. G.; Berzinis, A. P. *J. Am. Chem. Soc.* **1980**, *102*, 2844-2846.

(19) Moore, G. R.; Pettigrew, G. W. In *Cytochromes c*; Springer Verlag: New York, 1990; pp 174.

(20) Santos, H.; Turner, D. L. *Eur. J. Biochem.* **1992**, *206*, 721-728.

(21) Turner, D. L.; Salgueiro, C. A.; Schenkels, P.; LeGall, J.; Xavier, A. V. *Biochim. Biophys. Acta* **1995**, *1246*, 24-28.

(22) Banci, L.; Bertini, I.; Pierattelli, R.; Vila, A. J. *Inorg. Chem.* **1994**, *33*, 4338-4343.

(23) Timkovich, R. *Inorg. Chem.* **1991**, *30*, 37-42.

(24) Bushnell, G. W.; Louie, G. V.; Brayer, G. D. *J. Mol. Biol.* **1990**, *214*, 585-595.

(25) Emerson, S. D.; Mar, G. N. L. *Biochemistry* **1990**, *29*, 1556-1566.

(26) Turner, D. L.; Williams, R. J. P. *Eur. J. Biochem.* **1993**, *211*, 555-562.

(27) Feng, Y.; Roder, H.; Englander, S. W. *Biochemistry* **1990**, *29*, 3494-3504.

(28) Karplus, M. *J. Chem. Phys.* **1959**, *30*, 11-15.

(29) Feng, Y.; Roder, H.; Englander, S. W.; Wand, A. J.; Stefano, D. L. D. *Biochemistry* **1989**, *28*, 195-203.

(30) Banci, L.; Bertini, I.; Bren, K. L.; Gray, H. B.; Somporrnpisut, P.; Turano, P. *Biochemistry* **1995**, *34*, 11385-11398.

(31) Stuchebrukhov, A. A.; Marcus, R. A. *J. Phys. Chem.* **1995**, *99*, 7581-7590.

(32) Mayo, S. L.; Ellis, W. R.; Crutchley, R. J.; Gray, H. B. *Science* **1986**, *233*, 948-952.

(33) Low, D. W.; Winkler, J. R.; Gray, H. B. *J. Am. Chem. Soc.* **1996**, *118*, 117-120.

(34) Kjaer, M.; Andersen, K. V.; Poulsen, F. M. *Methods Enzymol.* **1994**, *239*, 288-307.

(35) Macura, S.; Ernst, R. R. *Mol. Phys.* **1980**, *41*, 95-117.

(36) Rucker, S. P.; Shaka, A. J. *Mol. Phys.* **1989**, *68*, 509-517.

(37) States, D. H.; Haberkorn, R. A.; Ruben, D. J. *J. Magn. Reson.* **1982**, *68*, 509-517.

(38) Vold, R. L.; Waugh, J. S.; Klein, M. P.; Phelps, D. E. *J. Chem. Phys.* **1968**, *48*, 3831-3832.

(39) Levitt, M. H.; Freeman, R. *J. Magn. Reson.* **1981**, *48*, 65-80.

(40) Marion, D.; Wuthrich, K. *Biochem. Biophys. Res. Commun.* **1983**, *113*, 967-974.

Chapter 4: Photo-initiated Oxidation of Microperoxidase-8, Cytochrome c Peroxidase and Myoglobins. Comparision of Oxidation Chemistries.

Introduction

High-valent iron porphyrins have been implicated in the catalytic cycles of many metalloenzymes, including the peroxidases, catalases, and cytochromes P-450.[1-3] The ability of these enzymes to oxidize a wide variety of substrates with high specificity has generated considerable interest in the chemistry of their high-valent forms[4,5] as well as in the structures and properties of synthetic analogs.[4-10] Peroxidase compounds I and II participate in enzymatic catalysis; compound I contains both a ferryl (Fe(IV)=O) ion as well as an organic radical, derived either from an amino acid residue (cytochrome *c* peroxidase, CcP)[11] or from the porphyrin (horseradish peroxidase, HRP).[12] The properties of CcP compound II, formed by reaction of compound I with single-electron reductants, indicate that it is an equilibrium mixture of Fe(IV)=O and Fe(III) tryptophan-radical species.[11,13] If no readily oxidizable amino acid residues are available, it is possible that a porphyrin radical plays a functional role in compound II; however, in HRP and other heme proteins, the ferric porphyrin radical form of compound II has thus far eluded detection.[14] While compounds I and II have similar one-electron reduction potentials, compound I is much more reactive towards single-electron reductants; electron transfer to the oxidized porphyrin or amino acid of compound I is *ca.* 1000 times more rapid than reduction of the ferryl ion in compound II.[13,14] A similar trend also has been observed in the reverse reaction, in which oxidation of compound II to generate compound I is observed to be more rapid than the oxidation of met-aquo forms to compound II.[15]

We have been exploring the use of photoinduced electron-transfer reactions to generate analogs of high-valent metalloenzyme intermediates in heme enzyme models as well as intact heme proteins. Stepwise oxidation of (P)Fe(III)-OH or (P)Fe(III)-OH_2 (P = porphyrin) to (P)Fe(IV)=O and cationic ($P^{+\bullet}$)Fe(IV)=O generates species whose active oxygen atoms are derived from water instead of peroxides or other active forms of

dioxygen.[16] Our work initially centered on microperoxidase-8 (MP8), the heme-containing octapeptide obtained from proteolytic cleavage of horse heart cytochrome *c*, which has been shown to be a functional peroxidase enzyme model.[19-23] MP8 contains the heme prosthetic group as well as amino acid residues 14-21 of horse heart cytochrome *c*. The imidazole of His18 occupies one of the axial binding sites, leaving the other axial site for exogenous ligands such as water or hydroxide.[17] We have found that the MP8 ferric porphyrin radical is readily prepared by a photoinduced single-electron oxidation in acidic aqueous media. Interestingly, our kinetics data suggest that this ferric porphyrin radical undergoes intramolecular electron transfer to form ferryl MP8 in alkaline solution. We have also extended the work on MP8 to explore the chemistry of heme proteins themselves, and have succeeded in generating high-valent states of horseradish peroxidase (HRP) and cytochrome *c* peroxidase (CcP). The rates at which the three different ferric hemes were oxidized vary greatly, with reactions proceeding to completion in microseconds in MP8 to seconds in the HRP system. Our photoinitiated oxidation technique, however, fails to generate observable oxidized protein products in cytochrome P-450, myoglobin and chloroperoxidase, and possible underlying reasons for the greatly varying observed rates of oxidation will be examined.

Experimental Section

Materials. Ferric MP8 and acetyl MP8 were prepared and purified as described in Chapter 2 of this thesis. Ferryl MP8 for static measurements was prepared chemically by addition of 3% hydrogen peroxide (VWR) to a solution of ferric MP8 in pH 9.5 buffer. Purified MP8 and N-acetyl MP8 were assayed for purity and fully characterized by mass spectrometry and NMR methods.[18] Distilled water was further purified by a Barnstead Nano-Pure system before use. Tris(2,2'-bipyridine)ruthenium(II) chloride (Strem) was

used as received. Hexaammineruthenium(III) chloride (Strem) was recrystallized from warm hydrochloric acid solutions by slowly concentrating a filtered solution in a slowly rotating rotary evaporator. Yeast CcP was a gift from Dr. David Gooden of the Scripps Institute. CcP was stored as a suspension of crystals in deionized water in the freezer in individual sample tubes, and thawed immediately before use. The crystals from thawed samples were dissolved in buffer and the solution centrifuged to remove insoluble materials before use. The concentration of CcP was determined spectrophotometrically using an extinction coefficient of 100 mM^{-1} cm^{-1} at the Soret maximum, 408 nm. Horse-heart myoglobin was obtained from Sigma and used as received. Illumination for steady-state photolysis experiments was provided by an Oriel 75 W halogen photolysis lamp. Deuterated buffer solutions were prepared by repeated rotary evaporation of natural abundance aqueous buffer followed by reconstitution with deuterium oxide (Cambridge Isotopes Laboratories). The pD was then corrected using D_3PO_4 or NaOD as needed, and all reported pD values are corrected for the pH meter isotope effect.

Methods. Absorption spectra were recorded on an HP-8452A spectrophotometer. Flash photolysis measurements were performed on stirred samples contained in sealed quartz cuvettes (NSI precision cuvettes with quartz-glass graded joint) deoxygenated by repeated evacuation followed by backfilling with purified argon from a vacuum line. The excitation source for flash photolysis measurements at 480 nm was a Lambda-Physik FL 3002 dye laser using coumarin 480 dye (Exciton) pumped by a Lambda-Physik LPX 210i XeCl excimer laser (308 nm). Dye laser output was attenuated as needed by passage through crossed polarizing filters. Typically, 1 mJ/pulse laser energies were used. The pulse energy was monitored for consistency by a photodiode and a discriminator. For transient absorption, pulses with energies outside of $\pm$ 10% variance were rejected by disarming the digitizer. For luminescence decay, only pulses lower than 90% of the average intensity were rejected by the discriminator. Probe light for single-wavelength

transient absorption measurements was provided by a 75 watt continuous-wave arc lamp (PTI model A 1010) focused on the aperture of an ISA monochromator fitted with a Hamamatsu 7-stage photomultiplier tube. For time bases $\leq$ 100 μs, increased signal to noise was achieved by increasing the effective probe lamp intensity with the use of a probe lamp pulser synchronized with the laser excitation. For luminescence decay measurements, emitted light was focused onto the monochromator aperture by the optics indicated in Figure 4.1. Time-resolved PMT output was amplified and then processed by a Sony/Tektronix RTD 710 digitizer interfaced to an IBM personal computer. For time bases $\leq$ 1 ms a fast amplifier constructed at Brookhaven National Laboratory was used. For measurements with time bases $\geq$ 1 ms, a slow amplifier (PSD Corp., now defunct) was used. Probe and pump beams were manually made coincident in the sample cuvette by aligning the parallel counter-propagating laser and probe lamp beams, using the optics table shown in Figure 4.1 Kinetics data were evaluated using the least-squares fitting program Kinfit written by Dr. Jay Winkler (PC version) or Dr. T. P. Pascher (Macintosh version).

For multi-wavelength transient absorption measurements, probe light was provided by a flash lamp powered by the discharge of a large capacitor. The time resolution of multi-wavelength measurements was achieved by delaying the probe pulse using a digital delay generator (EG&G). Probe light was passed through a beam-splitter, the reflected portion of the light was directly guided to a spectrograph (Acton Research Corp. SpectraPro 275), while the transmitted portion of the probe light was first passed through the sample before entering the spectrograph. Intensities of probe and reference beams were determined by a dual diode array detector (Princeton Instrument DPDA-1024) interfaced to a PC running either house-written software (Dr. Max Bachrach) or a commercial data collection package (WinSpec). For data collected using the WinSpec package, the diode array was calibrated using the spectrum of an Oriel argon lamp.

Figure 4.1: Schematic of the BILRC nanosecond experiments table used to collect transient absorption and luminescence decay measurements. Probe light from the arc lamp is reflected off of mirrors 1 and 2 through the pinhole and off of mirror 3. Mirror 4 reflects the probe light and focuses it onto the sample. Light transmitted through the sample is reflected off mirror 5 onto mirror 6 and into the aperture of the monochromator. Excitation light from pulsed laser sources passes through an opening in the center of mirror 5 and through the sample. The probe and pump beams are manually aligned to be coincident in the sample.

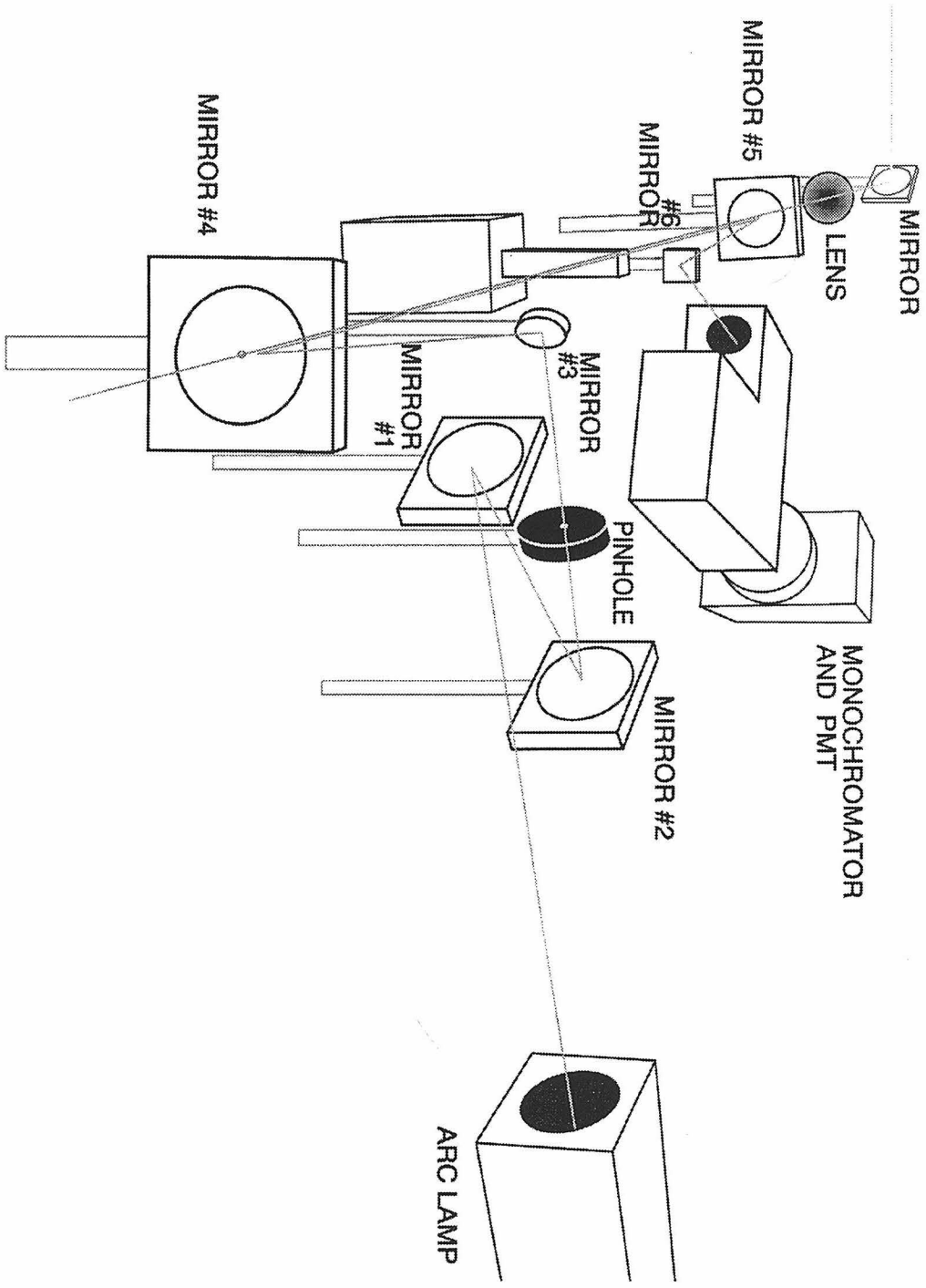
MIRROR
LENS
MIRROR #5
MIRROR #6
MIRROR #4
MIRROR #3
MIRROR #1
PINHOLE
MONOCHROMATOR AND PMT
MIRROR #2
ARC LAMP

Results and Discussion

Flash-Quench Oxidation of MP8

The electronic absorption spectrum of resting MP8 is typical of a high-spin ferric heme (Soret at 396 nm, Q-bands at 510 and 623 nm). Addition of one molar equivalent of hydrogen peroxide to an alkaline solution (> pH 9) of MP8 results in the formation of (P)Fe(IV)=O,[19] whose electronic spectrum features a red-shifted Soret band (406 nm) and absorptions at 519 and 548 nm analogous to those found in the spectra of ferryl myoglobin[16,20,21] and compound II of HRP and CcP.[15] The (P)Fe(IV)=O/(P)Fe(III)-OH MP8 difference spectrum exhibits a large bleach centered at 390 nm and a positive absorption change with a maximum at 413 nm (Figure 4.2).

We have generated (P)Fe(IV)=O by photooxidation of ferric MP8 (Eq. 1abc).

$$Ru(bpy)_3^{2+} \xrightarrow{h\nu} Ru(bpy)_3^{2+*} \quad \textbf{(1a)}$$

$$Ru(bpy)_3^{2+*} + Ru(NH_3)_6^{3+} \longrightarrow Ru(bpy)_3^{3+} + Ru(NH_3)_6^{2+} \textbf{(b)}$$

$$Ru(bpy)_3^{3+} + (P)Fe^{III}\text{-}OH_2 \longrightarrow (P^{\bullet+})Fe^{III}\text{-}OH_2 \,/\, (P)Fe^{IV}{=}O + 2H^+ + Ru(bpy)_3^{2+} \textbf{(c)}$$

Irradiation of $Ru(bpy)_3^{2+}$ in the presence of excess $Ru(NH_3)_6^{3+}$ produces $Ru(bpy)_3^{3+}$ (E° $Ru^{3+/2+}$ = 1.25 V vs. NHE) in less than 1 μs. In the absence of ferric MP8, the photogenerated $Ru(bpy)_3^{3+}$ reacts with $Ru(NH_3)_6^{2+}$ to regenerate the starting complexes on a millisecond time scale (Eq. 1ab).[22] The presence of micromolar ferric MP8 accelerates the decay of $Ru(bpy)_3^{3+}$ and gives rise to absorption changes at 410 and 390 nm that are attributable to the formation of (P)Fe(IV)=O at pH > 6 (Figure 4.3). The

Figure 4.2: A: Absorption spectra of resting Ac-MP8 in pH 10, 0.1 M borate buffer (broken line) and ferryl Ac-MP8 prepared by addition of excess hydrogen peroxide at 0° C (solid line). B: Ferryl-ferric difference spectrum in the Soret region.

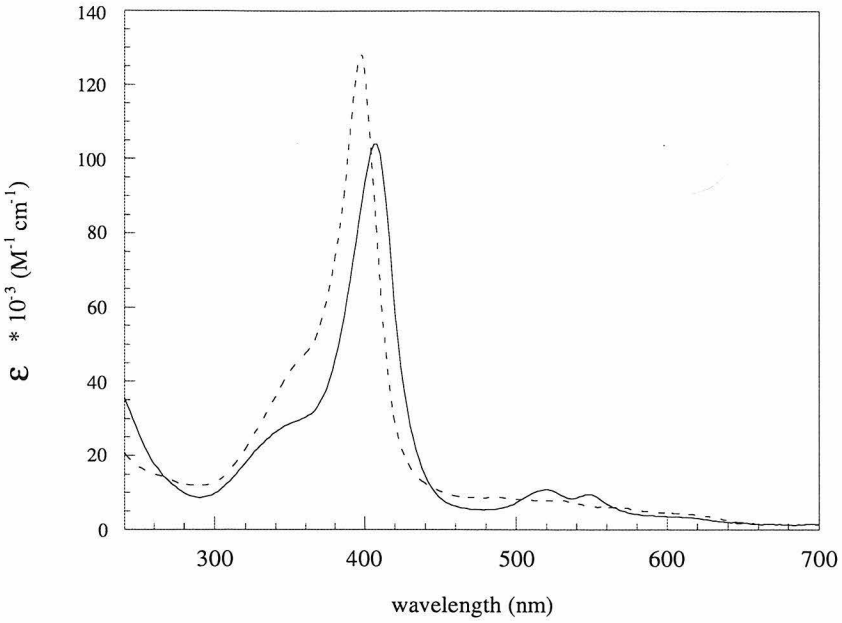
140
120
100
80
60
40
20
0
ε * 10^-3 (M^-1 cm^-1)
300
400
500
600
700
wavelength (nm)

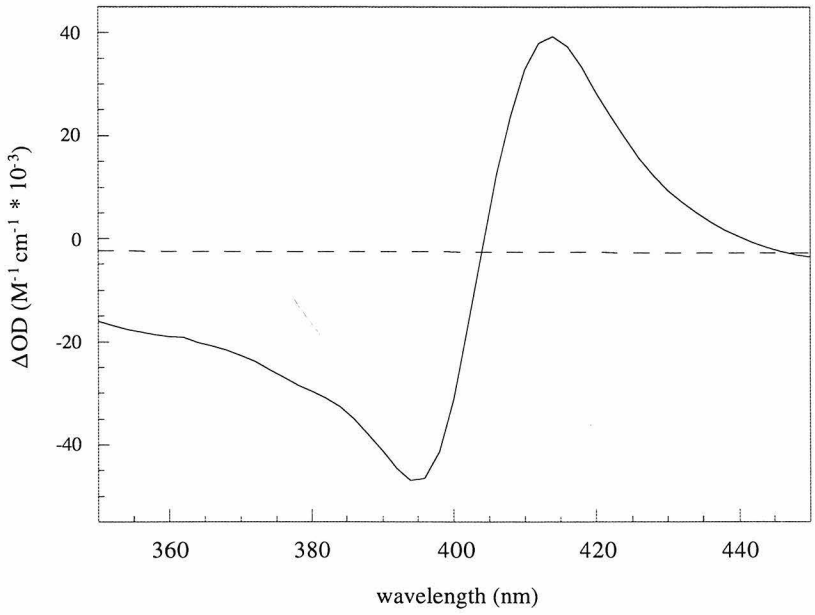
40
20
0
-20
-40
ΔOD (M^-1 cm^-1 * 10^-3)
360
380
400
420
440
wavelength (nm)

Figure 4.3: Single-wavelength transient absorption spectra in the (P)Fe(III) (390 nm) and (P)Fe(IV) (410 nm) Soret regions obtained after flash photolysis of a 7 μM solution of resting MP8 with 5 mM $Ru(bpy)_3^{2+}$ and 10 mM $Ru(NH_3)_6^{3+}$ in 0.1 M phosphate buffer (pH 8).

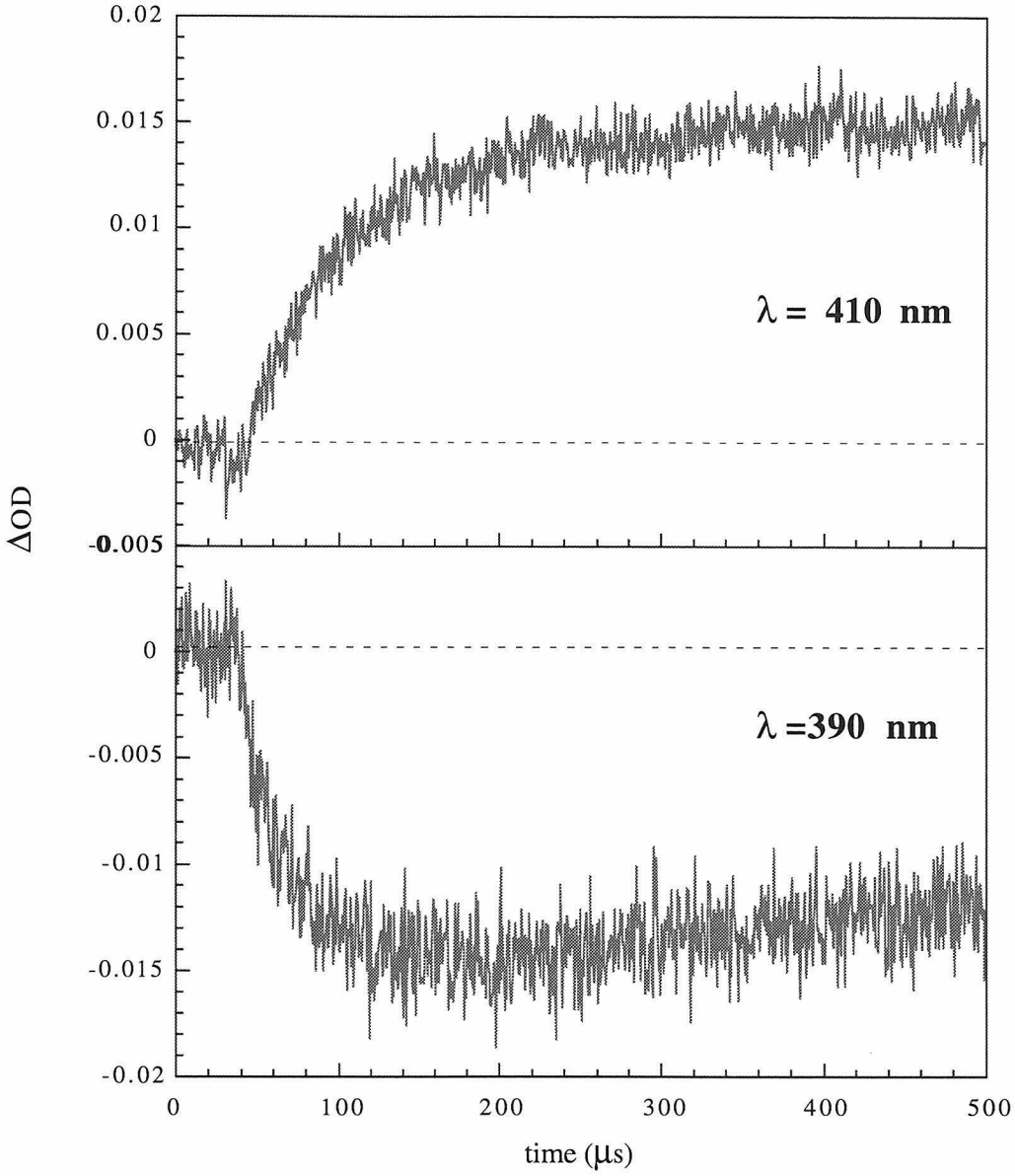
0.02
0.015
0.01
0.005
0
-0.005
λ = 410 nm
0
-0.005
-0.01
-0.015
-0.02
λ =390 nm
ΔOD
0
100
200
300
400
500
time (μs)

ferryl/ferric difference spectrum strongly resembles the transient absorption spectrum obtained 300 μs after laser irradiation (Figure 4.4c). Ferryl MP8 features a well-defined Q-band doublet with maxima at 521 and 548 nm. The transient absorption spectrum at pH 8 exhibits similar features at 524 and 552 nm, consistent with transient generation of (P)Fe(IV)=O (Figure 4.5). Under these conditions, the ferryl species persists for several milliseconds. The quencher is absolutely necessary for electron transfer to occur; irradiation of a solution containing only $Ru(bpy)_3^{2+}$ and MP8 does not result in any detectable quenching of the $Ru(bpy)_3^{2+}$ excited state (the luminescence lifetime of $Ru(bpy)_3^{2+}$ with micromolar MP8 in buffered solution is indistinguishable from a control sample containing only $Ru(bpy)_3^{2+}$). Thus, direct quenching of the excited state by MP8 is negligible, and electron transfer to $Ru(NH3)_6^{3+}$ is the only quenching pathway that will be considered here.

The oxidation of ferric MP8 by $Ru(bpy)_3^{3+}$ exhibits pseudo-first-order kinetic behavior. A plot of the observed rate constant *vs*. the concentration of ferric MP8 is linear over a wide concentration range (5 to 100 μM), and the slope yields a second-order rate constant of 2.2×10^9 M^{-1} s^{-1} at pH 8 (Figure 5). The rate of appearance of (P)Fe(IV)=O after laser photolysis is essentially pH independent over the pH 7-9 range (pH 7, 2.7×10^9 M^{-1} s^{-1}; pH 7.5, 2.2×10^9 M^{-1} s^{-1}; pH 8.5, 2.0×10^9 M^{-1} s^{-1}). The rate of ferryl generation exhibits a small solvent isotope effect, $k_H/k_D = 1.7$, consistent with the presence of a hydroxide or aquo ligand on ferric MP8 that is deprotonated to the oxo ligand of ferryl MP8. In principle, the number of protons involved in the rate-determining step may be determined by examining the rate of reactions in a series of solutions containing a range of isotopic compositions (the "proton inventory" method). The rates at which Fe(IV)=O species appear follow a roughly linear dependence on the deuterium oxide content of the solvent; however, due to the small magnitude of the isotope effect, the results of proton

Figure 4.4: Soret-region transient absorption spectra taken 300 μs after laser photolysis at pH 6, 6.5, and 7. Each sample contains 7 μM MP8, 10 μM $Ru(bpy)_3^{2+}$ and 10 mM $Ru(NH_3)_6^{3+}$ in 0.1 M phosphate buffer.

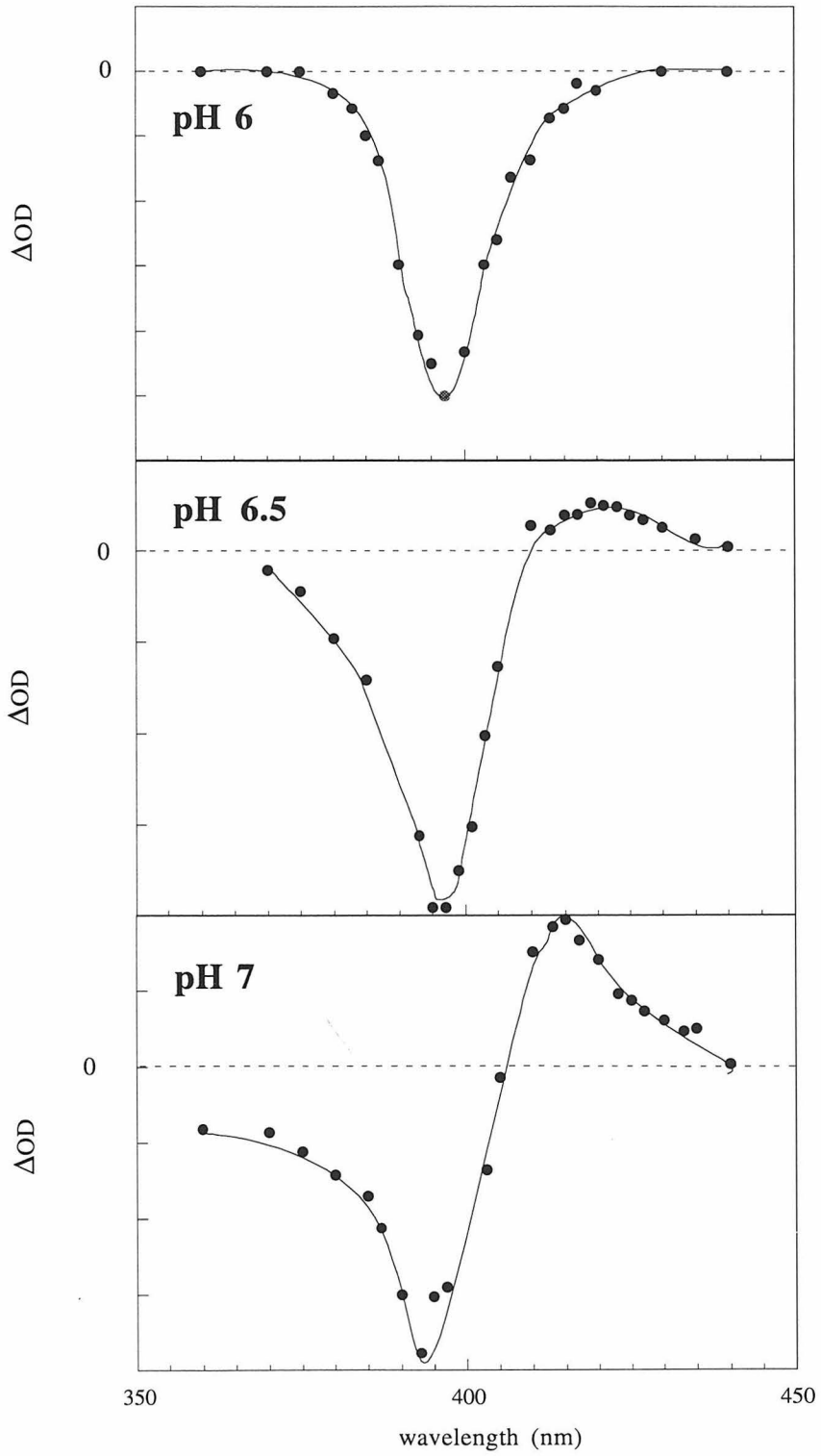
pH 6
pH 6.5
pH 7
0
0
0
ΔOD
ΔOD
ΔOD
350
400
450
wavelength (nm)

Figure 4.5: A: Ferryl-ferric difference spectrum in the Q-band region. Ferryl MP8 was generated by addition of hydrogen peroxide to a solution of ferric Ac-MP8 in pH 9.5 borate buffer at 0° C. B (C): Q-band region transient absorption spectrum obtained 300 μs after laser irradiation of solutions containing 30 mM MP8, 20 mM $Ru(bpy)_3^{2+}$, 10 mM $Ru(NH_3)_6^{3+}$ in 0.1 M phosphate buffer, pH 8 and (pH 6).

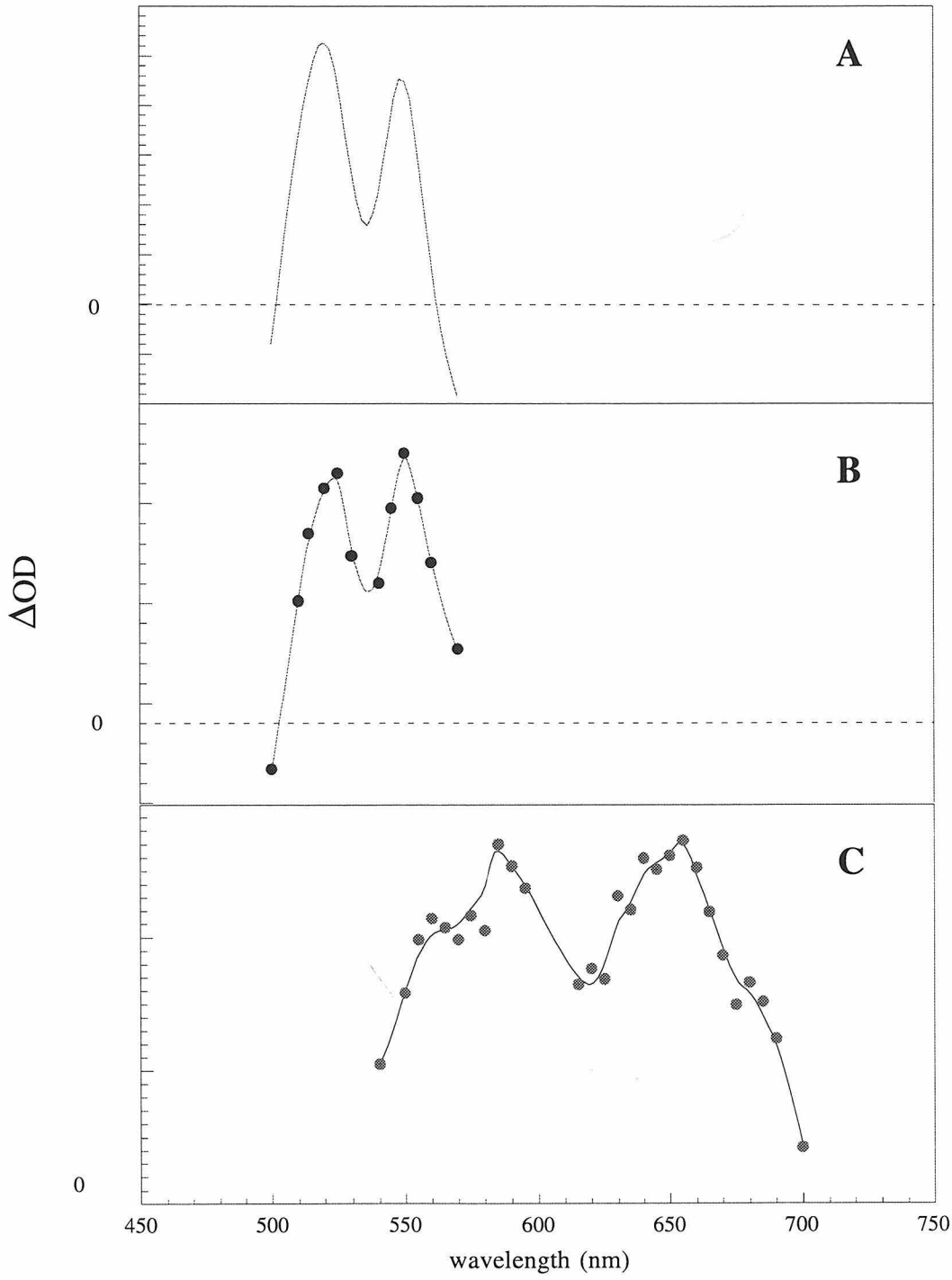
A
B
C
0
0
0
ΔOD
450
500
550
600
650
700
750
wavelength (nm)

inventory experiments were inconclusive as to whether a single proton or multiple proton transfers were involved in the rate determining step.

Oxidation of (P)Fe(III)-OH_2 by $Ru(bpy)_3^{3+}$ in solutions below pH 6 does not result in transient generation of ferryl MP8, and flash photolysis measurements are consistent with the production of the ferric cation-radical porphyrin. The transient absorption spectrum taken 300 μs after laser photolysis of a pH 6 solution (Figure 4.4a) shows a Soret-region bleach whose minimum coincides with the ferric Soret band maximum (396 nm). No OD increase is observed in the Soret region, indicating the production of a porphyrin species with a weaker Soret band. Electrochemical oxidation of Fe(III)(TPP)-Cl gives $[Fe(III)(TPP)\text{-}Cl]^{+\bullet}$, whose absorption spectrum features a broadened Soret band with a lower extinction coefficient than that of the neutral Fe(III) species.[23] An examination of the transient absorption spectrum in the visible region reveals broad absorptions at 587 and 650 nm (Figure 4.5). The absorption spectra of cation-radical porphyrins typically exhibit broadened, red-shifted Q-bands.[23] No solvent isotope effect was observed on the rate of oxidation and an apparent second-order rate constant of $5.6 \times 10^9\ M^{-1}\ s^{-1}$ was obtained from a concentration dependence study (Figure 4.6). Ferric deuteroporphyrin dimethyl ester (Fe(III)(DPDE)) reacts rapidly with radiolytically generated peroxyl radicals in mixed organic-aqueous solvents to give $Fe(III)(DPDE)^{+\bullet}$ ($k \sim 2.6 \times 10^8\ M^{-1}\ s^{-1}$).[24-26] Peroxyl radicals have reduction potentials in the 1.0-1.1 V range, similar to that of $Ru(bpy)_3^{3+}$.[27]

It is apparent that oxidation of ferric MP8 at low pH results in exclusive formation of the porphyrin cation-radical product (Eq. 2a). At low pH, equilibrium 2b lies to the left; deprotonation of the radical aquo ligand is not favored, and the radical species is effectively trapped.

Figure 4.6: Rates of oxidation of ferric MP8 to ($P^{\bullet+}$)Fe(III)-OH_2 (pH 6) and (P)Fe(IV)=O (pH 8) as a function of [Fe(III)]: [$Ru(bpy)_3^{2+}$], 10 μM; [$Ru(NH_3)_6^{3+}$], 10 mM.

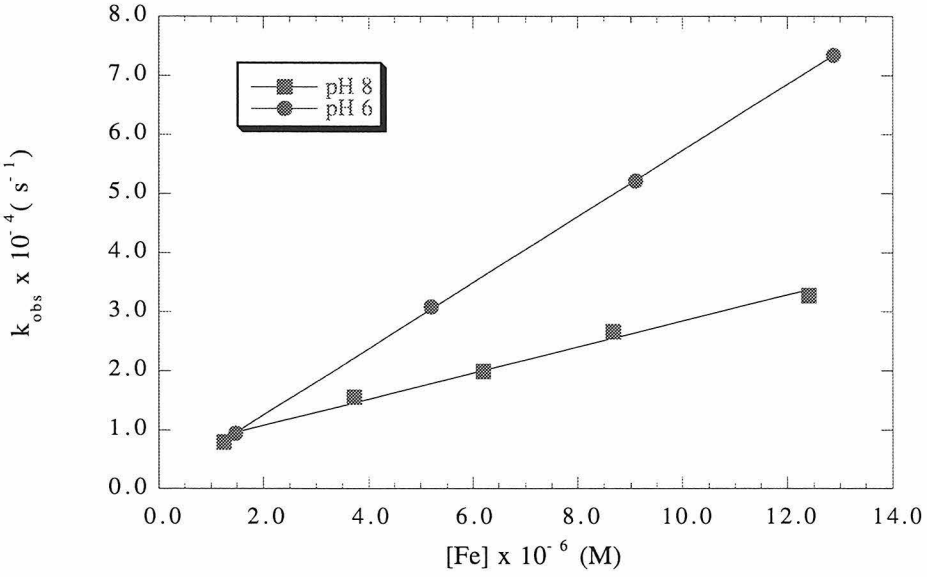
8.0
7.0
6.0
5.0
4.0
3.0
2.0
1.0
0.0
pH 8
pH 6
k_{obs} x 10^{-4} (s^{-1})
0.0
2.0
4.0
6.0
8.0
10.0
12.0
14.0
[Fe] x 10^{-6} (M)

$$Ru(bpy)_3^{3+} + (P)Fe^{III}\text{-}OH_2 \underset{k_{-1}}{\overset{k_1}{\rightleftharpoons}} Ru(bpy)_3^{2+} + (P^{\bullet+})Fe^{III}\text{-}OH_2 \qquad \textbf{(2a)}$$

$$(P^{\bullet+})Fe^{III}\text{-}OH_2 \underset{k_{-2}}{\overset{k_2}{\rightleftharpoons}} (P)Fe^{IV}{=}O + 2\,H^+ \qquad \textbf{(2b)}$$

$$Ru(bpy)_3^{3+} + (P)Fe^{III}\text{-}OH_2 \underset{k_{-3}}{\overset{k_3}{\rightleftharpoons}} Ru(bpy)_3^{2+} + (P)Fe^{IV}{=}O + 2\,H^+ \qquad \textbf{(2c)}$$

At alkaline pH, initial oxidation of the porphyrin is followed by rapid conversion to the ferryl product; the buildup of radical species is no longer observed. Oxidation of the porphyrin is not a proton-coupled redox process, and therefore its associated rate constants (k_1 and k_{-1}) are predicted to be insensitive to solution pH and isotopic composition, in line with the experimental findings. The single-electron oxidation of chromium(III) porphyrins to the corresponding chromium(IV)-oxo porphyrins proceeds through an analogous chromium(III) cation-radical porphyrin intermediate whose optical spectrum has been observed by pulse radiolytic methods.[30]

Transient absorption spectra taken 300 μs after excitation exhibit a gradual growth of the 420 nm Fe(IV)=O absorption relative to the 396 nm bleach as the pH increases from 6 to 8.5 (Figure 4.5abc). We interpret this as a pH-dependent shift of the equilibrium between the two redox forms of oxidized MP8 (Eq. 2b). It has been shown that electrochemically generated $[Fe(III)(TMP)(ClO_4)]^{+\bullet}$ undergoes a similar transformation to a ferryl species upon metathesis of the perchlorate ligand to hydroxide.[28] The position of the transition between the ferric radical and the ferryl porphyrin as the observed product appears to be near pH 6. The transition between aquo and hydroxo ligands on the MP8 iron does not occur until near pH 9;[17,29] however, the lower pK value may reflect that the species being deprotonated in the case of the flash-quench oxidation is the ferric radical

aquo or hydroxo species, and the increased positive charge on the heme is likely to cause an increase in the acidity of the axial aquo or hydroxo ligands. Coincidentally, the transition between ferric W191 radical and ferryl forms of CcP appears to also occur near pH 6 (*vide infra*).[30]

The rate law for the mechanism described by Eq. 2 (with pseudo-first-order conditions for (P)Fe(III)-OH_2 and $Ru(bpy)_3^{2+}$) predicts biexponential kinetics of ferryl MP8 formation. The direct conversion of a ferric aquo or hydroxo complex to a ferryl species involves coupled proton and electron transfers, and, whether the processes are concerted or sequential, the observed rate should be strongly dependent on pH and solvent isotope (H/D) composition. The observed ferryl MP8 formation rates are only weakly dependent on these two factors indicating that neither Eq. 2b nor Eq. 2c is important in the rate-determining step of the reaction. If we assume that Eq. 2c does not contribute to the observed reaction (i.e., $k_3[(P)Fe(III)\text{-}OH_2] + k_{-3}[Ru(bpy)_3^{2+}] << k_1[(P)Fe(III)\text{-}OH_2] + k_{-1}[Ru(bpy)_3^{2+}]$), then the two rate constants in the biexponential formation of ferryl MP8 are given by Eq. 3.

$$\nu_1 = k_1\,[Fe^{III}MP8] \; + \; \frac{k_{-1}\,[Ru(bpy)_3^{2+}]\,k_{-2}}{k_2 + k_{-2}} \qquad \textbf{(3a)}$$

$$\nu_2 \; = \; k_2 + k_{-2} \qquad \textbf{(3b)}$$

The intramolecular equilibration between ferryl MP8 and the ferric porphyrin radical (Eq. 2c), although intrinsically slow, is still likely to be faster that the bimolecular oxidation of ferric MP8 by $Ru(bpy)_3^{3+}$ (i.e., $k_2 + k_{-2} >> k_1[(P)Fe(III)\text{-}OH_2] + k_{-1}[Ru(bpy)_3^{2+}]$. Hence, the amplitude of the exponential corresponding to ν_2 will be negligible and the overall reaction will appear to be a single-exponential process. The expression for ν_1 correctly predicts the linear dependence on the total MP8 concentration, the observed

nonzero intercept, as well as the weak dependence on pH and H/D composition of the solvent.

Our findings strongly indicate that ligand-centered oxidation of both hydroxo and aquo MP8 is the rate-limiting step in the formation of (P)Fe(IV)=O. Although ferric porphyrins generally have ligand-centered reduction potentials somewhat higher than their metal-centered potentials,[31,32] the porphyrin is oxidized more rapidly by $Ru(bpy)_3^{3+}$ than the ferric center. The difference in electron-transfer rates is attributable to the proton-coupled oxidation of the ferric center to a ferryl species. It is likely that the large reorganization energy for concerted Fe(III)/Fe(IV)=O interconversions makes stepwise mechanisms more favorable and may account for the sluggish reactivity of compound II ferryl compounds.[33] Our data suggest that (P)Fe(IV)=O is not a kinetically competent oxidant and that its reactions are governed by a slow interconversion between the metal-oxo form and the highly reactive ferric radical species.

Flash-Quench Oxidation of CcP

As discussed previously, yeast CcP reacts with hydrogen peroxide to produce water and the 2 electron oxidized cmp I form of the protein, which contains a ferryl porphyrin and an oxidized W191 side chain. It has been suggested that formation of cmp I proceeds through the intermediacy of an HRP cmp I - like species that contains both a ferryl porphyrin and a porphyrin cation radical.[34] The cmp II oxidation state of CcP is thought to be an equilibrium between W191 radical - ferric porphyrin and neutral W191 - ferryl porphyrin species; however, the possible presence of a ferric porphyrin radical similar to that observed in the flash-quench oxidation of MP8 has not been reported. We therefore began to investigate the single-electron oxidation of CcP in order to investigate this chemistry.

Treatment of CcP with excess hydrogen peroxide results in immediate oxidation of the protein to the cmp I level. The optical spectrum of CcP cmp I strongly resembles that of neutral ferryl porphyrins such as HRP cmp II and MP8 cmp II, with a Soret band redshifted from that of the ferric resting state (Figure 4.7). The W191 radical has only very weak absorptions in the visible and its contributions to the spectrum are considered negligible here, thus the optical spectra of CcP cmp I and cmp II both are dominated by the spectrum of the ferryl porphyrin center and are identical for our purposes. The difference spectrum obtained from manual subtraction of the ferryl and ferric CcP spectra is qualitatively similar to the ferryl - ferric MP8 difference spectrum with a ΔOD minimum in the ferric Soret region at 385 nm and ΔOD maximum in the ferryl Soret region at 425 nm (Figure 4.7).

Multi-wavelength transient absorption spectra were taken at pH 6 and 8, and were found to be in excellent agreement with the transient absorption profile obtained from single-wavelength measurements. These transient absorption spectra are qualitatively similar to the static difference spectrum; however, both the minimum and maximum are shifted by approximately 5 nm to the blue (Figure 4.8). While this difference may indicate the formation of a product other than ferryl CcP, the rate of $Ru(bpy)_3^{3+}$ decay appears to be identical to the rate at which the new spectrum grows in (Figure 4.9), establishing that the new spectrum corresponds to an oxidized protein product. The shifted spectrum may indicate that either the solvation of the heme in CcP oxidized by an outer-sphere oxidant may be different from that resulting from oxidation by hydrogen peroxide, or that the protonation state of groups near the heme may be different. Oxidation by peroxide appears to result in the extrusion of two of three crystallographic water molecules present in the ferric active site pocket, one directly displaced by the incoming peroxide molecule.[35]

Figure 4.7: Top: Static UV-vis spectra of CcP, resting (dashed) and treated with an excess of hydrogen peroxide (solid). Bottom: Soret region difference spectrum calculated by manually subtracting the ferryl and ferric static spectra.

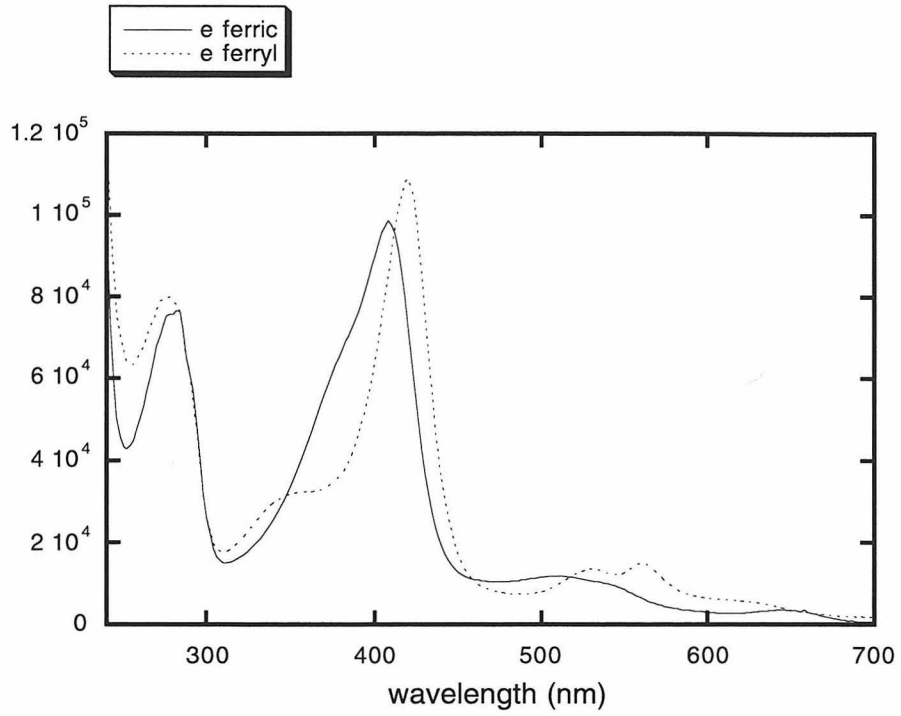
e ferric
e ferryl
1.2 10^5
1 10^5
8 10^4
6 10^4
4 10^4
2 10^4
0
300
400
500
600
700
wavelength (nm)

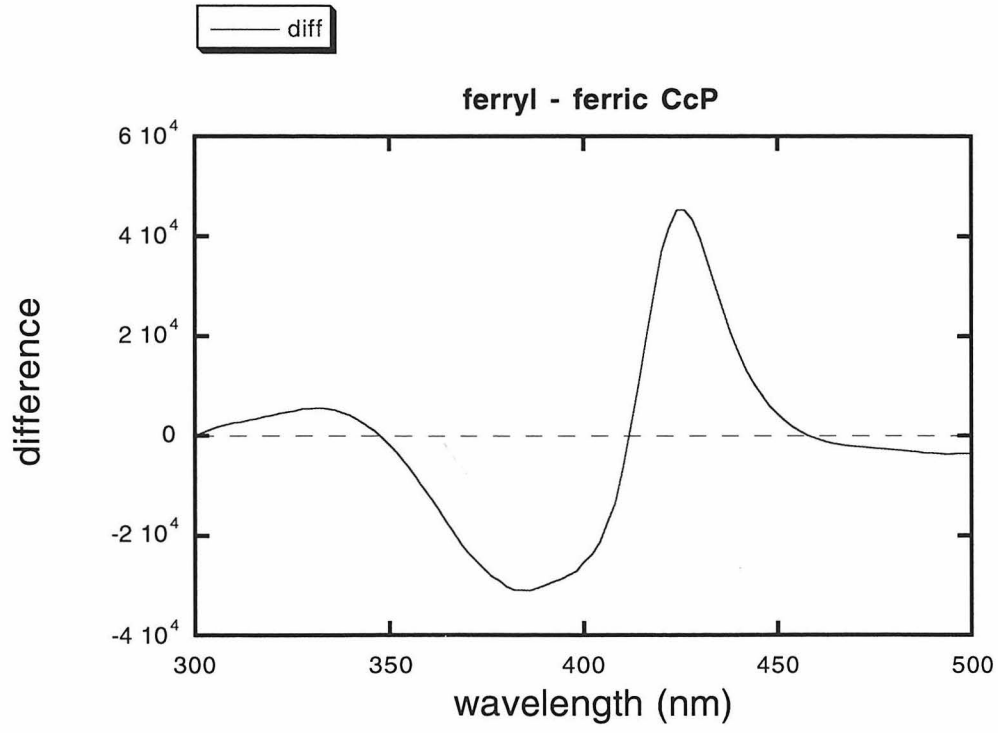
diff
ferryl - ferric CcP
difference
6 10^4
4 10^4
2 10^4
0
-2 10^4
-4 10^4
300
350
400
450
500
wavelength (nm)

Figure 4.8: Top: Transient absorbance spectrum of oxidized CcP intermediate resulting from reaction with photo-generated $Ru(bpy)_3^{3+}$. Conditions: pH 6 0.1 M phosphate buffer, laser excitation at 480 nm, 1 Hz repetition rate. 7 mM CcP, 10 μM $Ru(bpy)_3^{2+}$, 10 mM $Ru(NH_3)_6^{3+}$. The spectrum was generated by plotting the ΔOD measurements and measuring the ΔOD at t = 5 ms at each wavelength. Bottom: Direct comparison of the difference spectrum obtained from static UV-vis measurements (dotted) with the transient difference spectrum obtained 5 ms after laser excitation (solid).

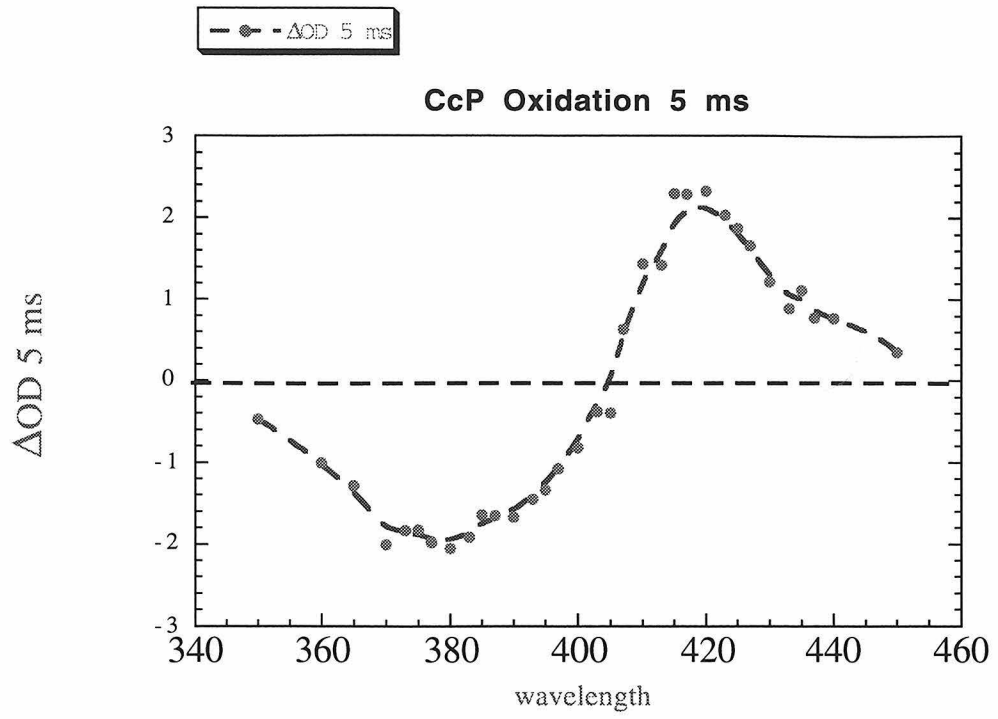
ΔOD 5 ms
CcP Oxidation 5 ms
ΔOD 5 ms
3
2
1
0
-1
-2
-3
340
360
380
400
420
440
460
wavelength

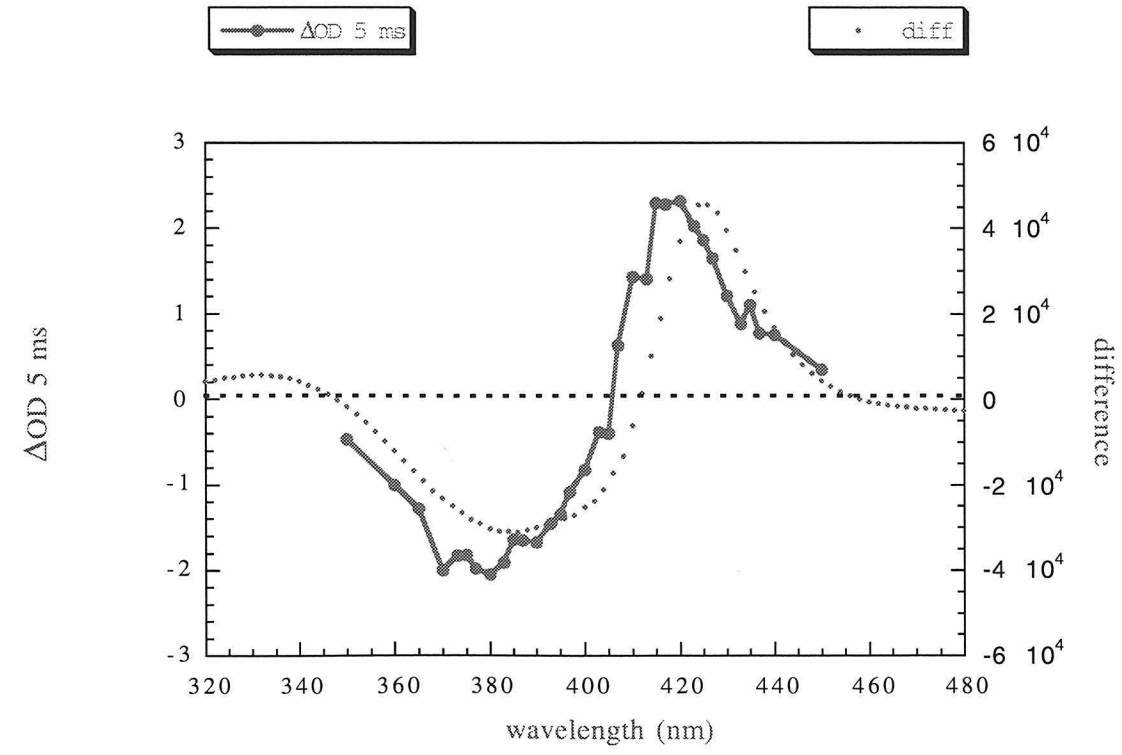
ΔOD 5 ms
diff
ΔOD 5 ms
3
2
1
0
-1
-2
-3
6 10^4
4 10^4
2 10^4
0
-2 10^4
-4 10^4
-6 10^4
difference
320
340
360
380
400
420
440
460
480
wavelength (nm)

Figure 4.9: Direct comparison between kinetics observed for the appearance of CcP Fe(IV)=O (light dots) and the decay of $Ru(bpy)_3^{3+}$ (heavy solid trace) transient absorption spectra.

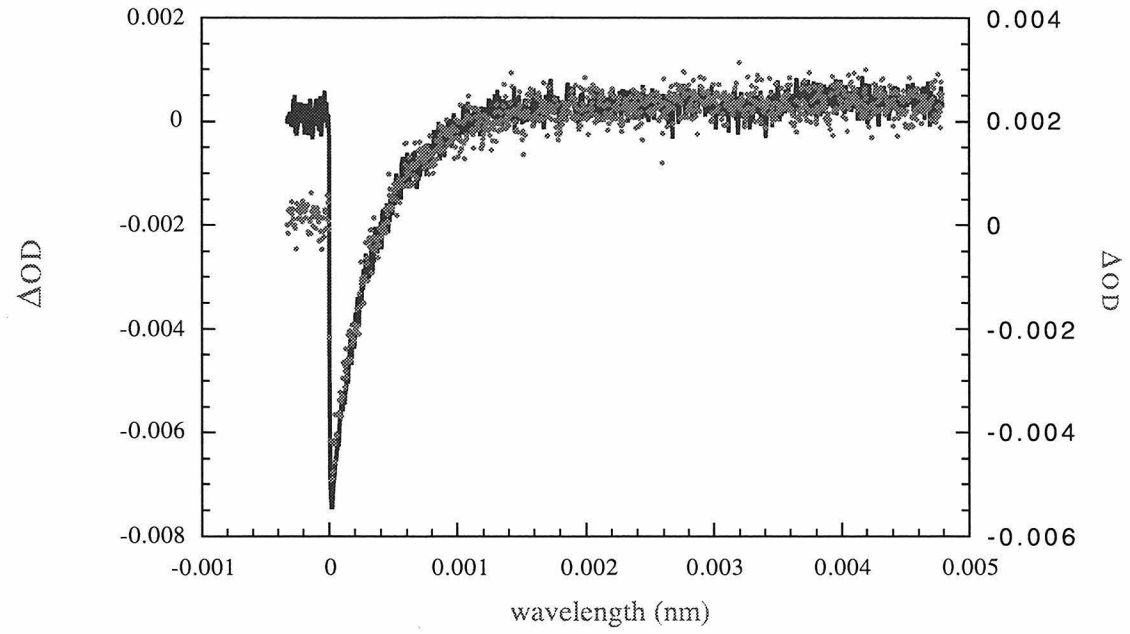
0.002
0
-0.002
-0.004
-0.006
-0.008
ΔOD
0.004
0.002
0
-0.002
-0.004
-0.006
ΔOD
-0.001
0
0.001
0.002
0.003
0.004
0.005
wavelength (nm)

Outer-sphere oxidation by $Ru(bpy)_3^{3+}$, however, requires no incoming group and therefore places no steric demands on the heme pocket that may result in water extrusion, and the increased pocket polarity may account for the slight blue shift in the transient spectra. Alternatively, the number of protons generated by the reaction with peroxide is different from that resulting from outer-sphere oxidation. Oxidation with peroxide requires that two protons be removed from the peroxide molecule to yield the ferryl oxo ligand and a molecule of water. In the flash-quench oxidation, again, two protons are must be removed from the active site. However, the second oxygen from the peroxide is not present to act as a proton acceptor, so the protonation state of nearby basic residues such as H52 and R48 may be different. The possibility also exists that protonation of R48 may alter the hydrogen bonding interaction with the ferryl oxygen resulting in a shift in the spectrum. The oxo ligand itself may also be protonated, although the terminal iron oxo species is likely to be highly acidic.

No intermediates were observed as in the flash-quench oxidation of HRP,[36] nor could the presence of an intermediate be inferred from the kinetics as in the case of MP8 oxidations.[37] The rate of appearance of the ferryl spectrum at pH 6 was found to be 2700 s^{-1} with a CcP concentration of 7 μM and a pulse energy of approximately 1 mJ. The amplitudes of the transient absorption signals, however, are relatively small compared to spectra of MP8 under comparable conditions. The concentration of $Ru(bpy)_3^{3+}$ generated by laser photolysis was calculated from a transient absorption trace at 450 taken on a 10 μs time scale. The trace levels after an initial rapid bleach and recovery that corresponds to generation of the excited state and rapid quenching to yield $Ru(bpy)_3^{3+}$. The molar extinction ΔOD at 450 calculated from static $Ru(bpy)_3^{2+}$ and $Ru(bpy)_3^{3+}$ spectra was taken to be - 13, 400 M^{-1} cm^{-1}. The ΔOD at 450 was obtained by fitting the kinetic trace to a single exponential, and an offset at infinite time of - 3.9 mOD was obtained, corresponding

to an initial $Ru(bpy)_3^{3+}$ concentration of 0.29 μM. Assuming that all of the oxidizing equivalents generated were consumed in oxidation of the protein, a ΔOD of 13.2 mOD at the difference Soret maximum is predicted if all of the oxidizing equivalents produced a ferryl porphyrin. CcP cmp II, however, is known to exist as an equilibrium mixture with oxidizing equivalents on both the iron and on W191.[30] The amplitudes observed for flash-quench oxidations of CcP at pH 6 are significantly smaller than those predicted; only 20% of the oxidizing equivalents are spectroscopically detected as ferryl species, implying that the remaining 80% are present as the W191 radical species. The value for the equilibrium constant between W191 radical and ferryl forms of CcP cmp II at pH 6 is reported to be approximately 5, with the ferryl species predominating. Clearly the results of the flash-quench oxidation differ on this matter; however, the possibility exists that the extinction coefficient of the oxidized protein product observed from flash-quench oxidation may be significantly altered compared to that of the chemically generated ferryl CcP. We also cannot exclude the possibility that the equilibrium between ferryl and W191 radical species has been significantly altered by changes in heme solvation and/or hydrogen bonding. Lowered yields of ferryl and therefore increased amounts of W191 radical are consistent with a destabilization of the ferryl species that may be the result of the removal of the hydrogen bonding between R48 and the ferryl oxygen. The fact that presence of the W191 radical is inferred from the magnitudes of the transient absorption spectra, yet the kinetics of $Ru(bpy)_3^{3+}$ decay and Fe(IV)=O growth are identical and fit well to monoexponential kinetics, implies that the equilibration between the two species is rapid compared to the bimolecular oxidation reaction itself. In spite of the fact that W191 and the heme are in close contact, and that the radical and heme are magnetically coupled as evidenced by the EPR spectrum, the observed rates of equilibration between ferric radical and ferryl forms of CcP are anomalously slow, $< 1000\ s^{-1}$ in the pH 5 - 7 range.[30] The slow rate of

equilibration was attributed to large reorganization energies due to the proton requirement for reduction of the ferryl ion by the W191 radical. Since our pseudo-first order rate constants are at most only a factor of two greater than the reported rates of radical-ferryl equilibration, we would expect to see markedly biphasic kinetics. We propose here that the ferryl CcP species generated by single-electron oxidation interacts strongly with a proton left in the active site pocket as a result of single electron oxidation. While terminal Fe(IV) oxo species are likely to be strongly acidic, there may be additional hydrogen bonding contributions from, for instance, a protonated H52. A protonated ferryl species may undergo more facile reduction by W191 due to a reduction in the reorganization energy of the reaction (contributions from nuclear rearrangements due to protonation increases the total reorganization energy for reduction of the unprotonated ferryl), speeding the rate at which equilibrium is attained.

Photo-induced Oxidation of Myoglobins

Although the physiological role of myoglobin (Mb) is to reversibly store and release molecular oxygen, exposure to hydrogen peroxide generates the well-known ferryl form of Mb, that has been shown to contain an Fe(IV)=O chromophore. The second oxidation equivalent from the reduction of hydrogen peroxide is translocated as a radical on tyrosine side-chains to the surface of the protein where it is available for oxidation chemistry.[38] Strong outer-sphere single electron oxidants, such as hexachloroiridate(IV), have also been shown to oxidize met-Mb to ferryl Mb.[39] We therefore reasoned that photo-generated $Ru(bpy)_3^{3+}$ should also react to oxidize the heme and yield ferryl Mb; however, attempts to observe flash-quench oxidation of Mb by transient absorption were fruitless (T. B. Karpishin, unpublished results). Moreover, steady state photo-oxidation of wild-type equine Mb using $Ru(bpy)_3^{3+}$ and the irreversible quencher $Co(NH_3)_5Cl$ also only resulted

in irreversible heme degradation. It may, however, be possible to oxidize the Mb heme with photo-initiated oxidants that are covalently tethered to the heme itself (P. Farmer, unpublished results).

The redox properties of Mb's are clearly different from those of peroxidases and P-450 type enzymes, which have strongly donating axial ligands present that are capable of stabilizing highly oxidized hemes (recall from Chapter 1 that peroxidases have a strongly hydrogen-bonded axial imidazole that results in a shorter Fe-N bond). Mb mutants exist, however, in which the nature of the axial ligand is readily altered. Mutation of the axial H93 ligand of sperm whale Mb (SW Mb) to a G results in a "cavity mutant" that is readily reconstituted with various exogenous ligands.[40,41] Addition of ethanethiol to met-H93G SWMb results in thiol binding to the heme iron, giving a species whose optical spectrum strongly resembles that of ferric cytochrome P-450's. Since the highly oxidized intermediates in cytochrome P-450 catalysis remain elusive and few suitable well-characterized models exist for these species, the oxidation chemistry of thiol-reconstituted H93G SWMb (EtSH H93G SWMb) was explored.

Steady-state illumination of a solution containing EtSH H93G SWMb with $Ru(bpy)_3^{2+}$ at room temperature results in irreversible heme degradation similar to that seen with wild type Mb's. However, photolysis at lower temperatures (4° C), results in clean changes in the optical spectrum, from that of the ferric thiol form to a species with a Soret band at 420 nm (Figure 4.10). This species is stable for hours at 4° C, and is not affected by the addition of mild reductants such as ascorbic acid. The optical spectrum obtained after ~ 5 minutes of photolysis does not resemble that of chloroperoxidase cmp II, one of the few characterized thiolate-bound oxidized hemes.[42] A species with a Soret band at 420 is also obtained upon oxidation of EtSH H93G SWMb with H_2O_2 (J. Dawson, pers. comun.). The identity of this species remains unknown; however, it does not exhibit the reactivity and spectroscopic properties of an Fe(IV)=O heme, or a porphyrin

Figure 4.10: Steady-state photolysis of the EtSH form of H93G SWMb. 1 mM $Co(NH_3)_6^{3+}$, 20 μM $Ru(bpy)_3^{2+}$. Spectra were taken every 30 seconds. Three different phases of the reaction were observed. Top: Decay of the initial EtSH H93G SWMb spectrum and growth of species with 406 nm Soret. Middle: Decay of the 406 nm Soret species. Bottom: Partial recovery of the bleached spectrum.

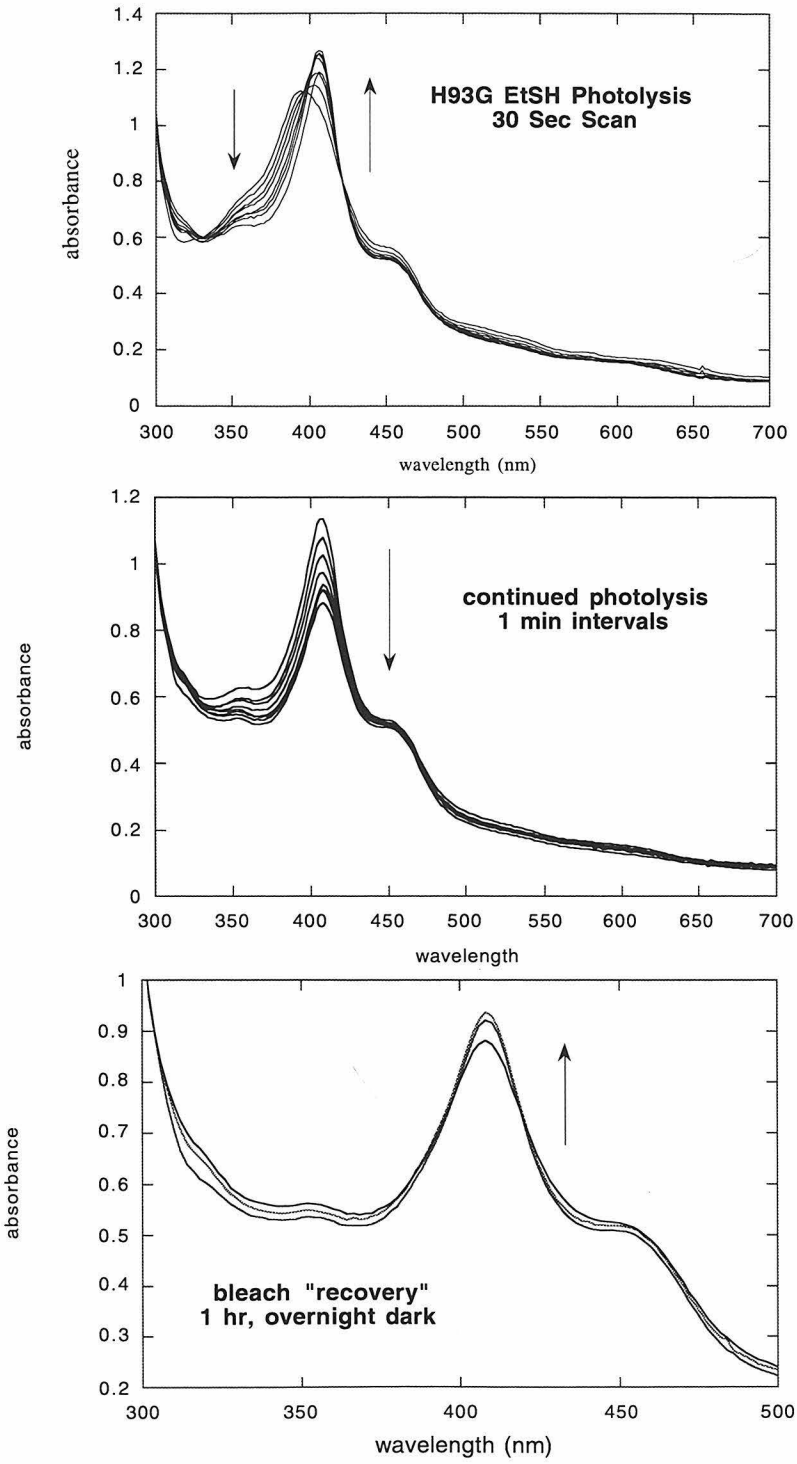
H93G EtSH Photolysis
30 Sec Scan
absorbance
wavelength (nm)
continued photolysis
1 min intervals
absorbance
wavelength
bleach "recovery"
1 hr, overnight dark
absorbance
wavelength (nm)

radical: it is possible that it is the product of oxidative damage to the thiol ligand. Time-resolved measurements of this oxidation reaction may reveal the presence of intermediates or an alternative initial oxidation product, and should be investigated.

Comparisons of Results from Oxidation of Proteins and Models

Clearly, the oxidations of MP8 proceed rapidly, with high efficiency; roughly 66% of the oxidizing equivalents initially generated by photolysis and quenching are accounted for by ferryl MP8 absorption at pH 7. The bimolecular rate for oxidation of MP8 is also by far the most rapid over all pH conditions, nearly 3 orders of magnitude faster than the initial oxidation of the HRP porphyrin radical, and an order of magnitude greater than the estimated bimolecular rate for oxidation of CcP by $Ru(bpy)_3^{3+}$ (MP8 is oxidized by $Ru(bpy)_3^{3+}$ at ca. 2×10^9 M^{-1} s^{-1}, while the HRP ferric radical is formed at 10^6 M^{-1} s^{-1}). The six-coordinate nature of the MP8 and CcP active sites ensures that an axial water is bound to the iron atom when oxidation takes place, while in HRP, water binding to the five-coordinate heme is reported to be slow and determines the rate of appearance of the Fe(IV)=O form of the protein. Oxidation of the MP8 heme is clearly favored over the CcP and HRP hemes due to its large solvent exposure. Both HRP and CcP have only their heme edges exposed to solvents; however, each is much more protected from solvent than MP8's heme. Heme exposure clearly is not the only factor governing the reactivity towards outer-sphere oxidants, as Mb has a high degree of heme exposure, but does not readily participate in outer-sphere oxidations. A number of explanations for the lack of reactivity with Mb are conceivable. The higher reduction potentials for redox chemistry of Mb cannot be ruled out as a factor, nor can the oxidation of tyrosine residues to their radical forms by $Ru(bpy)_3^{3+}$. However, the success preparing ferryl Mb by flash-photolysis of photooxidants covalently tethered to the heme suggests that it is thermodynamically

possible to oxidize Mb to ferryl Mb, but that the oxidizing equivalents are consumed as protein based radicals, which eventually leads to decomposition of the heme. Addition of a group that provides a stable sink for oxidizing equivalents such as thiol group also appears to prevent irreversible decomposition of the heme; however, the nature of the oxidized heme species produced is unclear.

References and Notes

(1) Valentine, J. S. In *Bioinorganic Chemistry*; I. Bertini, H. B. Gray, S. J. Lippard and J. S. Valentine, Eds.; University Science Books: Mill Valley, California, 1994; pp 253-315.

(2) Bren, K. L.; Gray, H. B.; Banci, L.; Bertini, I.; Turano, P. *J. Am. Chem. Soc.* **1995**, *117*, 8067-8073.

(3) Levitt, M. H.; Freeman, R. *J. Magn. Reson.* **1981**, *48*, 65-80.

(4) Arasasingham, R. D.; Cornman, C. R.; Balch, A. L. *J. Am. Chem. Soc.* **1989**, *111*, 7800-7805.

(5) Shin, K.; Goff, H. M. *J. Am. Chem. Soc.* **1987**, *109*, 3140-3142.

(6) Calderwood, T. S.; Bruice, T. C. *Inorg. Chem.* **1986**, *25*, 3722-3724.

(7) Tsuchiya, S. *J. Chem. Soc. Chem. Commun.* **1991**, 716-717.

(8) Bell, S. E. J.; Cooke, P. R.; Inchley, P.; Leanord, D. R.; Smith, J. R. L.; Robbins, A. *J. Chem. Soc. Perkin Trans.* **1991**, *2*, 549-559.

(9) Traylor, T. *Pure Appl. Chem.* **1991**, *63*, 265-274.

(10) Groves, J. T.; Watanabe, Y. *J. Am. Chem. Soc.* **1988**, *110*, 8443-8452.

(11) Urry, D. W.; Pettegrew, J. W. *J. Am. Chem. Soc.* **1967**, *89*, 5276-5283.

(12) Sklenar, V.; Bax, A. *J. Magn. Reson.* **1987**, *71*, 379-383.

(13) Banci, L.; Bertini, I.; Pierattelli, R.; Vila, A. J. *Inorg. Chem.* **1994**, *33*, 4338-4343.

(14) Kobayashi, N.; Osa, T. *Chem. Pharm. Bull.* **1989**, *37*, 3105-3107.

(15) Hayashi, Y.; Yamazaki, I. *J. Biol. Chem.* **1979**, *254*, 9101-9106.

(16) Kimura, K.; Peterson, J.; Wilson, M.; Cookson, D. J.; Williams, R. J. P. *J. Inorg. Biochem.* **1981**, *15*, 11-25.

(17) Wang, J.-S.; Tsai, A.-L.; Heldt, J.; Palmer, G.; Van Wart, H. E. *J. Biol. Chem.* **1992**, *267*, 15310-15318.

(18) Frye, J. S.; Mar, G. N. L. *J. Am. Chem. Soc.* **1975**, *97*, 3561-3562.

(19) Wang, J.-S.; Baek, H. K.; Van Wart, H. E. *Biochem. Biophys. Res. Commun.* **1991**, *179*, 1320-1324.

(20) Tatsuma, T.; Watanabe, T. *Anal. Chem.* **1991**, *63*, 1580-1585.

(21) Othman, S.; Lirzin, A. L.; Desbois, A. *Biochemistry* **1994**, *33*, 15437-15448.

(22) Wuttke, D. S.; Bjerrum, M. J.; Winkler, J. R.; Gray, H. B. **1992**, *256*, 1007-1009.

(23) Turner, D. L.; Salgueiro, C. A.; Schenkels, P.; LeGall, J.; Xavier, A. V. *Biochim. Biophys. Acta* **1995**, *1246*, 24-28.

(24) Macura, S.; Ernst, R. R. *Mol. Phys.* **1980**, *41*, 95-117.

(25) Bertini, I.; Luchinat, C. In *Physical Methods for Chemists*; 2 ed.; R. Drago, Ed.; Saunders College Publishing: San Diego, CA, 1992.

(26) Kjaer, M.; Andersen, K. V.; Poulsen, F. M. *Methods Enzymol.* **1994**, *239*, 288-307.

(27) States, D. H.; Haberkorn, R. A.; Ruben, D. J. *J. Magn. Reson.* **1982**, *68*, 509-517.

(28) Moore, G. R.; Pettigrew, G. W. In *Cytochromes c*; Springer Verlag: New York, 1990; pp 174.

(29) Baldwin, D. A.; Marques, H. M.; Pratt, J. M. *J. Inorg. Biochem.* **1986**, *27*, 245-254.

(30) Liu, R.-Q.; Miller, M. A.; Han, G. W.; Hahm, S.; Geren, L.; Hibdon, S.; Kraut, J.; Durham, B.; Millett, F. *Biochemistry* **1994**, *33*, 8678-8685.

(31) Turner, D. L. *Eur. J. Bioch.* **1995**, *227*, 829-837.

(32) Timkovich, R. *Inorg. Chem.* **1991**, *30*, 37-42.

(33) Vold, R. L.; Waugh, J. S.; Klein, M. P.; Phelps, D. E. *J. Chem. Phys.* **1968**, *48*, 3831-3832.

(34) Erman, J. E.; Vitello, L. B.; Mauro, J. M.; Kraut, J. *Biochemistry* **1989**, *28*, 7992-7995.

(35) Fulop, V.; Phizackerly, R. P.; Soltis, S. M.; Clifton, I. J.; Wakatsuki, S.; Erman, J.; Hajdu, J.; Edwards, S. L. *Structure* **1994**, *2*, 201-208.

(36) Berglund, J.; Pascher, T.; Winkler, J. R.; Gray, H. B. *J. Am. Chem. Soc.* **1997**, *119*, 2464-2469.

(37) Low, D. W.; Winkler, J. R.; Gray, H. B. *J. Am. Chem. Soc.* **1996**, *118*, 117-120.

(38) Allentoff, A. J.; Bolton, J. L.; Wilks, A.; Thompson, J. A.; Montellano, P. R. O. d. *J. Am. Chem. Soc.* **1992**, *114*, 9744-9749.

(39) George, P.; Irvine, D. H. *Biochem. J.* **1955**, *60*, 596-604.

(40) De Pillis, G.; Decatur, S. M.; Barrick, D.; Boxer, S. G. *J. Am. Chem. Soc.* **1994**, *116*, 6981-6982.

(41) Barrick, D. *Biochemistry* **1994**, *33*, 6546-6554.

(42) Sono, M.; Roach, M. P.; Coulter, E. D.; Dawson, J. H. *Chem. Rev.* **1996**, *96*, 2841-2887.

Chapter 5: Covalent Modification of Microperoxidases by Reverse Proteolysis

Introduction

Small molecule analogs of the active sites of heme proteins are under investigation in many laboratories.[1-3] Covalent attachment of ligands to the porphyrins is often desirable as it reduces complications due to axial ligand dissociation and scrambling in cases involving mixed axial ligation.[4-9] The preparation of ligand-linked (tailed) porphyrin systems, however, often involves complex multi-step syntheses. We have found that trypsin-catalyzed reverse proteolysis[10,11] provides a simple preparative route to a novel class of water-soluble tailed porphyrins based on the well-characterized microperoxidase (MP) framework.[12-22] Using reverse proteolysis reactions, we have obtained mutant microperoxidase decapeptides (MP10s) with C-terminal histidine (H23MP10), tyrosine (Y23MP10), and methionine (M23MP10) residues. In addition, we have investigated the electronic absorption and resonance Raman spectra of these MP10 mutants.

The synthesis of polypeptide chains by the classical solid-phase methodology using activated esters to effect condensation involves extensive use of orthogonal protecting groups to ensure that only a single condensation reaction occurs in solution. The use of protecting group is necessary because the reaction of the activated esters is inherently non-selective in nature. This lack of chemical selectivity renders the use of classical peptide coupling techniques ineffective for the coupling of unprotected peptide segments. In principle, peptide coupling catalyzed by enzymes should be specific and take place under mild reaction conditions; enzymatic systems mediate the specific synthesis of highly elaborate protein polypeptides under physiological conditions. Unfortunately, the peptidyl aminotransferase systems of living organisms are extremely complex and cumbersome to work with. A less complex approach that incorporates the natural selectivity of enzyme catalysis into a peptide bond forming reaction involves reversing the normal reaction course of a protease enzyme (reverse proteolysis).

The physiological role of protease enzymes is to effect the hydrolysis of peptide bonds. In the thermodynamic method of reverse proteolysis, conditions are sought such that the equilibrium is shifted sufficiently towards the reverse of hydrolysis, and the enzyme effectively catalyzes the formation of a peptide bond. Alternatively, the kinetic method of reverse proteolysis involves use of a mildly activated C-terminal ester of one of the peptides to be joined. This ester reacts rapidly with the enzyme (a serine or cysteine protease) to produce an acylated enzyme intermediate which is then deacylated by an incoming amino acid nucleophile, resulting in peptide bond formation. The hydrolysis of this new peptide is relatively slow compared to the reaction of the activated C-terminus, causing the product to transiently accumulate in solution.[23] In both the thermodynamic and kinetic methods, a large excess of amino acid nucleophile is employed to either alter the equilibrium constant in favor of peptide synthesis, or to increase the rate of deacylation of the enzyme intermediate that results in peptide synthesis. The thermodynamic method typically also requires that water be removed from the reaction by the use of low-water content organic solvent systems to further shift the equilibrium in favor of the desired product. Solvents systems with as little as 1% water have been employed with reasonable success, resulting in yields of peptide bond formation $\geq$ 90%.[24]

Reverse proteolysis is ideal for applications that involve condensation of small unprotected segments that contain only a single hydrolytic site for the enzyme used for catalysis. While practical applications of reverse proteolysis have been primarily limited to simple condensation reactions to form simple dipeptides such as the thermolysin mediated preparation of the dipeptide ester aspartame (traditional solid-phase chemical synthesis remains the method of choice for preparation of most longer peptides), advances in reverse proteolysis methodology have made the enzymatic synthesis of certain small oligopeptides possible. Successful applications of reverse proteolysis in the synthesis of natural products include the preparation of the delta-sleep inducing

nonapeptide (WAGGDASGE) by Sakina and coworkers[25] in which each of the peptide bonds was formed using either papain or chymotrypsin mediated peptide bond forming reactions, and the preparation of the highly functionalized "delicious peptide" (KGDEESLA) that used six different proteases (chymotrypsin, chymopapain, subtilisn, V8 protease, proteinase K and proteinase E) to form the 7 peptide bonds.[26] Other proteases commonly employed in reverse proteolysis reactions are elastase,[11] carboxypeptidases[27] and trypsin.[10,28]

Trypsin is a member of the serine protease family of hydrolytic enzymes, and contains at its active site a classic catalytic triad of serine, histidine and aspartate residues. The S residue serves as a nucleophile in the hydrolytic reaction, attacking the carbonyl group of the P_1 residue, leading to the formation of a tetrahedral intermediate in the reaction. Hydrolysis of this intermediate by water results in the release of the truncated substrate. Trypsin's P_1 specificity for the positively charged amino acids K and R originates in the presence of a negatively charged D residue near the substrate binding site. Trypsin has been reported to be active in peptide bond forming reactions in a number of organic/aqueous solvent systems, including DMF, acetonitrile, and hexafluoroisopropanol based systems. We have exploited trypsin's P_1 specificity in a reverse proteolysis scheme to selectively add amino acids to the C-terminus K22 of MP9.

Experimental Section

Materials: Dimethyl formamide was obtained from Burdick and Jackson. Hexafluoroisopropanol was obtained from Sigma. Amino acid amides, esters and hydrazides were purchased in enantiomerically pure forms except as noted from Bachem, CA. Carbohydrazide was purchased from Fluka. The trypsin (Sigma) used for reverse proteolysis reactions was treated with a chymotrypsin inhibitor (TPCK or DPCC) and used as received. MP9 was prepared and purified as described in Chapter 2.

Methods:

General Peptide Coupling Reactions:

Peptide coupling reactions were carried out in 50% DMF/ 50% water containing 50 mM TRIS HCl, 100 mM NaCl and 10 mM $CaCl_2$. Reactions were terminated by addition of excess glacial acetic acid, followed by washing in an Amicon stirred cell (YM-1 membrane) with 0.1% TFA. Except as noted, all reaction mixtures were purified by a standard FPLC purification routine. Buffer A was 0.1% TFA and buffer B was 60% acetonitrile, 40% water with 0.1% TFA added. For preparative scale reactions, a Pharmacia 16/10 PepRPC column was used. The crude peptide solution was applied to the column using a 10 mL SuperLoop fitted with solvent resistant Kel-F O-rings. The crude peptide was washed at the top of the column with a 20% B solution for 10 minutes, after which a gradient to 60% B was initiated. Except as noted, a flow rate of 5 mL/min was used. The column was inspected visually during the run, and in most cases bands corresponding to heme containing product and reactant were clearly visible and were collected manually. For analytical FPLC, a Pharmacia 5/5 PepRPC column was used. The crude peptide solution was applied to the column and a gradient from 0 - 100% B was immediately initiated. As with the preparative scale reactions, bands corresponding to the heme-containing product and reactants were easily seen on the column and collected manually. A flow rate of 1 mL/min was used for all analytical runs. UV-visible spectra were collected on a Hewlett-Packard 8542A diode array spectrophotometer. Extinction coefficients for heme peptides were determined by the pyridine hemochrome method.[29] Yields were estimated from FPLC peak areas using the integrating feature of UN-SCAN-IT on digitized chromatograms. The molar absorbance at 254 was considered to be the same for MP9 starting materials and X23MP10 peptides; no attempt was made to determine response functions for the peptides.

Preparation of H23MP10

For large scale preparations of H23MP10 for NMR and MCD measurements, 0.91 g of His-NH_2 • 2 HCl was dissolved in minimal water and titrated to the isoelectric point (pH 7.25) with sodium hydroxide solution. The solution of free-base His-NH_2 was lyophilized to dryness. The resulting off-white solid was treated with anhydrous DMF (4 mL). After thorough mixing, the sodium chloride was removed by centrifuging the mixture and decanting off the supernatant. The DMF solution of His-NH_2 was then added to solid lyophilized MP9 (40 mg) resulting in a deep red solution. 20 mg of trypsin was then dissolved in 4 mL of the TRIS buffer described in the general section, and this was slowly added to the DMF containing the His-NH_2 and MP9. The reaction was allowed to stir gently overnight, after which time the progress of the reaction was stopped by addition of acetic acid. Enough acetic acid was added to turn the solution from red to brown (pH ~ 2). The brown solution was diluted to 40 mL with 0.1% TFA and concentrated in an Amicon stirred cell. After washing 2 X with 0.1% TFA, the crude mixture was purified by FPLC using the standard protocol described in the general experimental section. H23MP10 elutes slightly earlier than the MP9 starting material (~ 45% B) (Figure 5.1). The identity of the product was confirmed by MALDI mass spectrometry, m/z calculated 1771 amu, m/z 1770.9 observed (Figure 5.2). Yields estimated from the FPLC peak areas are approximately 30%. This general procedure works equally well for smaller scale preparations.

Preparation of W23MP10

0.24 g of Trp-NH_2 • HCl was dissolved in minimal water and titrated to its isoelectric point using sodium hydroxide solution. The water was removed by lyophylization and the remaining solid was treated with anhydrous DMF (1 mL). After

Figure 5.1: FPLC trace of H23MP10 obtained with a 16/10 PepRPC column using the standard protocol for heme peptide purification. The arrow indicates the product H23MP10 peak.

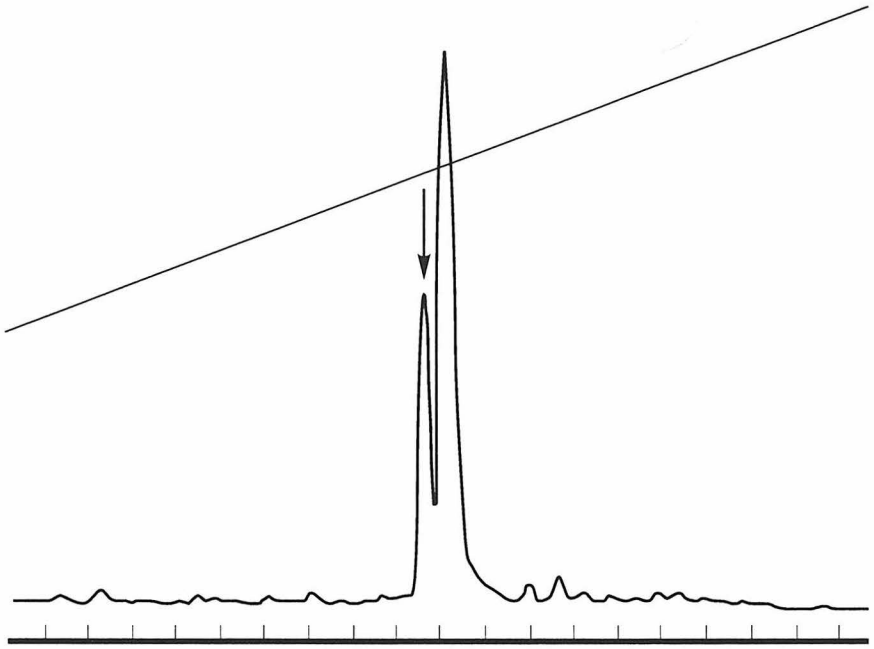

Figure 5.2: MALDI mass spectrum of purified H23MP10 (20 μM solution in ca. 30% acetonitrile/water 0.1% TFA).

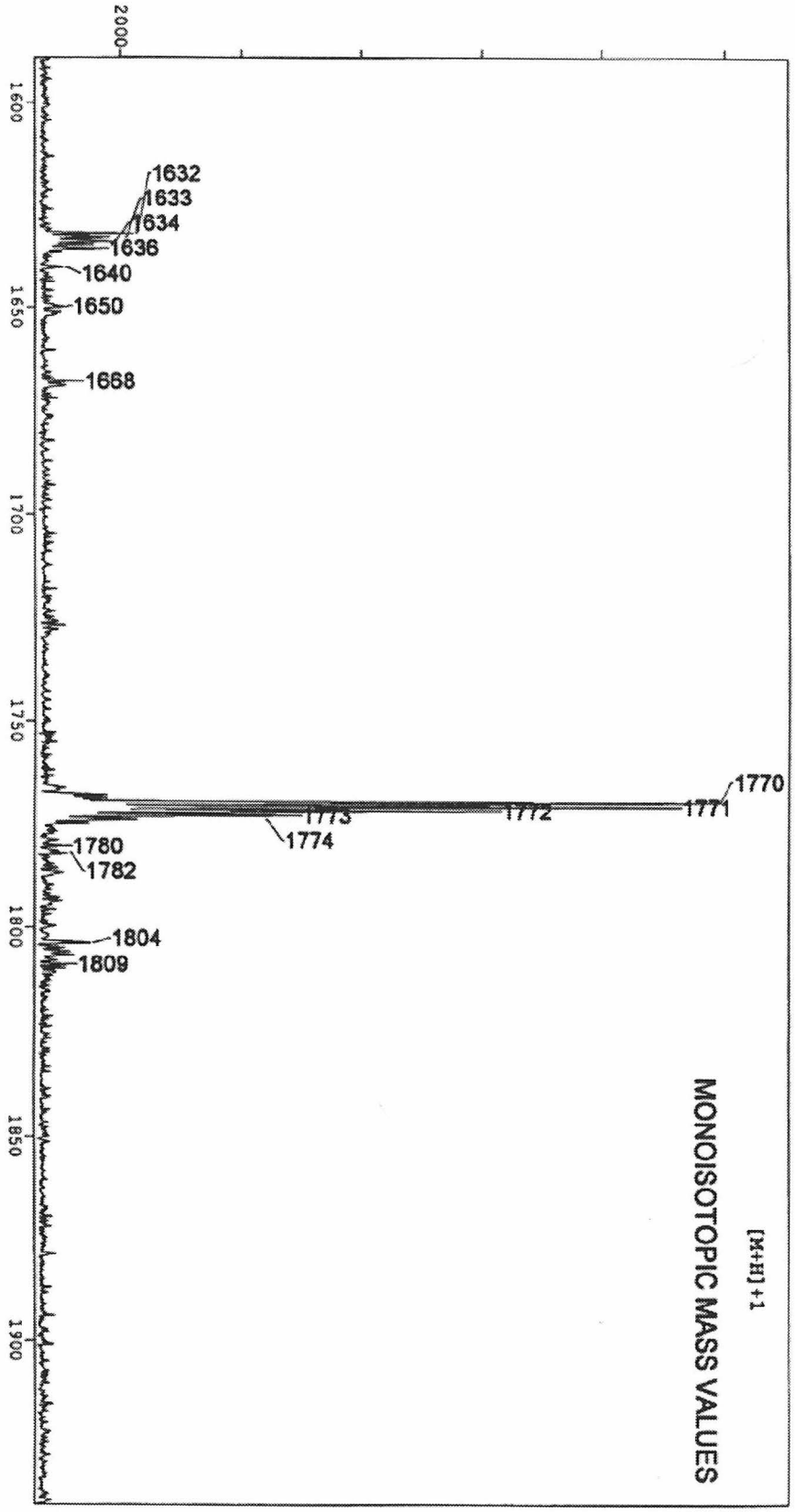
2000
1600
1650
1700
1750
1800
1850
1900
1632
1633
1634
1636
1640
1650
1668
1770
1771
1772
1773
1774
1780
1782
1804
1809
MONOISOTOPIC MASS VALUES
[M+H]+1

mixing, the solid sodium chloride was removed by filtration through a glass fritted disc or by centrifugation. The DMF solution containing Trp-NH_2 was then added to 3 mg of MP9. 25 mg of trypsin was dissolved in 1 mL of the standard TRIS buffer described above. The trypsin containing solution was added to the DMF solution of MP9 and Trp-NH_2 and the reaction was allowed to proceed overnight with gentle stirring. 1 mL of glacial acetic acid was then added, and the mixture was diluted to 10 mL with water, concentrated and washed repeatedly in an Amicon cell. The crude mixture was purified on a 16/10 PepRPC column using a modification of the standard FPLC protocol described above, in which the gradient is allowed to run up 100% B. The second heme-containing fraction eluting at ca. 60% B corresponds to the W23MP10 peptide (Figure 5.3). UV-vis absorption spectra of these fractions features an additional absorption in the UV at 280 nm (shoulder) that is consistent with the presence of the Trp-NH_2 residue. These fractions also exhibit fluorescence in the region expected for Trp emission (λ_{max} ~ 340 nm) (Figure 5.4). MALDI mass spectra (Figure 5.5) are also consistent with the addition of Trp-NH_2: m/z calculated: 1821 amu, m/z observed: 1820.4 amu.

Preparation of M23MP10

0.18 g of Met-NH_2 • HCl was dissolved in minimal water and titrated to pH 8 with sodium hydroxide solution. The free base solution of Met-NH_2 was lyophilized overnight, and the resulting solid was treated with DMF (1 mL). Sodium chloride was removed by centrifugation. The resulting clear solution was added to 7 mg of lyophilized MP9 to give a dark red solution. 25 mg of trypsin was dissolved in 1 mL of the standard TRIS buffer described above and added to the DMF solution. The reaction mixture was allowed to stir gently overnight. The reaction was stopped by addition of 1 mL of glacial acetic acid. The solution was diluted to 10 mL with 0.1% TFA, and concentrated in an Amicon stirred cell. The concentrated crude mixture was passed down a Sephadex G-25

Figure 5.3: FPLC trace for the purification of W23MP10. The arrows indicate fractions that contain the product W23MP10 diastereomers. The absolute stereochemistry of the two fractions has not been determined.

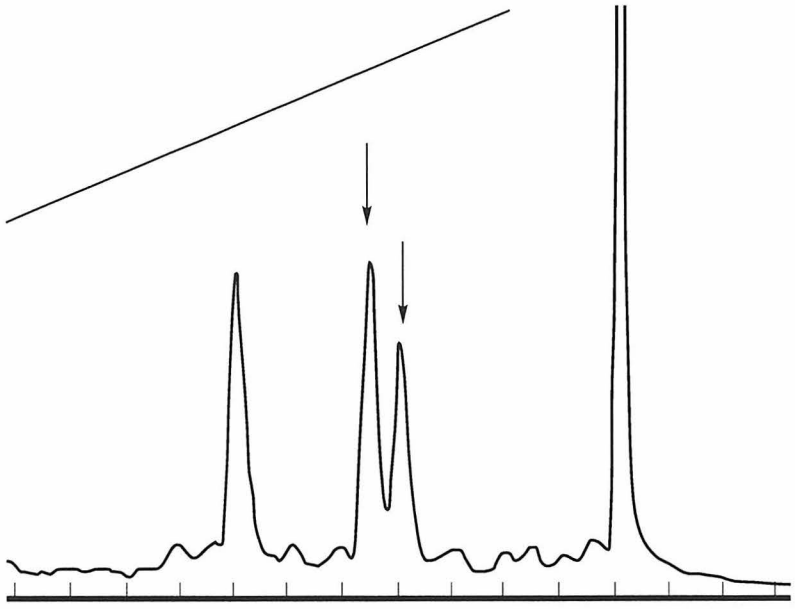

Figure 5.4: Static fluorescence spectrum of W23MP10. Solution contained ca. 30% acetonitrile in water with 0.1% TFA.

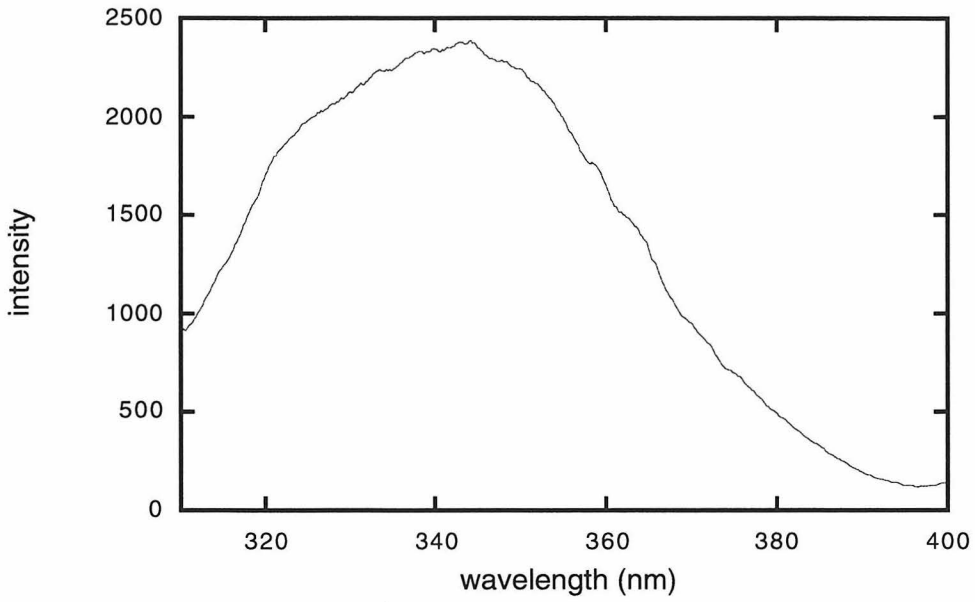
2500
2000
1500
1000
500
0
intensity
320
340
360
380
400
wavelength (nm)

Figure 5.5: MALDI mass spectrum of purified W23MP10 (20 μM solution in ca. 30% acetonitrile/water 0.1% TFA).

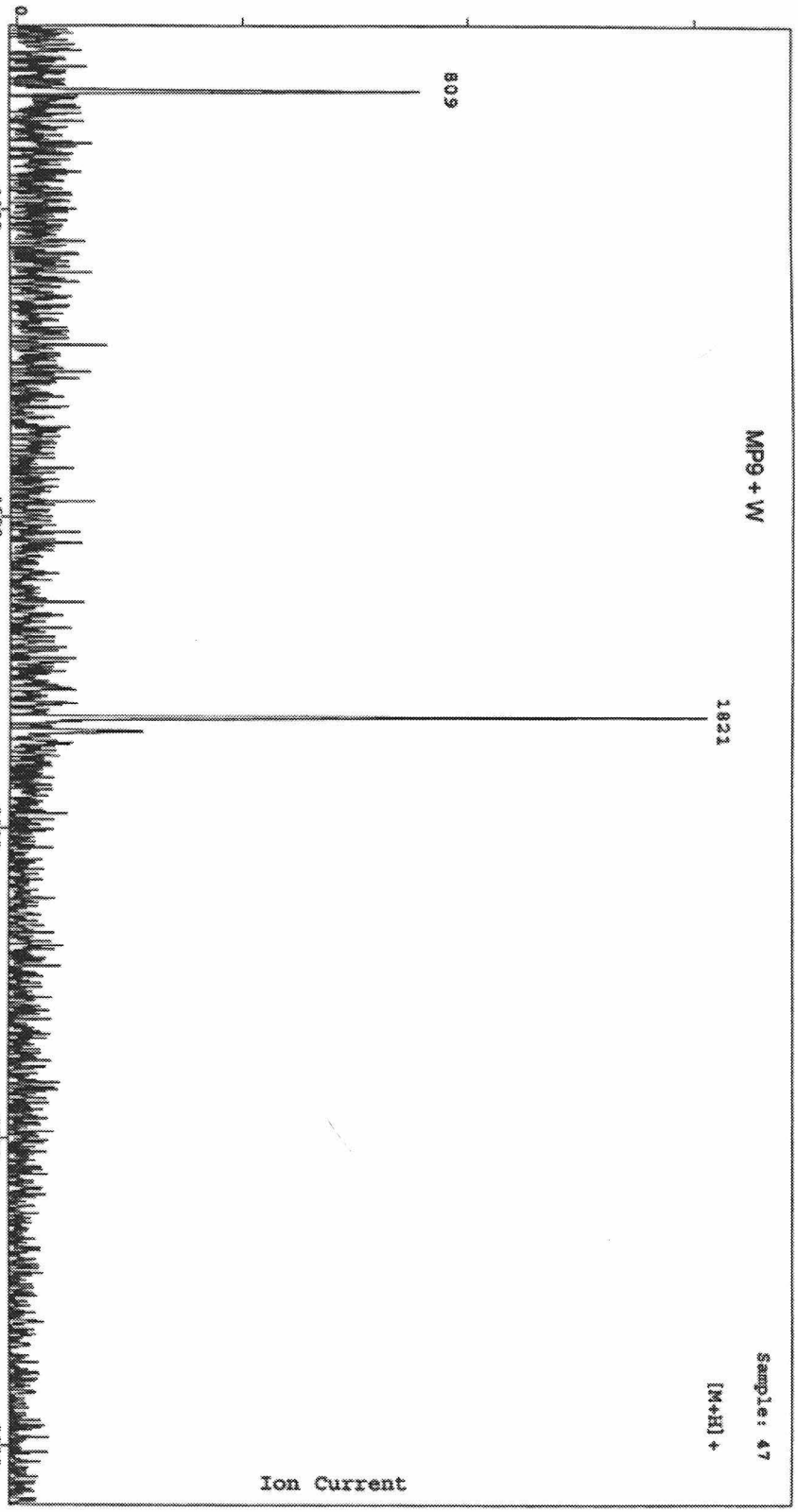
809
1821
MDP + W
Sample: 47
[M+H] +
Ion Current
0
1000
1500
2000
2500
3000

(Pharmacia PD-10) column, then applied to a Pharmacia 16/10 PepRPC column and purified according to the standard FPLC protocol described above. M23MP10 elutes at 43% B, later than MP9, as expected for the addition of a relatively hydrophobic M residue (Figure 5.6). The identity and purity of the addition product was verified by MALDI mass spectrometry (Figure 5.7). m/z calculated: 1767 amu, m/z observed: 1766 amu. Yields were estimated to be 42%.

Preparation of Y23MP10

Free base Tyr-NH_2 was prepared by titrating a solution of Tyr-NH_2 • HCl (0.23 g) with sodium hydroxide solution to pH 8, and removing the solvent by lyophylization. The solid was treated with 1 mL of DMF, and the solid sodium chloride remaining was centrifuged out. 5 mg of MP9 was dissolved in the resulting DMF solution of free base Tyr-NH_2. 25 mg of trypsin was dissolved in 1 mL of the standard TRIS buffer described above, and slowly added to the DMF solution. The reaction was allowed to stir overnight. The progress of the reaction was stopped by addition of 1 mL of glacial acetic acid. The brown solution was concentrated and washed 2 X in an Amicon stirred cell and purified on a 16/10 PepRPC column using the standard FPLC protocol described above. Y23MP10 elutes as a large fraction at 48% B (Figure 5.8). The identity and purity of the peptide were assayed by MALDI mass spectrometry. m/z calculated: 1797 amu, m/z observed: 1796.7 amu (Figure 5.9). Yields were estimated to be 40%.

Figure 5.6: FPLC trace for the purification of M23MP10. The arrow indicates the M23MP10 product peak. The other major peak eluting earlier is MP9 starting material.

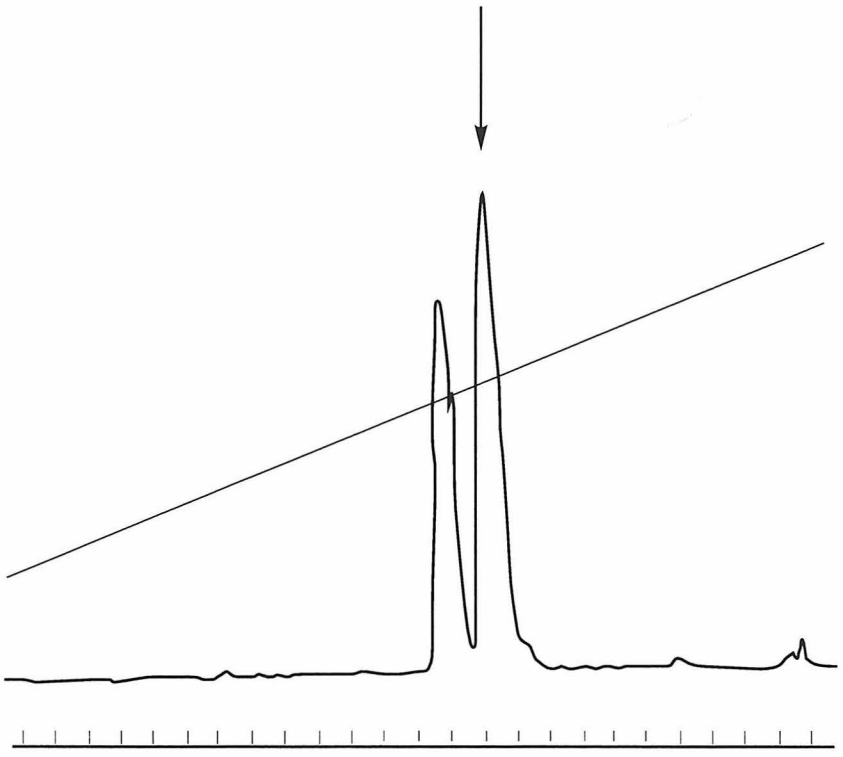

Figure 5.7: MALDI mass spectrum of M23MP10 (20 μM solution in ca. 30% acetonitrile/water 0.1% TFA).

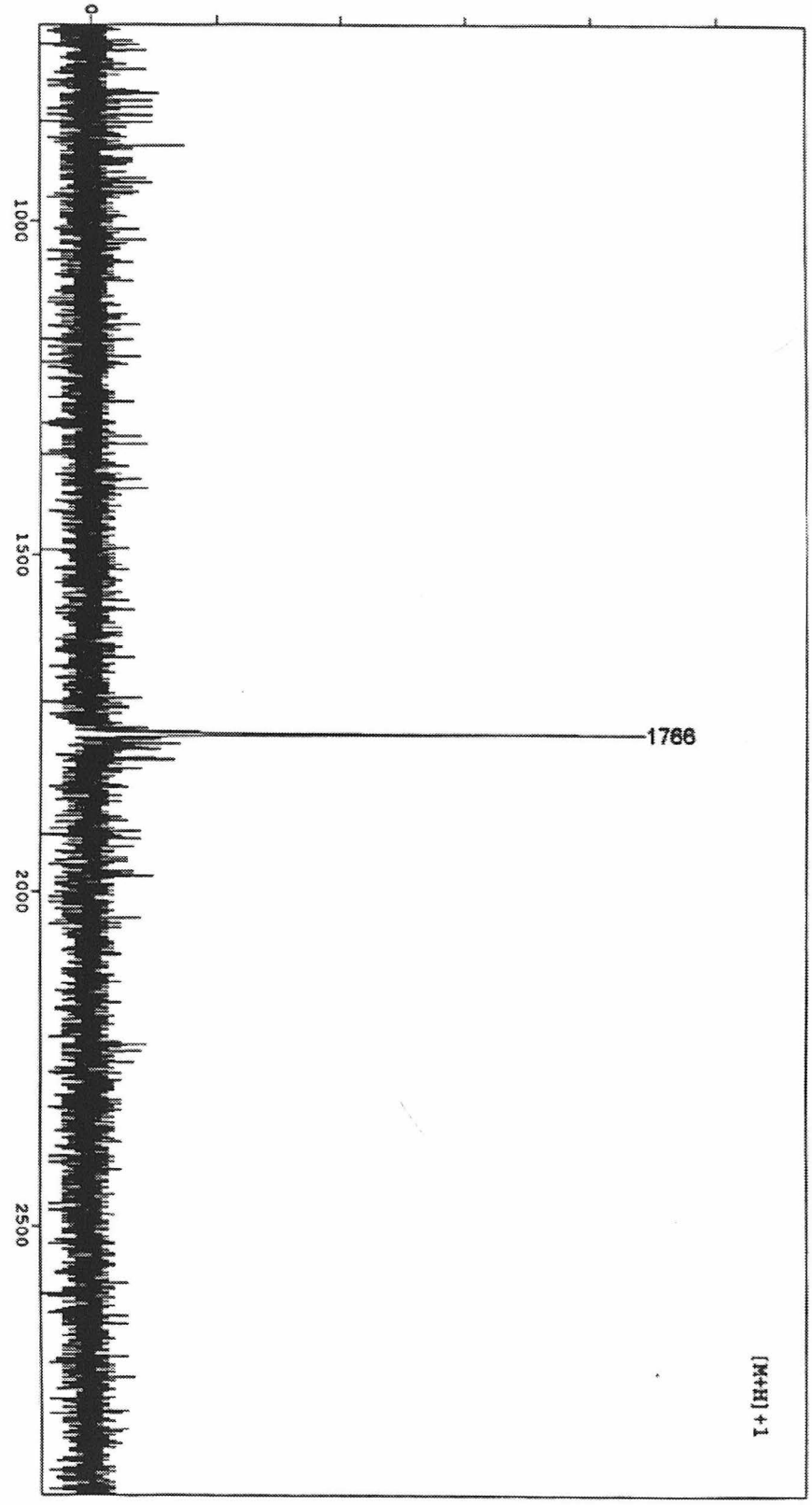
0
1000
1500
2000
2500
1766
[M+H] +1

Figure 5.8: FPLC trace for the purification of Y23MP10. The arrow indicates the peak containing the product Y23MP10 and the other major peak eluting earlier is MP9 starting material.

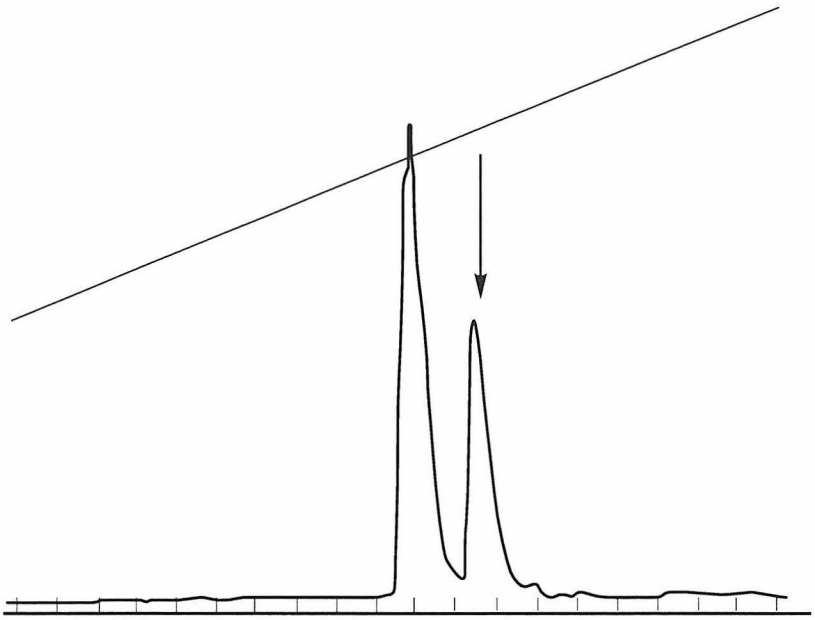

Figure 5.9: MALDI mass spectrum of purified Y23MP10 (20 μM solution in ca. 30% acetonitrile/water 0.1% TFA).

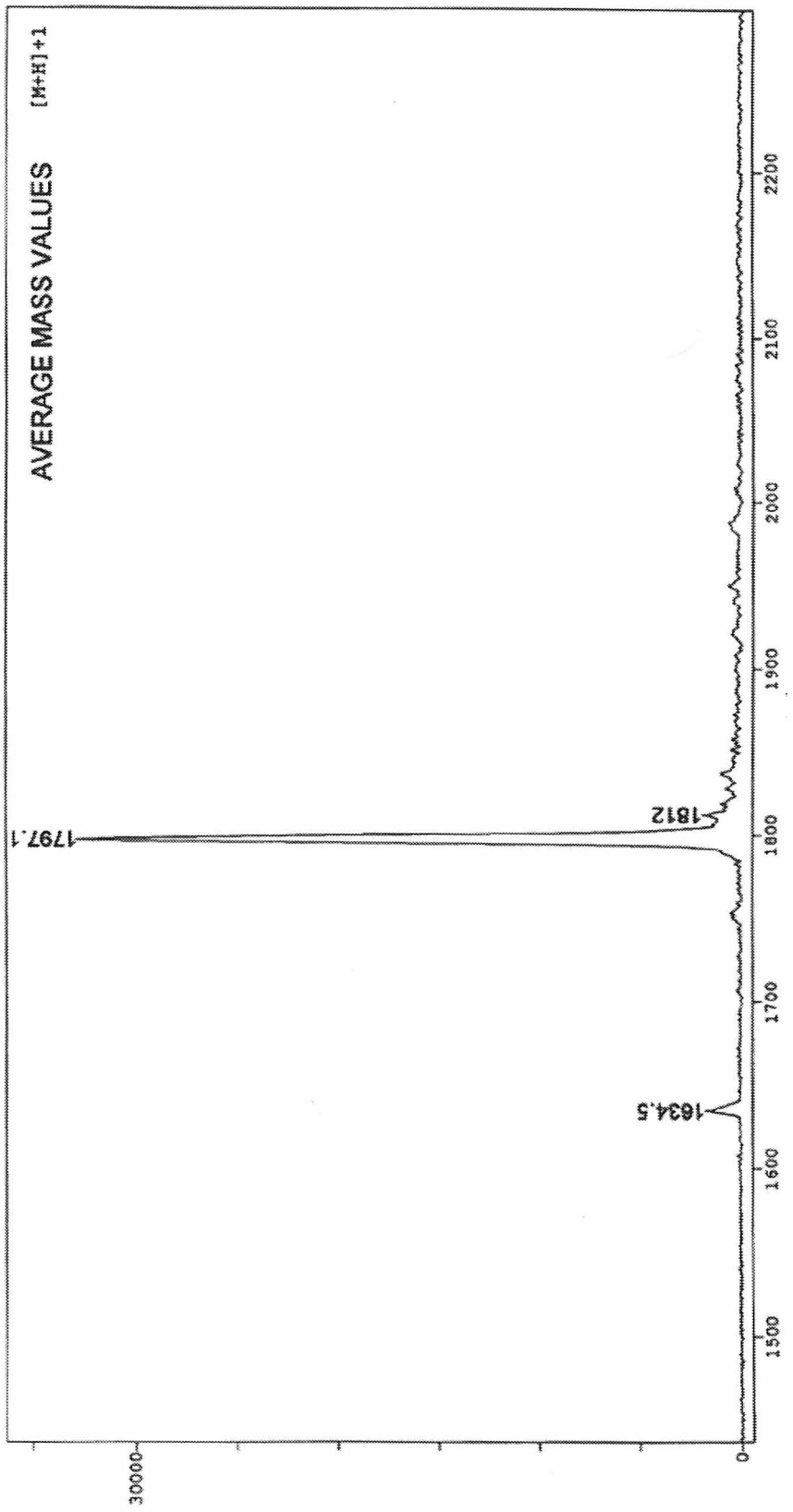
AVERAGE MASS VALUES
[M+H]+1
1797.1
1812
1634.5
30000
0
1500
1600
1700
1800
1900
2000
2100
2200

Preparation of γ23MP10

Gly-NH-NH-Z (γ, 0.34 g) was dissolved in minimal water and titrated with sodium hydroxide to pH 8. The resulting solution of free-base γ was dried by lyophylization overnight, and the resulting solid dissolved in DMF (1 mL). No attempt was made to remove the sodium TFA present in the reaction mixture. The DMF solution was added to ~ 1 mg of MP9. 25 mg of trypsin was dissolved in the standard TRIS buffer described above, and slowly added to the DMF solution. The reaction was allowed to stir overnight, after which it was quenched with 1 mL of acetic acid followed by washing with 0.1% TFA. The crude mixture was fractionated using a 5/5 PepRPC column running the standard FPLC protocol described earlier. γ23MP10 elutes after MP9 at 46% B (Figure 5.10). The product was identified by MALDI mass spectrometry (Figure 5.11). m/z calculated: 1839 amu. m/z observed: 1841 amu.

Resonance Raman Spectroscopy

Excitation at 406 nm for resonance Raman spectroscopy was provided by an Lambda-Physik FL3002 dye laser using PBBO dye pumped by an LPX 210i excimer laser operating at 10-50 Hz, approximately 1 mJ per pulse at 406 nm at the sample. Probe light was purified using a diffraction grating (1200 grooves/mm) followed by tight focusing and passage through a 20 μm aperture to reject off-axis light. Raman light was collected using a right-angle collection geometry. Scattered light was focused on the aperture of a SPEX 750 M monochromator equipped with a cooled CCD array detector interfaced to a PC running the commercial WinSpec data collection package. Typical acquisition times were 1-5 minutes, with sample concentrations between 50-100 μM. All spectra were collected at ambient temperature. Cosmic ray artifacts have been removed

Figure 5.10: FPLC trace for the purification of γ23MP10. The arrow indicates the product γ23MP10 peak. The other major peak eluting earlier is MP9 starting material.

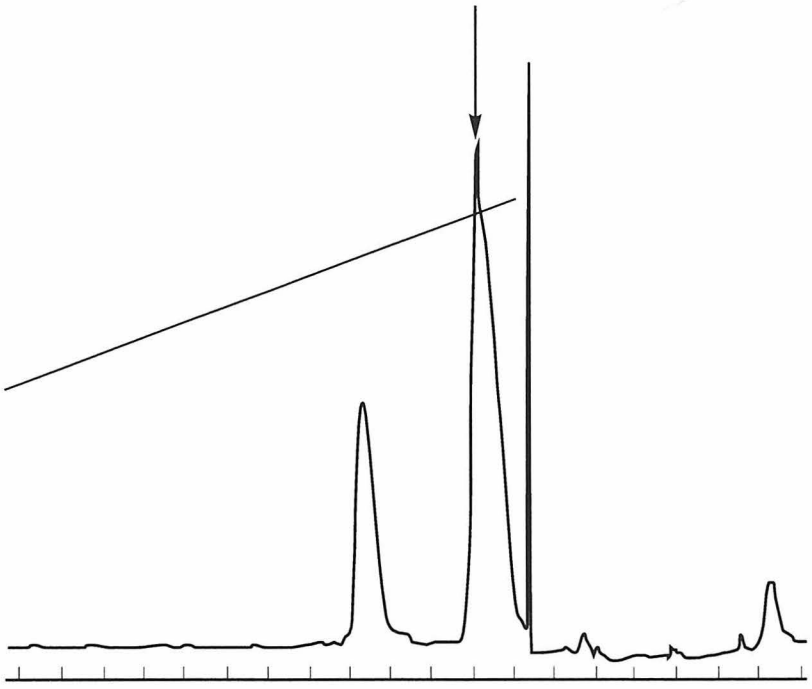

Figure 5.11: MALDI mass spectrum of purified γ23MP10 (20 μM solution in ca. 30% acetonitrile/water 0.1% TFA).

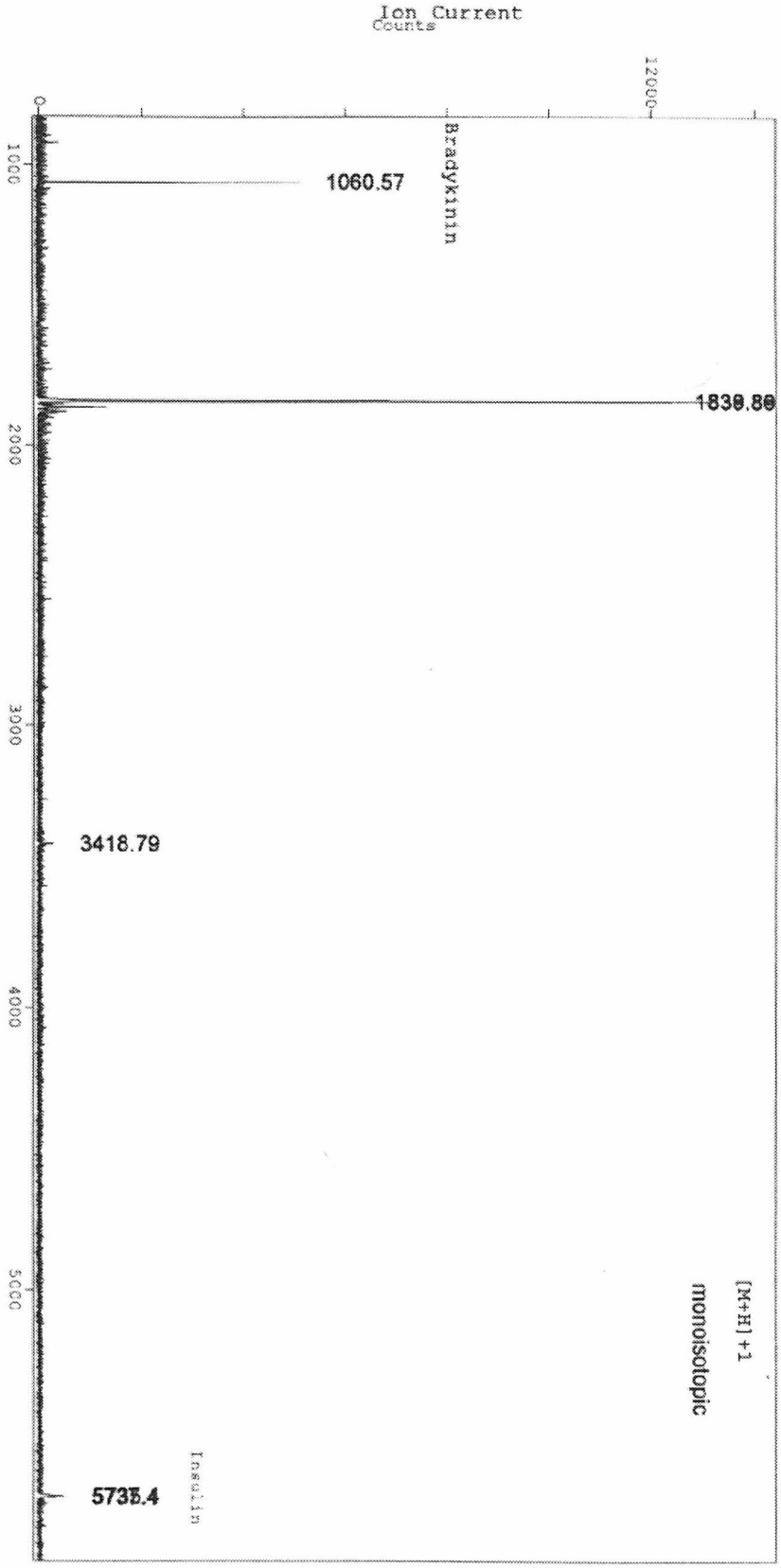
Ion Current
Counts
0
1000
2000
3000
4000
5000
12000
Bradykinin
1060.57
1839.80
3418.79
5735.4
Insulin
[M+H]+1
monoisotopic

from the spectra using a house-written MatLab macro. The CCD detector response was calibrated using a standard ArHg lamp. A spectrum was taken of the lamp output, and a linear scale was constructed assuming that the CCD array spans 29 nm. The known wavelengths of emission lines from the lamp were compared with their observed wavelengths from the linear scale, and appropriate corrections were noted. The corrections were fitted to a smooth curve in Kaliedagraph, and the function describing the curve was used to correct the CCD output over the entire wavelength range (Figure 5.12).

Miscellaneous

Static tryptophan fluorescence spectra were collected on a Hitachi F-4500 fluorimeter in Dr. Thomas Meade's laboratory. The fluorescence lifetime of tryptophan residues were determined by time-correlated single-photon counting. Matrix-assisted laser desorption mass spectra were measured by Gary Hathaway as described in Chapter 2.

Results and Discussion

Peptide Chemistry - Preparation of X23 Microperoxidases

Since MP9 is a product of tryptic hydrolysis of cytochrome *c*, we reasoned that it should also readily participate as a substrate in the reverse reaction, trypsin-catalyzed peptide bond formation. Further, the high selectivity of trypsin-catalyzed reactions should minimize side products and circumvent the use of protecting groups. The use of mixed aqueous-organic solvent systems and addition of high concentrations of amino-acid nucleophiles shift the peptide bond formation/hydrolysis equilibrium in favor of the peptide synthesis reaction; in fact, we have found that trypsin is effective in promoting peptide bond formation with MP9 as a substrate in 50% aqueous dimethylformamide

Figure 5.12: Calibration curve for the SPEX 750 M Raman monochromator's CCD detector for spectra collected around a center wavelength of 425.5 nm, with probe wavelength 406 nm. The smooth curve is the equation that describes the correction applied as a function of wavelength, $y = 1.78 \times 10^{-7} (x^2) - 3.1 \times 10^4 (x) + 0.02051$.

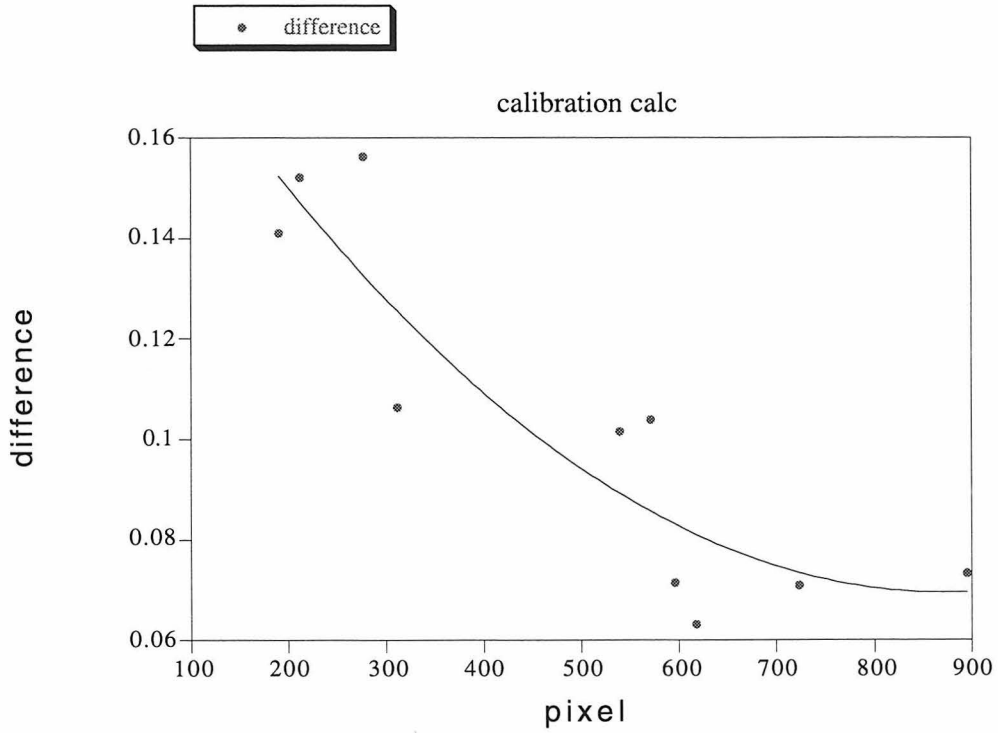
difference
calibration calc
0.16
0.14
0.12
0.1
0.08
0.06
difference
100
200
300
400
500
600
700
800
900
pixel

(DMF) solutions, and were able to produce a number of X23MP10 derivatives in modest to good yields. The product decapeptides were readily separated from the MP9 starting material by reverse-phase FPLC with acetonitrile-water gradients. Due to the high selectivity for positively charged P_1 residues inherent in trypsin catalysis, only one heme-containing product was observed when enantiomerically pure amino-acid amides were employed as nucleophiles. Reverse proteolysis succeeded in forming peptide bonds between MP9 and all amino acid amides tested, including histidine, tyrosine, methionine, and tryptophan. Analysis by MALDI mass spectrometry were in general consistent with the presence of a single heme-containing product. The use of hexafluoroisopropanol (HFIP) as a cosolvent with aqueous DMF has been reported to allow the use of extremely low water content solvent mixtures (~ 6%) in reverse proteolysis reactions, resulting in extremely efficient peptide coupling (yields ≤ 90%).[10] We briefly investigated the use of HFIP containing solvents for use in MP peptide couplings, and found no significant advantage over simple aqueous DMF solutions.

The success of the trypsin catalyzed reverse proteolysis approach contrasts with our many attempts to add amino acids using traditional peptide chemistry methods. A wide variety of activated amino acid esters (pentafluorophenoxy (PTFP), hydroxybenztriazole (HOBT), dicyclohexyldicarbodiimide (DCC) and EDC and DCI were all tried as activating groups) were reacted with MP8 in DMF or water; however, in most cases, no reaction was observed, and no addition products were ever isolated from these reactions.

Addition of D-Amino Acids

While much of the peptide chemistry was done with enantiomerically pure amino acid derivatives, interestingly, when a racemic mixture of amino acid amide nucleophiles were serendipitously employed (the initial experiment that lead to this discovery was the addition of *rac*-Trp-NH_2 to MP9, by chance the only form available from Bachem), *two*

product peaks were observed (Figure 5.3), possibly corresponding to incorporation of both the natural L-enantiomer as well as the unnatural D-enantiomer into the new MP10 molecule, since the mass spectrometry of a fraction containing both peaks resulted in a mass corresponding to that expected for a W23MP10 mutant. Although the two addition products have identical molecular masses, they would be diastereomers of each other, and, at least in principle, have different FPLC retention times. To confirm this, separate experiments were carried out using enantiomerically pure L and D-tryptophan and methionine amides, and all four diastereomeric addition products were obtained in reasonable yields. This suggests that trypsin does not appear to discriminate strongly based on the structure of the incoming nucleophile's backbone, implying that a wide variety of amino-acid like nucleophiles may be accepted into the active site for reaction. Papain has been reported to catalyze the addition of D-amino acids to N-protected amino acid monomers;[30] however, the delivery of D-amino acids by an enzyme is relatively rare, and this chemistry catalyzed by trypsin remains, to the best of our knowledge, unexplored. Careful quantitation of the diastereomeric product yields and the rates at which they accumulate should be a measure of how distorted the trypsin active site is in organic solvent systems.

Addition of Amino Acid Hydrazides

In order to facilitate further chain elongation of the MP backbone to generate more elaborate models of heme proteins, we explored the addition of a group by reverse-proteolysis that will react in a chemoselective manner with readily accessed unprotected peptide derivatives. Hydrazido groups are known to readily form condensation products with aldehydes in buffered aqueous solutions. The reaction between the aldehyde and hydrazido moiety is relatively selective - the hydrazido group remains unprotonated and is a more potent nucleophile than peptide amino termini or lysine side chain amines at low pH's (4-5). This condensation has been exploited to link together unprotected

peptide segments; Vilaseca and coworkers delivered a carbohydrazide (H_2N-NH-C(O)-NH-NH_2) residue to a protein C terminus by reverse proteolysis and appended an aldehyde bearing peptide by hydrazone formation.[31] Our attempts to adapt these reaction conditions (aqueous DMSO solutions) to our system failed, and carbohydrazide is not readily soluble in DMF solutions. These discouraging results with carbohydrazide prompted us to search for an alternative group containing a hydrazido moiety. Fortunately, carbobenzyloxy (Z) -protected amino acid hydrazides are commercially available as TFA salts, and were readily incorporated into our reverse proteolysis methodology. Trypsin catalyzed reaction between MP9 and glycine carbobenzyloxyhydrazide (γ) proceeded to form γ23MP10 smoothly in good yields. Deprotection of the hydrazide, however, proved to be problematic, as catalytic hydrogenation over carbon supported palladium[32] resulted in decomposition of γ23MP10. Alternative deprotection schemes such as treatment with acetic acid/hydrobromic acid mixtures are available, however, and may be more successful than the hydrogenation route.

Intramolecular Ligand Binding in X23MP10's

UV-visible Spectroscopy

The electronic absorption spectrum of Fe(III) H23MP10 changes dramatically with pH (Figure 5.13). The green low pH form has an intense Soret band (λ_{max} 394 nm) that redshifts to 406 nm and loses intensity upon titration with base, giving the high pH form a deep red color. In the visible region, the low pH form has broad, relatively weak Q-bands that gain intensity and coalesce as the pH rises. A tight isosbestic point is present at 494 nm, indicating clean conversion (pK 4.4) between the two forms. This behavior differs markedly from that of the MP9 precursor, which exhibits complex pH-dependent solution chemistry, with a spin-state change at approximately pH 9.5 (Figure

Figure 5.13: Top: Dependence of the H23MP10 absorption spectrum on pH. The initial pH 1.7 solution was titrated with concentrated NaOH. Spectra were measured using an HP-8452A diode array spectrophotometer. Bottom: Titration curve plotting absorbance at 396 nm as a function of pH.

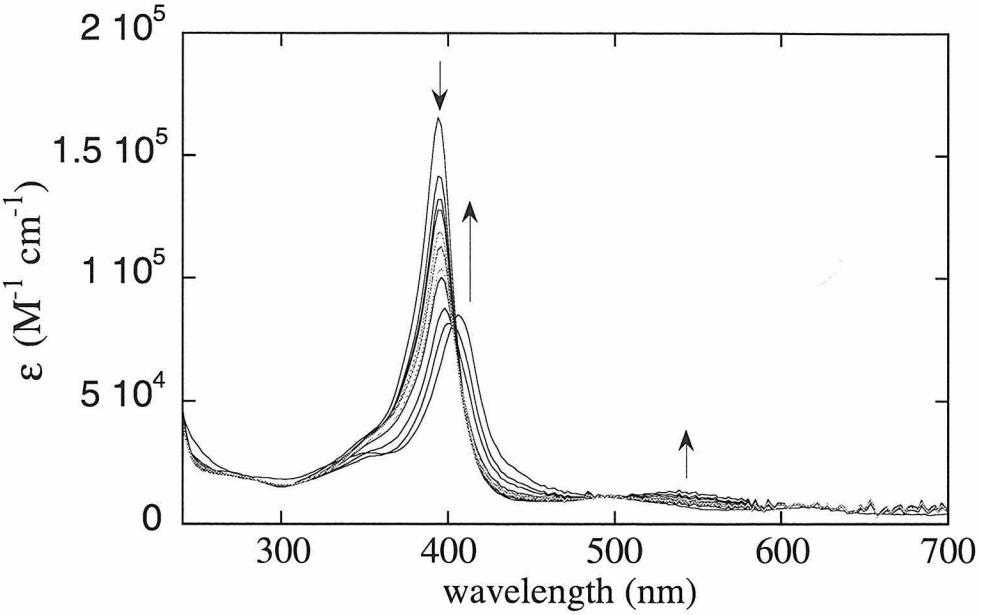
2 10^5
1.5 10^5
1 10^5
5 10^4
0
ε (M^-1 cm^-1)
300
400
500
600
700
wavelength (nm)

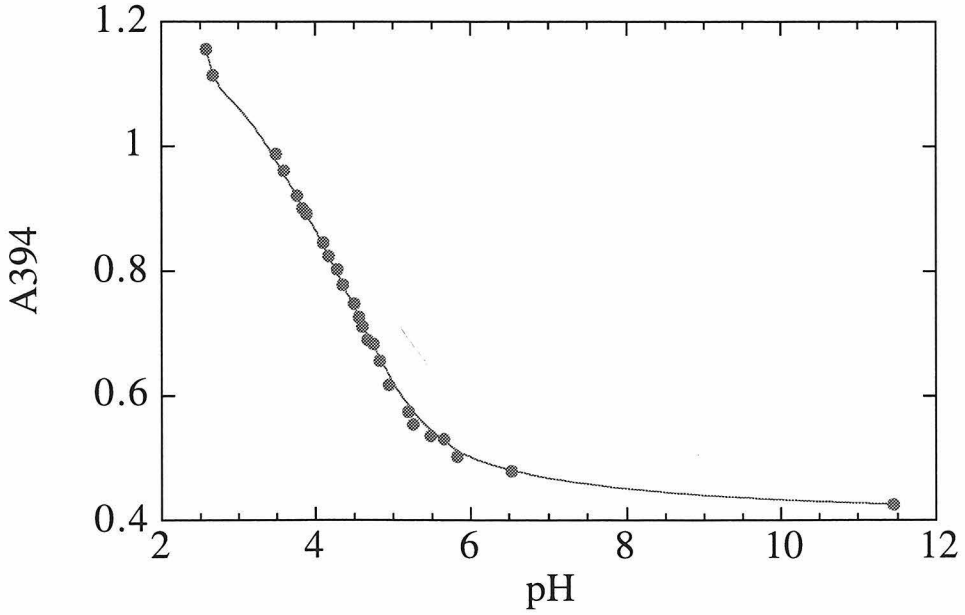
1.2
1
0.8
0.6
0.4
A394
2
4
6
8
10
12
pH

5.14). The spectra indicate that the imidazole of His23 binds axially to Fe(III) at high pH, producing a low-spin heme. The His23 imidazole is protonated at low pH, yielding a high-spin His-aquo heme. The X-band EPR spectrum of a frozen solution of H23MP10 (pH 2) shows a prominent g = 6 resonance characteristic of high-spin Fe(III) (Figure 5.15). The electronic absorption spectrum of the low-pH form is virtually identical with that of high-spin His-aquo MP8 (λ_{max} = 396 nm).[33] No EPR signal was detected from a frozen solution of H23MP10 at pH 7 at 77 K, consistent with the presence of a low-spin heme center. A Beer's law plot at pH 7 is linear in the μM concentration range (data not shown), and ^{1}H-NMR spectra are concentration independent over a tenfold concentration range (~0.1-1 mM) suggesting that the imidazole coordination is largely intramolecular in nature. Fe(III) Y23MP10 also undergoes a pH-dependent spin-state change and its absorption spectrum is characteristic of a low-spin form at pH 9. Fe(III) M23MP10, however, does not exhibit any spin-state changes other than those present in the MP9 precursor, indicating that the thioether side chain of Met23 does not coordinate to the ferric heme center (Figure 5.16). Interestingly, the thioether of M23MP10 apparently has little affinity for Fe(II); the UV-vis absorption spectrum of Fe(II) M23MP10 is virtually identical with that of reduced MP9 (Figure 5.17).

Resonance Raman Spectroscopy of X23 Microperoxidases

The large enhancements in scattering efficiency resulting from the intensity absorption bands associated with porphyrin π–π* transitions make heme proteins and their small molecule analogs ideal for investigation by resonance Raman spectroscopy. Our measurements were generally made with Soret region excitation (406 nm) to take full advantage of the resonance effect. Symmetrical modes of the porphyrin chromophore are selectively enhanced and dominate the Raman spectra obtained of heme proteins with Soret region excitation wavelengths. The positions of high-frequency (1300-1600 cm^{-1}) marker bands correlate with iron spin and oxidation states. The largest feature in the

Figure 5.14: Titration of MP9 with base monitored by UV-visible spectroscopy. Top: pH dependence of the absorption spectrum. Bottom: Titration curve based on the change in absorbance at 406 nm. Titration data collected by Grace Yang.

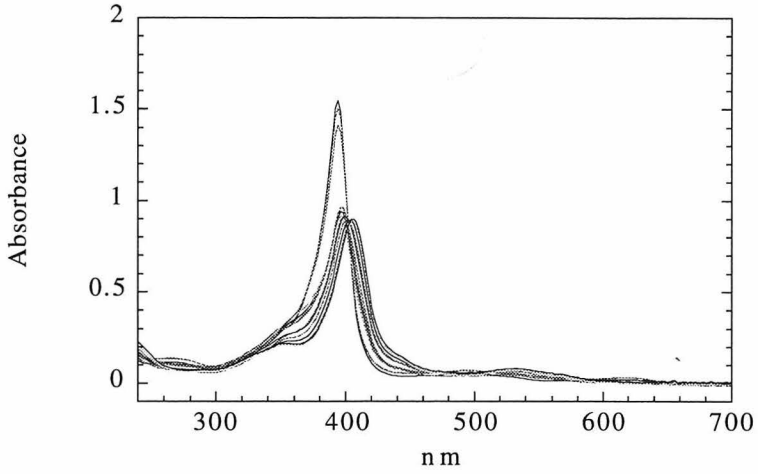
Absorbance
2
1.5
1
0.5
0
300
400
500
600
700
nm

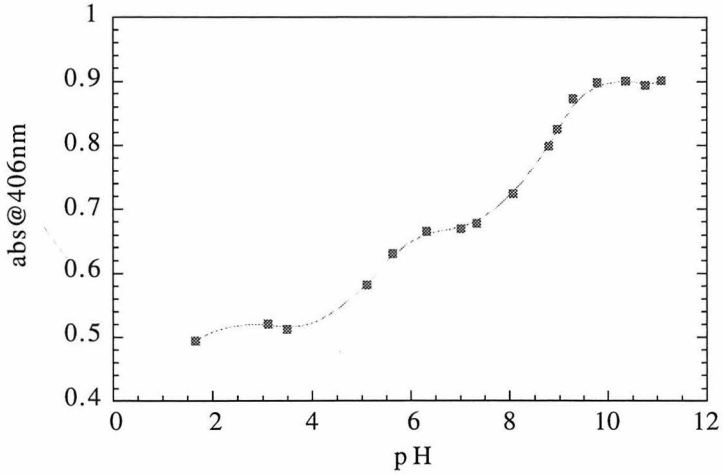
abs@406nm
1
0.9
0.8
0.7
0.6
0.5
0.4
0
2
4
6
8
10
12
pH

Figure 5.15: X-band EPR spectrum of the low-pH form of H23MP10. ca. 1 mM peptide concentration, frozen methanol / water glass. The spectrum has been corrected by subtracting a baseline signal from the cavity.

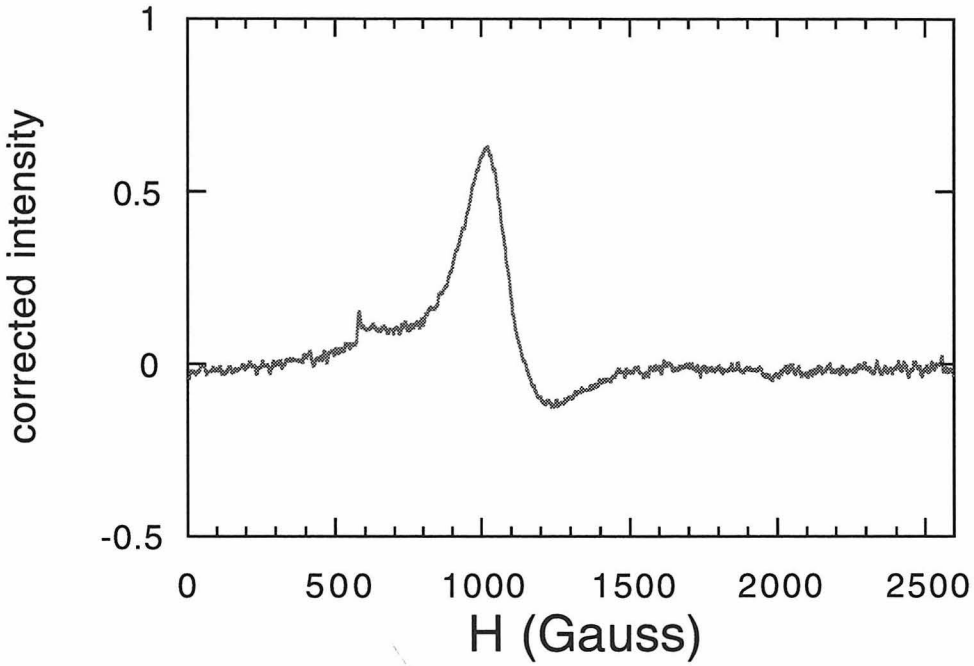
corrected intensity
1
0.5
0
-0.5
0
500
1000
1500
2000
2500
H (Gauss)

Figure 5.16: Titration of M23MP10 with base, starting at pH 2. Top: pH dependence of the optical spectrum. Bottom: Titration curve based on the change in absorbance at 406 nm. Titration data collected by Grace Yang.

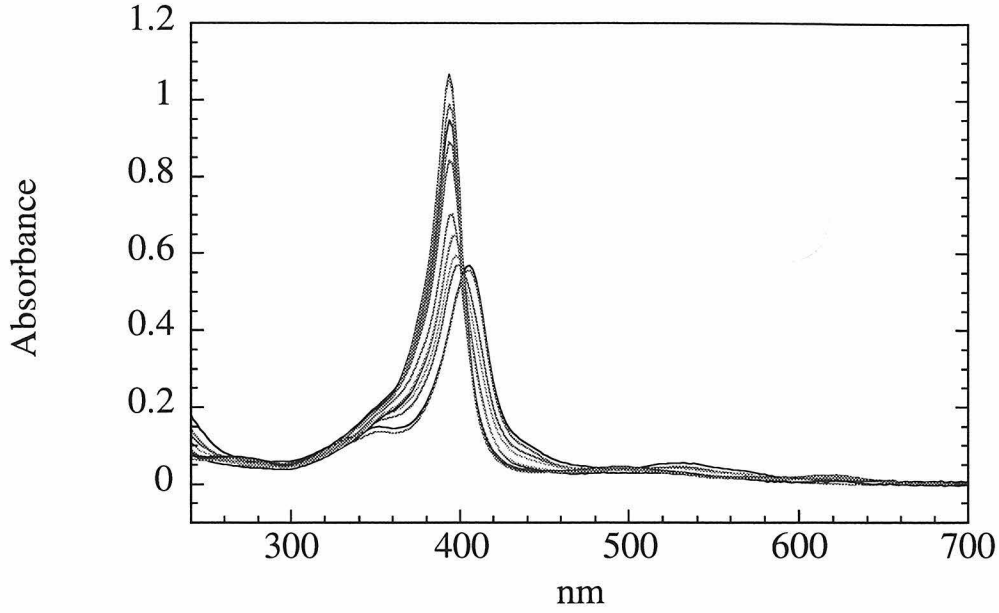
Absorbance
1.2
1
0.8
0.6
0.4
0.2
0
300
400
500
600
700
nm

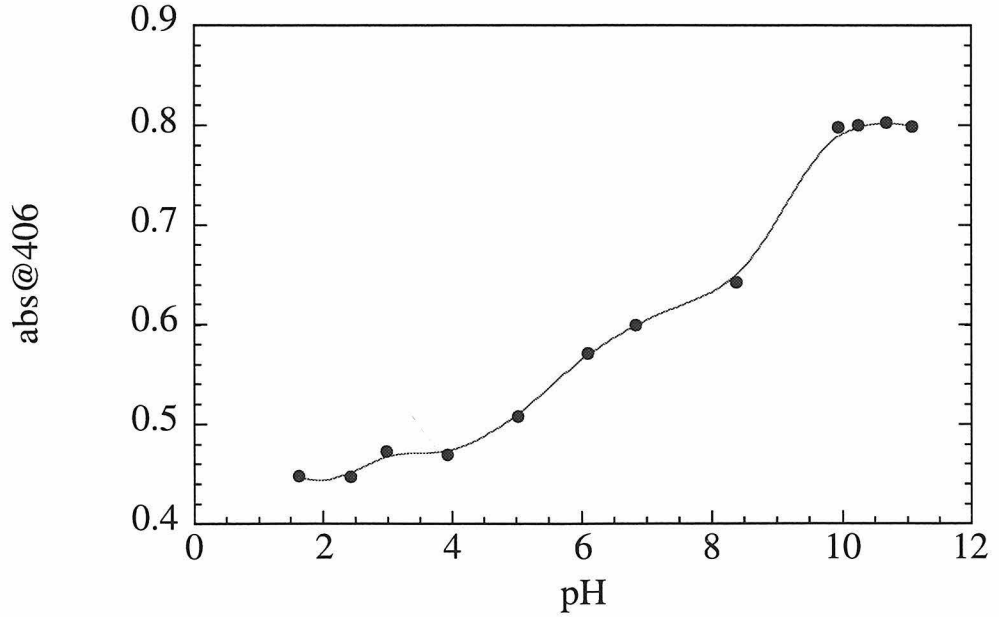
abs@406
0.9
0.8
0.7
0.6
0.5
0.4
0
2
4
6
8
10
12
pH

Figure 5.17: UV-visible spectra of reduced M23MP10 (dashed line), H23MP10 (dot-dash), Y23MP10 (dotted) and MP9 (solid). The relative intensities are not to scale.

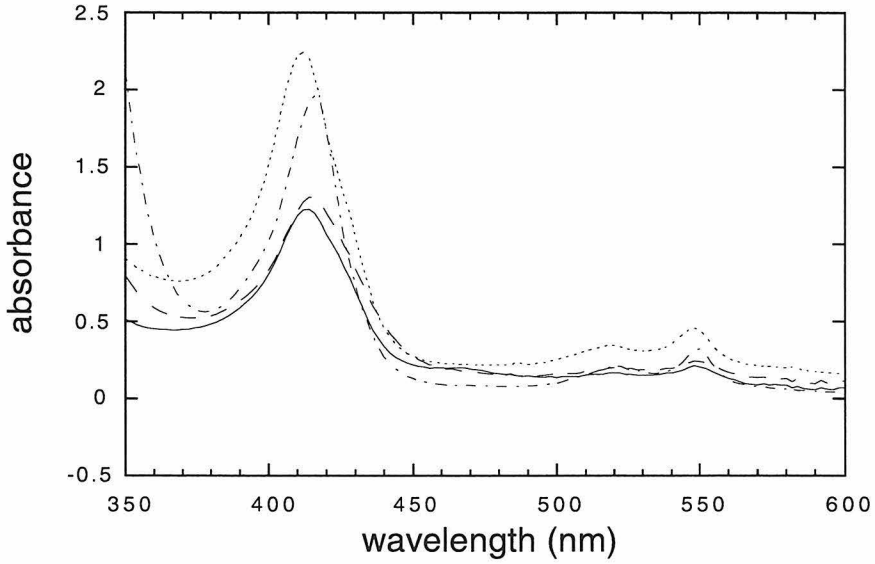
2.5
2
1.5
1
0.5
0
-0.5
absorbance
350
400
450
500
550
600
wavelength (nm)

high-frequency Raman spectra of iron porphyrins is the Cα-N symmetrical breathing mode ν_4 that appears near 1370 cm^{-1}. The position of this band correlates well to iron oxidation state as well as the presence of strong π acidic or basic ligands. Other prominent porphyrin bands in the high frequency range include ν_2, ν_4 and ν_{10}, each of which are useful spin-state markers. The frequencies of these modes are known to exhibit an inverse dependence on the core size of the porphyrin. Thus, high and low spin ferric and ferrous porphyrins are readily distinguished by comparison of their high-frequency resonance Raman spectra. We have applied resonance Raman spectroscopy here to investigate oxidation and spin state changes in the X23MP10 series.

The resonance Raman spectra of the Fe(III) forms of H23MP10 and Y23M10 have well-resolved porphyrin marker band regions. The high-frequency bands of H23MP10 (pH 7) (ν_4 = 1368, ν_2 = 1584, ν_{10} = 1633 cm^{-1}) (Figure 5.18) and Y23MP10 (pH 9) (ν_4 = 1368, ν_3 = 1501 ν_2 = 1581, ν_{10} = 1634 cm^{-1}) (Figure 5.19) resemble those of pure low-spin hemes, with marker band frequencies shifted to higher frequencies than the corresponding high spin hemes.[15,27,28] In contrast, the marker band region of the resonance Raman spectrum of MP8 at pH 7 (Figure 5.20) features broadened marker bands attributable to a heterogeneous mixture of heme chromophores with high and low-spin states.[16,17] As the pH is lowered to 2, the marker bands of Fe(III) H23MP10 undergo shifts to positions (ν_4 = 1366, ν_3 = 1482, ν_2 = 1567, ν_{10} = 1615 cm^{-1}) corresponding to a pure high-spin ferric center. Indeed, the spectrum closely resembles that of the His-aquo form of MP8 at pH 2 (ν_4 = 1367, ν_3 =1484 ν_2 = 1567, ν_{10} = 1617 cm^{-1}) (Figure 5.18), which appears to be predominantly high spin as determined by EPR, UV-vis, NMR and solution magnetic susceptibility measurements.[16,17]

In contrast to Soret region excitation, which selectively enhances symmetric modes of the porphyrin ring, Q-band excitation leads to selective enhancement of non-symmetrical modes that mix the B and Q states. Out of plane modes that are sensitive to porphyrin distortions are selectively enhanced in spectra with Q-band probe

Figure 5.18: Resonance Raman of H23MP10 at pH 7 and pH 2, high frequency region. Excitation at 406 nm, ~ 1.5 mJ / pulse at 10 Hz. 1 minute acquisition time, 2 mm slit height.

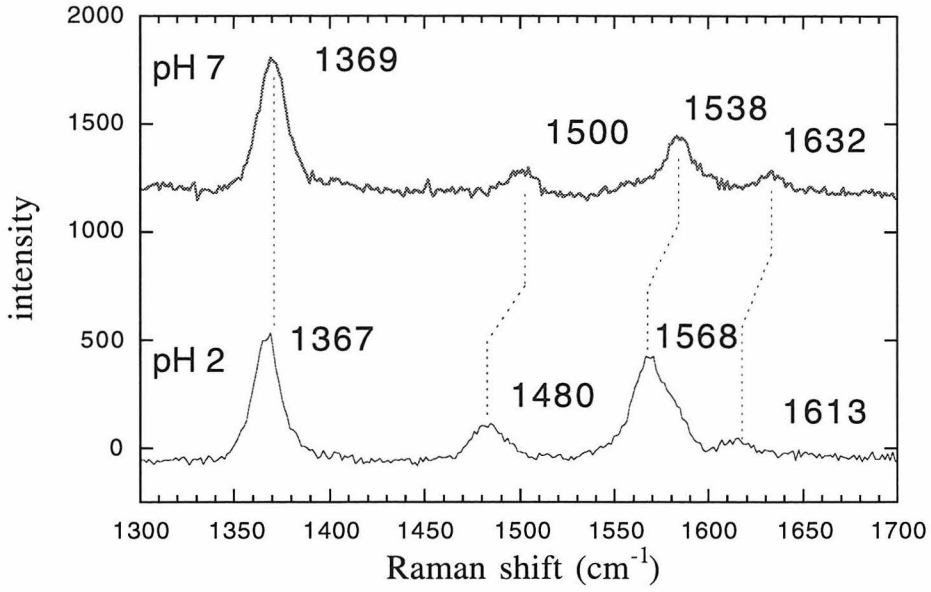
2000
1500
1000
500
0
intensity
pH 7
1369
1500
1538
1632
pH 2
1367
1480
1568
1613
1300
1350
1400
1450
1500
1550
1600
1650
1700
Raman shift (cm-1)

Figure 5.19: Resonance Raman spectrum of oxidized and reduced Y23MP10 in 0.1 M bicarbonate buffer, pH 9. Exposure time 60 s. 406 nm excitation.

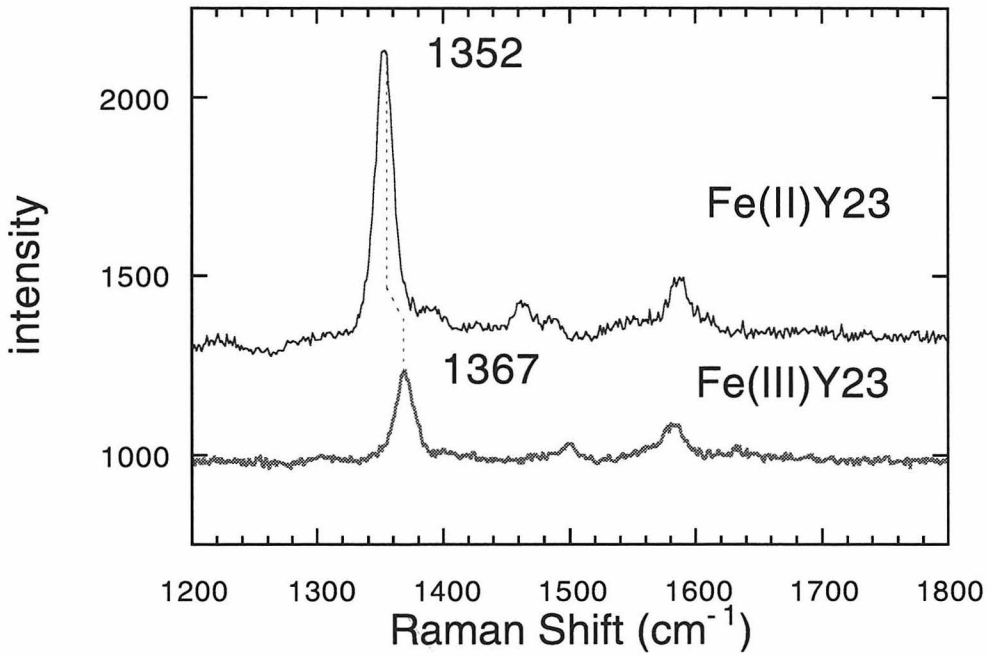
1352
2000
Fe(II)Y23
1500
1367
Fe(III)Y23
1000
intensity
1200
1300
1400
1500
1600
1700
1800
Raman Shift (cm-1)

Figure 5.20: Resonance Raman spectra of MP8 at pH 2 and pH 7, high frequency region. Excitation at 406 nm, ~ 1.5 mJ / pulse at 10 Hz. 1 minute acquisition time, 2 mm slit height.

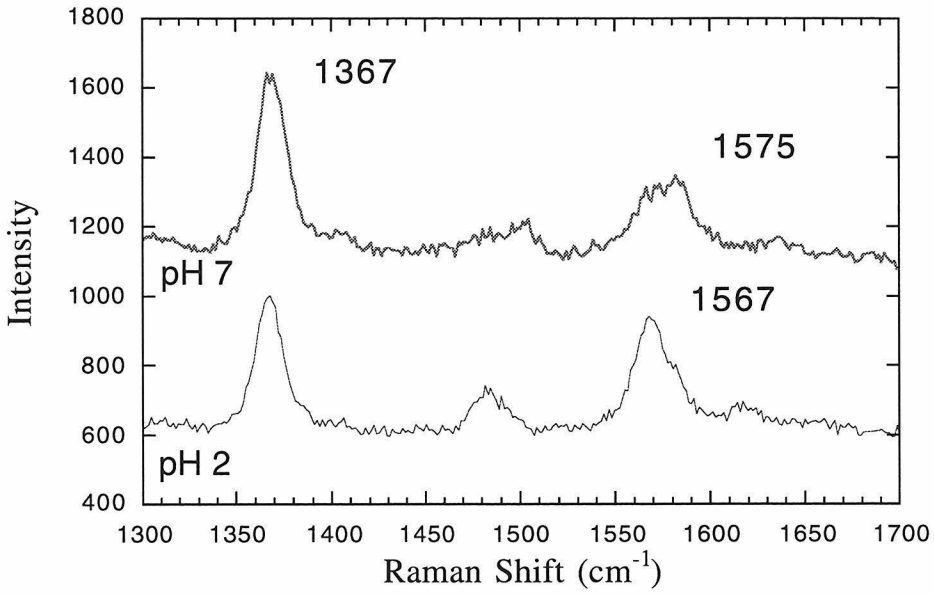
1800
1600
1400
1200
1000
800
600
400
Intensity
1367
1575
pH 7
1567
pH 2
1300
1350
1400
1450
1500
1550
1600
1650
1700
Raman Shift (cm-1)

wavelengths. We obtained reasonable resonance Raman spectra of H23MP10 with excitation in the Q-band region using the 532 nm line of a Nd-YAG laser. As expected, the high-frequency region of the spectrum is dominated by non-symmetric vibrational modes with moderate intensity (Figure 5.21). The low frequency region, however (< 1000 cm^{-1}), was found to be nearly featureless, suggesting that the MP10 porphyrin is relatively undistorted.

Addition of excess dithionite to argon-purged samples of Fe(III) H23 and Y23MP10 in pH 7 phosphate results in bright pink solutions of the corresponding Fe(II) forms. Spiro's inverse correlation between porphyrin vibrational frequencies and core size predicts a shift to lower frequency upon reduction, as the ferrous ion has a larger ionic radius, and should cause expansion of the porphyrin core. Indeed, resonance Raman spectra of Fe(II) H23 (Figure 5.22) and Y23MP10 (Figure 5.19) exhibit shifts in porphyrin marker frequencies consistent with the formation of low-spin ferrous heme centers.[14,15,27] The intense ν_4 oxidation state marker band shifts approximately 20 cm^{-1} to lower frequency upon reduction of both Y23 and H23MP10, appearing at 1351 cm^{-1}, with no detectable signal from unreacted Fe(III) species at 1368 cm^{-1}. The position of the spin-sensitive marker ν_2 at 1586 cm^{-1} in H23 and Y23MP10 suggests a six-coordinate Fe(II) in both cases.[14,15] The spectrum of Fe(II) Y23MP10 exhibits several moderately intense features in the low-frequency region that do not have counterparts in the spectrum of Fe(II) H23MP10; these features could indicate that there is a somewhat greater distortion of the porphyrin in Y23MP10.

Conclusions

The ability of trypsin to accept a wide variety of incoming nucleophiles should facilitate the synthesis of a wide variety of novel heme peptides. In the X23MP10 series (X = H, Y, M), the ligand-binding behavior provides a benchmark for evaluation of the

Figure 5.21: High-frequency resonance Raman Spectra of H23MP10 in pH 8.5 buffer with 532 nm excitation. A linear correction for baseline ramp was applied. The frequencies were determined using an uncorrected linear detector response function. Peak a: 1651 cm^{-1}; b: 1595 cm^{-1}, ν_{19}; c: 1405 cm^{-1}, ν_{20}; d: 1368 cm^{-1} $\nu_{15} + \nu_{24}$ or δ (CH_3); e: 1316 cm^{-1} ν_{21}.

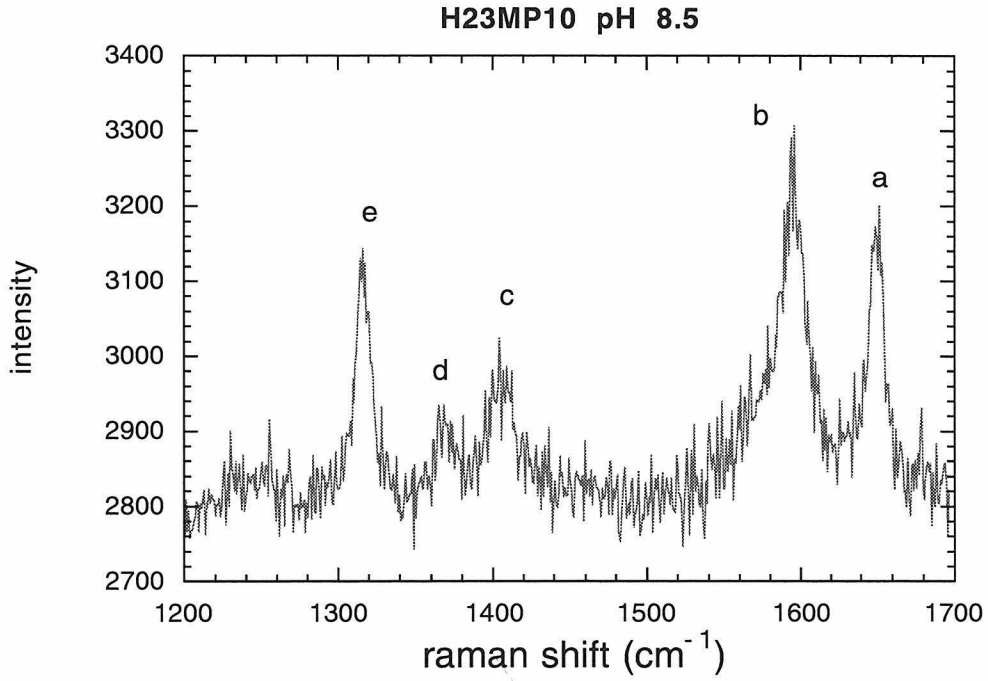
H23MP10 pH 8.5
intensity
3400
3300
3200
3100
3000
2900
2800
2700
1200
1300
1400
1500
1600
1700
raman shift (cm-1)
a
b
c
d
e

Figure 5.22: Resonance Raman spectra of dithionite reduced H23MP10, pH 7 (solid). Laser excitation at 406 nm, ~ 1.0 mJ/pulse at 50 Hz. For comparison, the resonance Raman spectrum of resting H23MP10 at pH 7 (dashed) is also shown (similar conditions, except 10 Hz repetition rate). Both samples are in 0.1 M phosphate buffer.

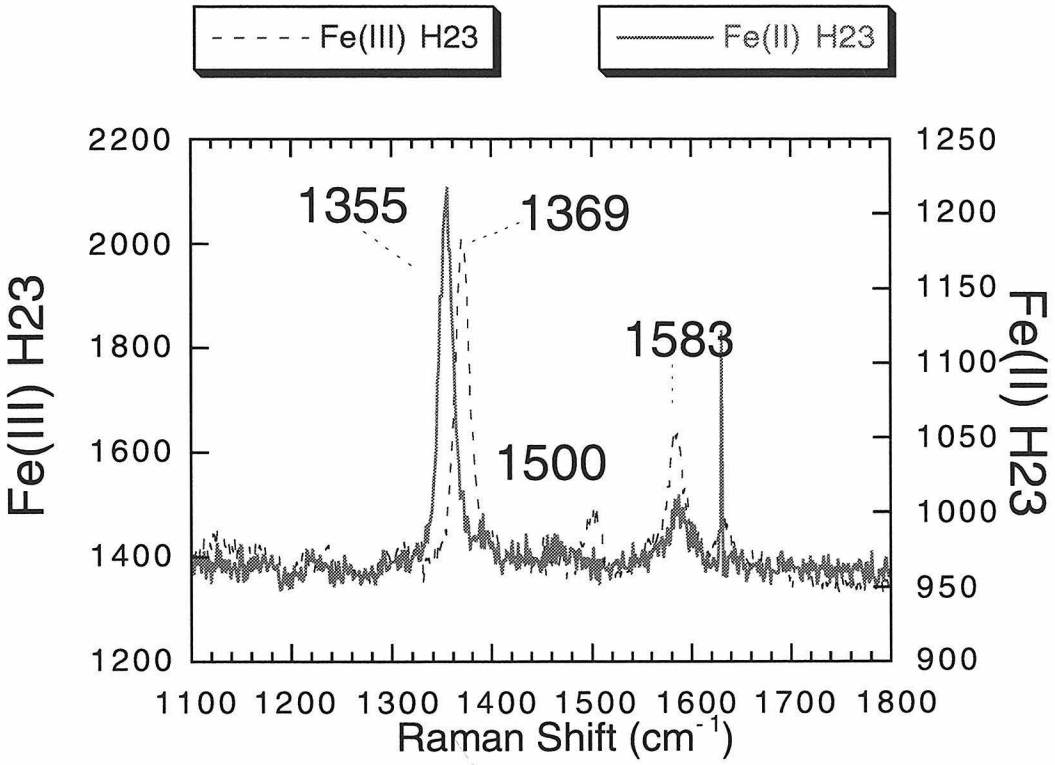
- - - - - Fe(III) H23
Fe(II) H23
2200
2000
1800
1600
1400
1200
1250
1200
1150
1100
1050
1000
950
900
1355
1369
1583
1500
Fe(III) H23
Fe(II) H23
1100 1200 1300 1400 1500 1600 1700 1800
Raman Shift (cm-1)

effects of folding on axial-ligand interactions in heme proteins; the histidine imidazole binds both Fe(III) and Fe(II) over a wide range of pH, tyrosine binding is seen only at high pH, and the thioether of methionine has very little affinity for Fe(III). In accord with observation,[34] our results suggest that histidine ligation will be favored in misfolded forms of cyt *c*. Although a tyrosine hydroxyl may be able to coordinate at high pH, it is unlikely that a methionine thioether will bind to Fe(III) in any unfolded state of the protein.

Apparently, trypsin has diminished specificity in its P_1' pocket in organic solvent mixtures, and is able to catalyze peptide bond formation to a variety of unusual peptide based substrates, including amino acids of unnatural chirality and protected amino acid hydrazides. The potential therefore exists to append selectively a wide variety of groups, such as metal chelators or fluorescent tags, onto heme peptide frameworks, and these may prove to be useful in further studies of electron transfer chemistry.

References and Notes

(1) Tsuchida, E.; Komatsu, T. *Meth. Enzym.* **1994**, *231*, 167-193.

(2) Momenteau, M.; Reed, C. A. *Chem. Rev.* **1994**, *94*, 659-698.

(3) Jameson, G. B.; Ibers, J. A. In *Bioinorganic Chemistry*; I. Bertini, H. B. Gray, S. J. Lippard and J. S. Valentine, Eds.; University Science Books: Mill Valley, 1994; pp 215-246.

(4) Boitrel, B.; Lecas-Nawrocka, A.; Rose, E. *Tet. Lett.* **1992**, *33*, 227-230.

(5) Battersby, A. R.; Howson, W.; Hamilton, A. D. *J. Chem. Soc., Chem. Commun.* **1982**, *21*, 227-230.

(6) Collman, J. P.; Brauman, J. I.; Iverson, B. L.; Sessler, J. L.; Morris, R. M.; Gibson, Q. H. *J. Am. Chem. Soc.* **1983**, *105*, 3052-3064.

(7) Traylor, T. G.; Berzinis, A. P. *J. Am. Chem. Soc.* **1980**, *102*, 2844-2846.

(8) Traylor, T. *Pure Appl. Chem.* **1991**, *63*, 265-274.

(9) Traylor, T. G. *Proc. Natl. Acad. Sci. U.S.A* .**1973**, *70*, 2647.

(10) Nishino, N.; Xu, M.; Mihara, H.; Fujimoto, T. *Chem. Lett.* **1992**, *2*, 327-330.

(11) Bongers, J.; Heimer, E. P. *Peptides* **1993**, *15*, 183-193.

(12) Peterson, J.; Saleem, M. M. M.; Silver, J.; Wilson, M. T. *J. Inorg. Biochem.* **1983**, *19*, 165-178.

(13) Munro, O. Q.; Marques, H. M. *Inorg. Chem.* **1996**, *35*, 3752-3767.

(14) Othman, S.; Lirzin, A. L.; Desbois, A. *Biochemistry* **1993**, *32*, 9781-9791.

(15) Othman, S.; Lirzin, A. L.; Desbois, A. *Biochemistry* **1994**, *33*, 15437-15448.

(16) Wang, J.-S.; Van Wart, H. E. *J. Phys. Chem.* **1989**, *93*, 7925-7931.

(17) Wang, J.-S.; Tsai, A.-L.; Heldt, J.; Palmer, G.; Van Wart, H. E. *J. Biol. Chem.* **1992**, *267*, 15310-15318.

(18) Smith, M.; McLendon, G. *J. Am. Chem. Soc.* **1981**, *103*, 4912-4921.

(19) Satterlee, J. D. *Inorg. Chim. Acta* **1983**, *79*, 195-196.

(20) Huang, Y.-P.; Kassner, R. *J. Am. Chem. Soc.* **1981**, *103*, 4927-4932.

(21) Adams, P. A.; Baldwin, D. A.; Marques, H. M. In *Cytochrome c : a multidisciplinary approach*; R. A. Scott and A. G. Mauk, Eds.; University Science Books: Sausalito, CA, 1996; pp 635-692.

(22) Carraway, A. D.; McCollum, M. G.; Peterson, J. *Inorg. Chem.* **1996**, *35*, 6885-6891.

(23) Schellenberger, V.; Jakubke, H.-D. *Angew. Chem. Int. Ed. Engl.* **1991**, *30*, 1437-1449.

(24) Kitaguchi, H.; Klibanov, A. M. *J. Am. Chem. Soc.* **1989**, *111*, 9272-9273.

(25) Sakina, K.; Kawazura, K.; Morihara, K. *Int. J. Peptide Protein Res.* **1988**, *31*, 245-252.

(26) Gill, I.; Lopez-Fandino, R.; Vulfson, E. *J. Am. Chem. Soc.* **1995**, *117*, 6175-6181.

(27) Breddam, K.; Widmer, F.; Meldal, M. *Int. J. Peptide Protein Res.* **1991**, *37*, 153-160.

(28) Bongers, J.; Offord, R. E.; Felix, A. M.; Campbell, R. M.; Heimer, E. P. *Int. J. Peptide Protein Res.* **1992**, *40*, 268-273.

(29) Berry, E. A.; Trumpower, B. L. *Anal. Biochem.* **1987**, *161*, 1-15.

(30) Barbas, C. F.; Wong, C.-H. *J. Chem. Soc. Chem. Commun.* **1987**, 533-534.

(31) Vilaseca, L. A.; Rose, K.; Werlen, R.; Meunier, A.; Offord, R. E.; Nichols, C. L.; Scott, W. L. *Bioconjugate Chem.* **1993**, *4*, 515-520.

(32) Hoffmann, K.; Magee, M. Z.; Lindenmann, A. *J. Am. Chem. Soc.* **1950**, *72*, 2814-2815.

(33) Aron, J.; Baldwin, D. A.; Marques, H. M.; Pratt, J. M.; Adams, P. A. *J. Inorg. Biochem.* **1986**, *27*, 227-243.

(34) Nall, B. T. In *Cytochrome c: a multidisciplinary approach*; R. A. Scott and A. G. Mauk, Eds.; University Science Books: Sausalito, CA, 1996; pp 167-200.

Chapter 6: Preparation, Spectroscopy and Electron Transfer Reactions of Manganese Microperoxidase-8

Introduction

In this Chapter, we briefly explore modification of the MP porphyrin by metal substitution. Since all of the first row transition metals from scandium through iron are known to form terminal metal-oxo complexes of varying stabilities, the opportunity exists to generate a series of metal-substituted MP8 complexes with which to study M(III)-OH --> M(IV)=O transformations over a wide range of driving forces and aquo pK's. The preparation of the free base porphyrin form of microperoxidase-8 (apo-MP8) and its subsequent metallation to produce the first member of this series, manganese substituted MP8 (MnMP8) are described. We will discuss some of the spectroscopic features of MnMP8, as well as its reactivity towards photo-generated $Ru(bpy)_3^{3+}$ and draw comparisons between our findings and the results of outer sphere oxidation of FeMP8 as well as with previous studies of oxidation of Mn substituted heme proteins by hydrogen peroxide.

Results and Discussion

Preparation and Characterization of apo-MP8 and MnMP8

The metal substitution of many heme proteins (for example, Mb) simply involves the removal of the native heme followed by reconstitution of the apo-protein with the appropriate metal-substituted porphyrin.[1,2] The covalent nature of the protein-heme linkage in *c*-type cytochromes, however, precludes this approach. An alternative method involves treatment of cyt *c* with anhydrous HF to produce porphyrin cyt *c*, which can then be reconstituted by treatment with the appropriate metal salt.[3] We have now adapted this procedure to also provide a convenient synthetic route to a variety of metal-substituted MP's.

Treatment of lyophilized solid MP8 with anhydrous HF at - 78° C results in the formation of a deep purple solution. After removal of the resulting iron fluoride salts from the resulting crude preparation by gel filtration chromatography in the dark, a purple solution of apo-MP8 is obtained. The optical spectrum of apo-MP8 has a very broad Soret band at 383 nm and 4 transitions in the visible region at 508, 542, 574 and 623 nm that are very characteristic of free base porphyrin spectra, and qualitatively similar to the absorption spectra reported for denatured porphyrin cytochrome *c* (Figure 6.1).[3-5] As expected, bright red emission is visible from solutions of apo-MP8 under ultraviolet irradiation.[5] The identity of apo-MP8 was confirmed by ^{232}Cf plasma-desorption mass spectrometry, which showed a parent ion peak at 1452 amu, along with features corresponding to the sodium adduct (M^+ + 23) and a 1409 amu fragment corresponding to a decarboxylation fragment (Figure 6.2). No residual unreacted FeMP8 was detected by mass spectrometry.

The crude reaction mixture that results from treating apo-MP8 with manganous acetate is a distinctive orange color, and an orange species constitutes the major band that elutes from reverse-phase chromatographic materials. The material comprising the major FPLC band was identified as the target MnMP8 by ^{232}Cf plasma-desorption mass spectrometry. Mn(III) porphyrins are commonly 6 coordinate, and thus we predicted that a water molecule would be coordinated to the Mn at the sixth axial position, resulting in a mass of 1506 amu. Indeed, a mass of 1507 amu was observed corresponding to the protonated aquo bound parent ion (Figure 6.2). The optical spectrum of purified MnMP8 has a distinctive "split Soret" band, with one component appearing at 368 nm and another weaker one at 463 nm (Figure 6.3). Split Soret spectra such as this are common to manganese(III) porphyrins, and are due to a lifting of the usual degeneracy between the porphyrin LUMO's due to π bonding with the manganese ion.[6,7] Table 6.1 lists the UV-vis spectral properties of a number of Mn substituted heme proteins.

Recent studies of the intermediate formed by reaction of Mn(III) porphyrins with peroxides favor a high-valent Mn(IV) oxo formulation (Mn(IV)=O) over the previously

Figure 6.1: Optical absorption spectrum of apo-MP8. The Q-band region (450 - 700 nm) is also shown enlarged 4 x to show detail.

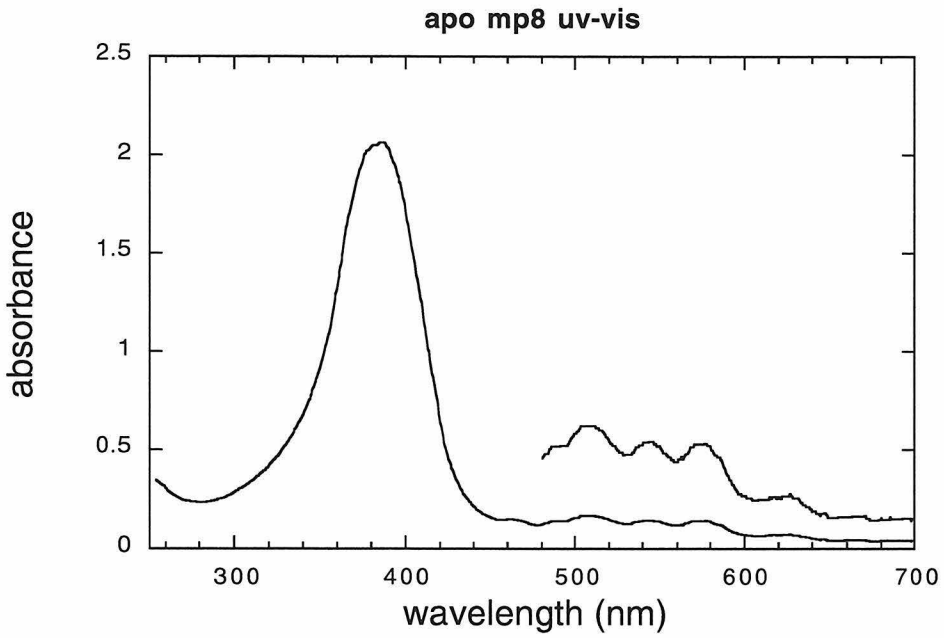
apo mp8 uv-vis
absorbance
2.5
2
1.5
1
0.5
0
300
400
500
600
700
wavelength (nm)

Figure 6.2: ^{232}Cf ion plasma desorption mass spectra of apo-MP8 (top: peak a, 1476 amu; peak b, 1452 amu ($M^+ + H^+$); peak c, 1409, 1406 amu) and MnMP8 (bottom: peak d, 1561 amu; peak e, 1507 amu ($M^+ + H^+$); peak f, 1463, 1457 amu).

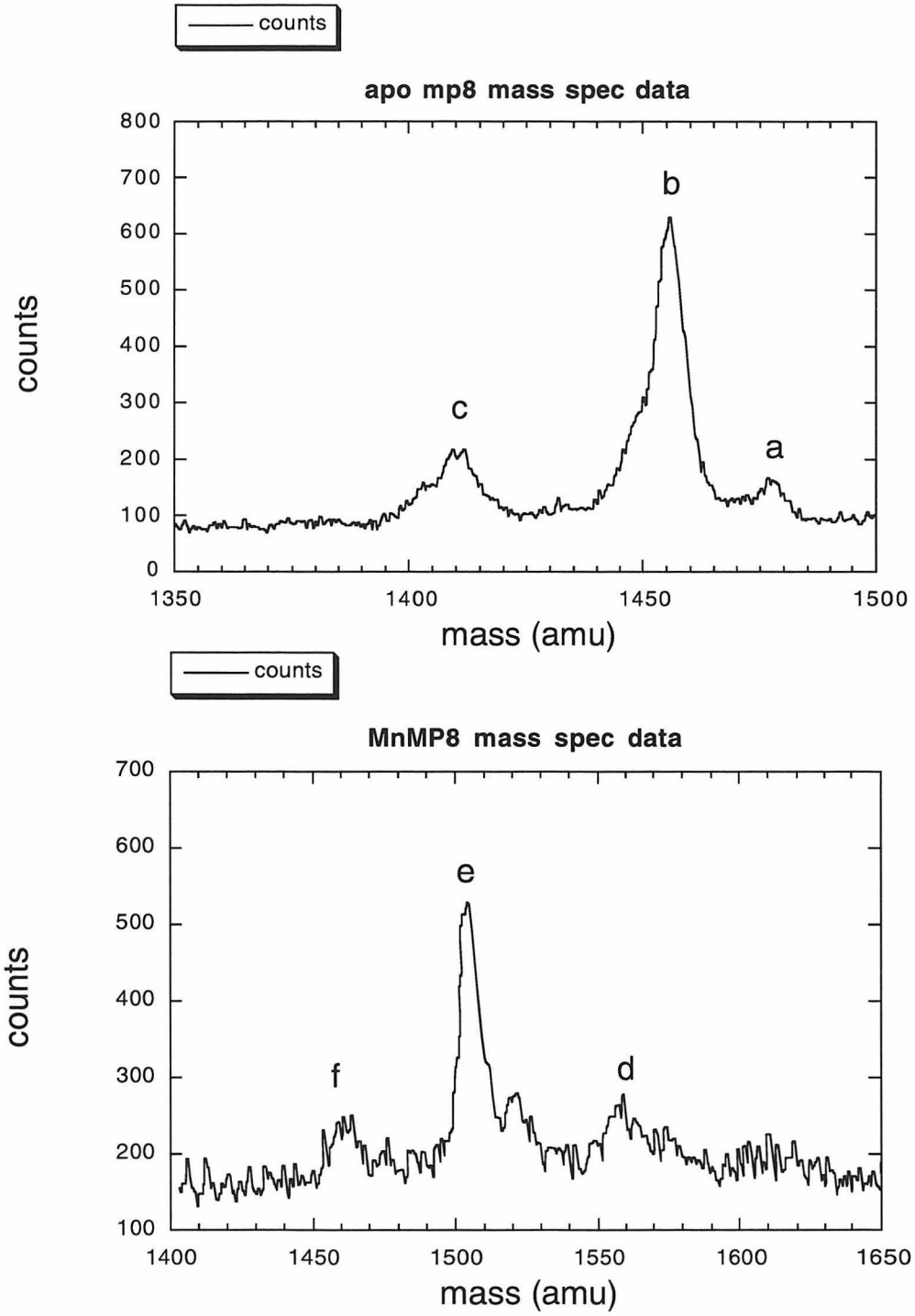
counts
apo mp8 mass spec data
800
700
600
500
400
300
200
100
0
counts
b
c
a
1350
1400
1450
1500
mass (amu)
counts
MnMP8 mass spec data
700
600
500
400
300
200
100
counts
e
f
d
1400
1450
1500
1550
1600
1650
mass (amu)

Figure 6.3: Optical absorption spectra of Mn(III) MP8 (dotted lines) and Mn(IV)=O MP8 (solid lines).

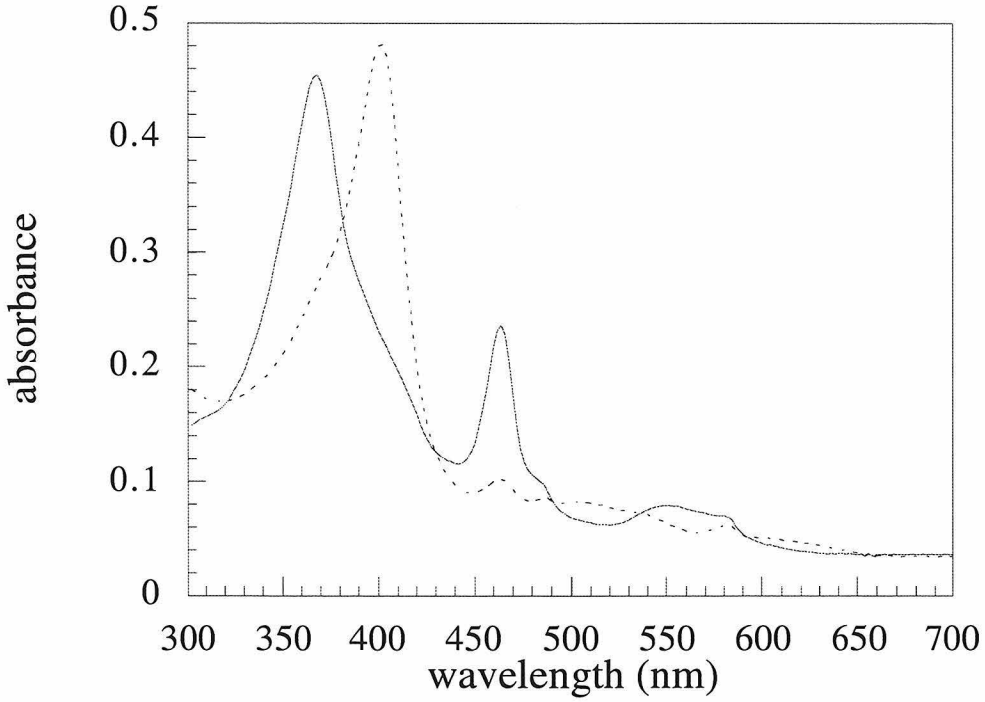
0.5
0.4
0.3
0.2
0.1
0
absorbance
300
350
400
450
500
550
600
650
700
wavelength (nm)

Table 6.1: UV-vis Absorption Maxima for Mn-Substituted Heme Proteins

Protein	Soret Component 1	Soret Component 2	Q - Bands
Mn(III) MP8	368	463	563
Mn(III) HRP	373	482	564
Mn(III) CcP	377	483	568
Mn(III) Mb	374	471	556

proposed Mn(IV) hydroxide complex (Mn(IV)-OH).[8] Treatment of Mn(III) MP8 with an excess of hydrogen peroxide generates a fleeting intermediate whose optical spectrum quickly reverts to that of the starting Mn(III) MP8 with little observed decomposition. The UV-vis spectrum of this intermediate has a single Soret band in a position between the two split Soret components at 401 nm (Figure 6.3). We assign this spectrum to that of the Mn(IV)=O MP8 in analogy to the oxidized form of Mn HRP, which has a single Soret band at 412 nm.[8,9] Addition of sodium dithionite to an anaerobic solution of Mn(III) MP8 yields, again, a species with a Soret band in the "normal" position, and we attribute this spectrum to the one-electron reduced form, Mn(II)MP8.

Photo-initiated Oxidation of Mn(III) MP8

In order to investigate the influence of metal coordination number and geometry on the reactivity of heme proteins towards peroxides, Mondal et al. measured the kinetics of hydrogen peroxide oxidation of Mn-substituted Mb.[10] This study proved to be useful for comparison with studies on the oxidation of Mn HRP by hydrogen peroxide, since it was unknown whether the difference in peroxidase activity between HRP and Mb could be attributed solely to the fact that ferric HRP has a five-coordinate heme active site, while met-Mb is six-coordinated. Since Mn Mb has a five-coordinate metal site,[11] metal substitution proved to be a simple way to introduce similar metal coordination environments within the different protein matrices. The observed rates for peroxide decomposition by the Mn substituted proteins were extremely slow compared to those of the wild-type proteins (Fe(III)HRP $k = 1.8 \times 10^7\ M^{-1}\ s^{-1}$, Fe(III)Mb $k = 1.3 \times 10^3\ M^{-1}\ s^{-1}$, Mn(III)HRP $k = 1.3 \times 10^4\ M^{-1}\ s^{-1}$, Mn(III)Mb $k = 2.5\ M^{-1}\ s^{-1}$).[10] Given these large difference in rates observed for reaction with the inner-sphere oxidant H_2O_2, we elected to investigate the relative rates of reaction between a homologous pair of Mn and Fe substituted MP's with an outer-sphere oxidant, photochemically generated $Ru(bpy)_3^{3+}$, in

order to determine whether the sluggish reactivity of the Mn substituted proteins is an intrinsic property of the Mn porphyrin center or is merely an artifact specific to the mechanism of peroxide decomposition by Mn porphyrins.

Laser flash photolysis of solutions of MnMP8 containing 10 μM $Ru(bpy)_3^{2+}$ and 10 mM $Ru(NH_3)_6^{3+}$ in neutral buffered solutions results in the appearance of a transient absorption spectrum that is in extremely excellent agreement with the difference spectrum calculated from peroxide oxidation of Mn(III) MP8 (Figure 6.4). The appearance of the Mn(IV)=O signal obeys first order kinetics, with typical rate pseudo-first order constants shown in Table 6.2. The slope of a plot of the MnMP8 concentration vs. the observed pseudo-first order rate constant yields the apparent bimolecular rate constant, shown in Table 6.3 and Figure 6.5. The rates remain roughly constant as a function of pH, although a somewhat higher rate was observed for oxidation in solution buffered at pH 8.5. This may indicate that we are approaching the pKa for the axially-bound water molecule; Mn porphyrin aquo complexes typically have pKa's ~ 1 unit lower than the analogous Fe porphyrins.[12] Since the aquo pKa of Fe(III) MP8 is known to be ~ 9,[13,14] it is reasonable that the analogous Mn(III) MP8 may contain significant quantities of manganese hydroxide species at pH 8.5. Unfortunately, the instability of $Ru(NH_3)_6^{3+}$ in pH 9 solution prevented further exploration of the pH dependence in the alkaline region. The observed bimolecular rates are quite similar to those observed for oxidation of Fe(III) MP8. The lack of pH dependence between pH 6 and 8 and the similar rates together suggest a mechanism for oxidation like the one observed for oxidation of Fe(III) MP8, in which bimolecular oxidation of the porphyrin ring precedes metal-oxo formation, and dominates the rate expression. We have not, however, directly observed the transient spectrum of the porphyrin radical as we did for FeMP8, and further transient absorption study is necessary on this point.

In spite of the fact that single-electron oxidation of Mn(III) MP8 should be somewhat less exothermic (ca. 100 mV) than the comparable oxidation of Fe(III) MP8, the

Figure 6.4: Top: Difference spectrum calculated from subtraction of the static UV-vis spectra of Mn(III) MP8 and Mn(IV)=O MP8. Bottom: Comparison of transient and static Mn(IV)=O - Mn(III) MP8 spectra; ΔOD values obtained from single exponential fits of kinetics traces (dots) superimposed on the static difference spectrum (solid line). ΔOD values from the laser experiment were obtained using traces with a 500 μs time base.

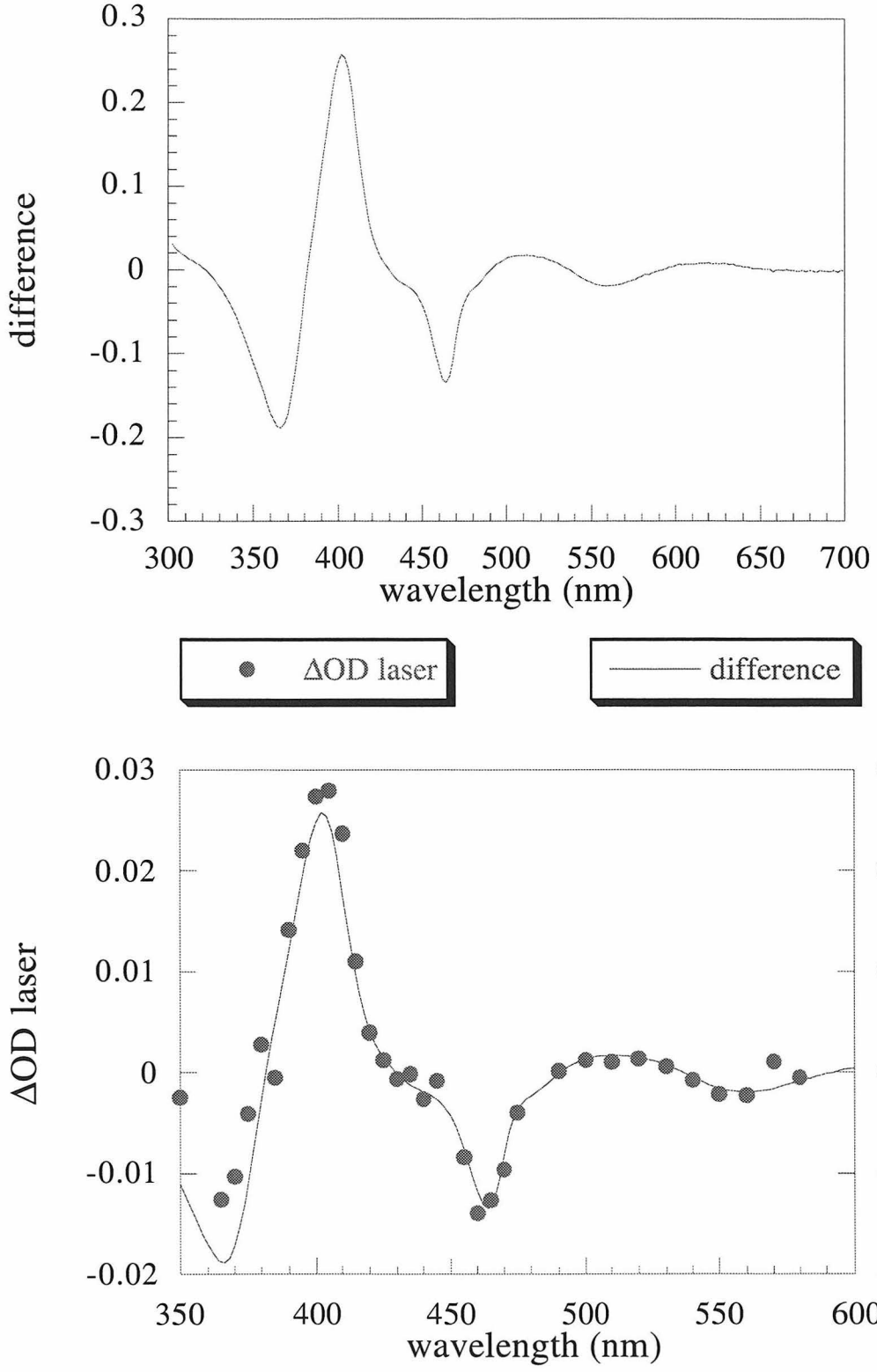
0.3
0.2
0.1
0
-0.1
-0.2
-0.3
difference
300 350 400 450 500 550 600 650 700
wavelength (nm)
ΔOD laser
difference
0.03
0.02
0.01
0
-0.01
-0.02
ΔOD laser
0.3
0.2
0.1
0
-0.1
-0.2
difference
350 400 450 500 550 600
wavelength (nm)

Figure 6.5: Plot of observed pseudo-first order rate constants as a function of MnMP8 concentration at pH 6, 7, 8 and 8.5. Lines are best fits from least-squares fitting.

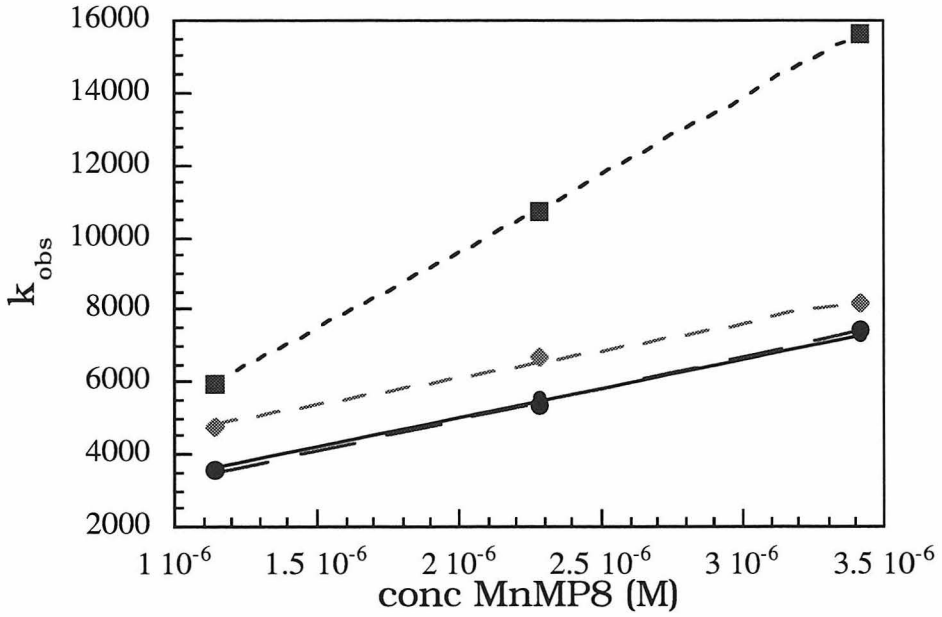
16000
14000
12000
10000
8000
6000
4000
2000
k_{obs}
1 10^{-6}
1.5 10^{-6}
2 10^{-6}
2.5 10^{-6}
3 10^{-6}
3.5 10^{-6}
conc MnMP8 (M)

Table 6.2: Observed Pseudo-First Order Rate Constants (s^{-1}) for Oxidation of Mn(III) MP8 by Photo-generated $Ru(bpy)_3^{3+}$ at pH 6-8.5

[Mn] (μM)	pH 6	pH 7	pH 8	pH 8.5
1.14	3645.0	3566.0	4725.0	5953.0
2.24	5554.0	5359.0	6690.0	10710
3.26	7291.0	7459.0	8175.0	15660

Table 6.3: Apparent Bimolecular Rate Constants for Oxidation of Mn(III) MP8 by Photo-Generated $Ru(bpy)_3^{3+}$

pH	k_{obs} (M^{-1} s^{-1})
6	1.7×10^9
7	1.8×10^9
8	1.6×10^9
8.5	4.6×10^9

presence of the Mn(III) ion does not seem to significantly impair the rates of reaction here, indicating that the Mn(III) center is readily oxidizable at high rates (comparable to the bimolecular rates observed for peroxide oxidation of the native peroxidase enzymes). This suggests that the Mn(III) centers of heme proteins are inherently less reactive towards oxidation by peroxides, but not because of the instability of the Mn(IV)=O moiety. The low reactivity may be due either to a reduced affinity for binding peroxide at the Mn(III) center, or perhaps due to the unusual stability of Mn(III) peroxo porphyrin complexes; certain complexes of Mn(III) porphyrins in which the peroxo ligand is bonded in a side-on fashion are relatively stable, as evidenced by the X-ray crystal structure of (TMP)FeO_2.[7] It may be that Mn porphyrins are relatively inefficient at cleaving the peroxide O-O bond. This could possibly be due to a weakening of the axial ligand interactions due to the presence of the Mn ion. Indeed, the axial metal-imidazole stretch measured in Mn(II) Mb is shifted to significantly lower frequency,[15] indicating that even in the Mn(II) form, axial bonding is weaker than in the analogous Fe(II) form, and although Raman measurements are not available for the corresponding Mn(III) form, JT distortion effects are likely to further weaken the axial bonding in this form. The diminished axial ligand interactions reduce the electron donor effectiveness of the proximal histidine, and could reduce the amount of "push" it supplies. Finally, it is interesting to note that there are manganese analogs of Fe-containing superoxide dismutases (SOD) and catalases, but there are no manganese containing peroxidase enzymes. Moreover, only Mn SOD has a mononuclear active site; Mn catalases all contain a binuclear bridged manganese core that is responsible for peroxide reactivity.

Conclusion

Demetallation of Fe(III) MP8 by anhydrous HF results in apo-MP8, which is a convenient starting material for a wide variety of metal-substituted MP8 derivatives,

including MnMP8. The identity of MnMP8 produced by treatment of apo-MP8 with manganous acetate was confirmed by mass spectrometry and UV-visible absorption spectroscopy. Spectroscopic results show that the resting state of MnMP8 contains a Mn(III) ion with histidine and aquo axial ligands. The Mn(IV)=O form of MP8 is readily prepared by oxidation with photo-generated $Ru(bpy)_3^{3+}$. The observed bimolecular rate constants for reaction with $Ru(bpy)_3^{3+}$ are comparable to those observed with FeMP8, and may suggest a common mechanism for their oxidations. The facile oxidation of the metal center by $Ru(bpy)_3^{3+}$ also suggest that a kinetic barrier to peroxide decomposition is responsible for the low peroxidase reactivity of Mn substituted heme proteins.

Experimental Section

Lyophilized MP8 was placed in the Teflon reaction container for the HF line used in the Biopolymer Center in the Beckman Institute. The reaction container was attached to the line and cooled with a dry-ice acetone bath. Enough HF was condensed into the reaction vessel to cover the solid MP. A purple solution results immediately. The HF solution was allowed to stand for 5 minutes at dry-ice temperature, and then allowed to warm to room temperature, after which time the HF was removed in vacuo. A brownish-purple residue remained in the vessel. The residue was treated with 0.1 M ammonium acetate buffer, pH 5, resulting in a purple solution, which was passed down either a Sephadex G-10 or G-25 (Pharmacia) column, which removed the iron salts from the free base solution. Care was taken to minimize the exposure of the free base to light, as many free base porphyrins are light-sensitive. Gel-filtered solutions of apo-MP8 were used immediately for metallation reactions by addition of manganous acetate (Aldrich) to give a roughly 10 mM solution. The metallation reaction was warmed to 40° C in a water bath and allowed to stand for 2 hours, then removed and allowed to stand in the dark for 2 days. The progress of the Mn insertion was monitored by UV-vis. After two days, the crude reaction mixture was

washed with 0.1% TFA and concentrated in an Amicon stirred cell. The concentrated crude mixture was fractionated on a Pharmacia PepRPC column using the standard FPLC protocol outlined in Chapter 2, using a 2.5 mL/min flow rate. The major orange fraction was collected and analyzed by mass spectrometry and UV-visible measurements. ^{232}Cf plasma desorption mass spectra were done by Jane Saunders in the Biology Department.

References

(1) Casimiro, D. R. Ph. D. Thesis, California Institute of Technology, 1993.

(2) Yonetani, T. J. *J. Biol. Chem.* **1967**, *242*, 5008.

(3) Erecinska, M.; Vanderkooi, J. M. *Meth. Enzym.* 165-181.

(4) Gouterman, M. *J. Mol. Spec.* **1961**, *6*, 138-163.

(5) Strottmann, J. M.; Stellwagen, A.; Bryant, C.; Stellwagen, E. *J. Biol. Chem.* **1984**, *259*, 6931-6936.

(6) Boucher, L. J. *J. Am. Chem. Soc.* **1968**, *90*, 6640-6645.

(7) VanAtta, R. B.; Strouse, C. E.; Hanson, L. K.; Valentine, J. S. *J. Am. Chem. Soc.* **1987**, *109*, 1425-1434.

(8) Nick, R. J.; Ray, G. B.; Fish, K. M.; Spiro, R. G.; Groves, J. T. *J. Am. Chem. Soc.* **1991**, *113*, 1838-1840.

(9) Yonetani, T.; Asakura, T. *J. Biol. Chem.* **1969**, *244*, 4580-4588.

(10) Mondal, M. S.; Mazumdar, S.; Mitra, S. *Inorg. Chem.* **1993**, *32*, 5362-5367.

(11) Saxena, A.; Modi, S.; Behere, D. V.; Mitra, S. *Biochim. Biophys. Acta* **1990**, *1041*, 83-93.

(12) Kaaret, T. W.; Zhang, G.-H.; Bruice, T. C. *J. Am. Chem. Soc.* **1991**, *113*, 4652-4656.

(13) Baldwin, D. A.; Marques, H. M.; Pratt, J. M. *J. Inorg. Biochem.* **1986**, *27*, 245-254.

(14) Wang, J.-S.; Tsai, A.-L.; Heldt, J.; Palmer, G.; Van Wart, H. E. *J. Biol. Chem.* **1992**, *267*, 15310-15318.

(15) Parthasarathi, N.; Spiro, T. G. *Inorg. Chem.* **1987**, *26*, 3792-3796.

Chapter 7: Resonance Raman Studies of Ferrous Carbonmonoxy Microperoxidase-8 and Cytochrome c

Introduction

Optical triggering methods hold great promise for investigations of protein folding reactions on sub-millisecond time scales. We and others have been exploring the folding of cyt *c* using pulsed laser excitation to initiate folding.[1-3] In principle, given an appropriate system, events on time scales as short as the picosecond regime may be probed. Photoinduced injection of an electron into unfolded oxidized cyt *c* has been demonstrated by Pascher and coworkers to be a viable approach to rapid initiation of cyt *c* folding.[1] Jones and coworkers have developed a system that relies on laser-initiated photodissociation of a carbon monoxide ligand bound to denatured cyt *c* to initiate folding.[2] Both studies employed nanosecond transient absorption spectroscopy to monitor the progress of the folding reaction. Currently we are seeking additional methods to probe the nature of photo-induced folding reactions of cyt *c*, including time-resolved resonance Raman spectroscopy. Resonance Raman spectroscopy has been used extensively to characterize heme proteins, yielding information regarding the spin and oxidation state of the heme iron,[4,5] and the Raman spectra of *c*-type cytochromes are well-understood.[6-8] Time-resolved Raman is therefore a useful probe of dynamic structural changes in heme proteins,[9] and has already found application for the study of oxidized cyt *c* folding.[10] For technical reasons, we have opted to focus our initial efforts on obtaining time resolved Raman spectra of cyt *c* folding reactions triggered by the CO photolysis method.

The photoinduced loss of a carbonyl ligand from metal centers is one of the most studied reactions of inorganic photochemistry.[11] In the presence of appropriate axial ligands, ferrous iron porphyrins avidly bind carbon monoxide, and photolysis of the carbonmonoxy complex readily causes dissociation of the carbonyl ligand. In general, the photodissociation of CO from hemes is highly reversible, and occurs with near-unit quantum yield with excitation wavelengths over a wide range. Nearly all aspects of CO photodissociation from heme proteins and models have been scrutinized by a battery of

time resolved methods, including UV-vis,[12,13] IR,[14] Raman,[15] and X-ray crystallography.[16] Departure of the CO ligand from the iron following photolysis is extremely rapid (≤ 350 fs).[13] The bimolecular recombination rate for CO recombination has been reported to be approximately 2 x 10^7 M^{-1} s^{-1} for the fully solvent exposed heme of MP-11.[17] Slower recombination rates are observed for the buried active sites of heme proteins.[18] The ultrafast dissociation and relatively slow recombination kinetics make for a reasonable, reversible optical trigger for protein folding.

The CO photolysis method used by Jones et al. takes advantage of Fe(II) cyt *c*'s affinity for CO at elevated temperatures in the presence of denaturants. The presence of CO was found to stabilize the unfolded form of Fe(II) cyt *c*, (Fe(II) cyt c_f) that is, the protein unfolds at lower concentrations of denaturant (guanadinium hydrochloride, GdnHCl) in the presence of CO. Laser photolysis resulting in photodissociation of the CO ligand, in principle, could then initiate cyt *c* folding within a certain denaturant concentration regime (for h-cyt *c*, the range is ~ 3-6 M GdnHCl). Indeed, Jones and coworkers observe changes in the UV-visible absorption spectrum after photolysis that were attributed to loss of the carbonyl ligand to initially generate a five-coordinate heme species akin to deoxy-Mb within the unfolded protein matrix. Subsequent to CO loss, the UV-visible spectrum continued to evolve and these changes were attributed to partial folding of the cyt *c* protein in competition with CO rebinding.[2]

In order to further investigate the behavior of unfolded cyt *c* after photodissociation of CO, we have elected to apply microsecond time-resolved resonance Raman as a probe of events occurring exclusively at the heme center. Observation of high-frequency marker bands as a function of time following CO photodissociation should allow direct observation of the high-spin five-coordinate heme, as well as its subsequent transformation into low-spin six-coordinate species. In order to effectively isolate the folding of the protein matrix from events that occur at the heme, we have prepared the ferrous carbonmonoxy form of MP8 (Fe(II)-CO MP8) and examined its photochemistry by transient absorption and time-

resolved resonance Raman methods. Fe(II)-CO MP8 is an ideal model for unfolded ferrous carbonmonoxy cyt *c* (Fe(II)-CO cyt c_u), as it has the identical heme substitution pattern and axial ligation (important for direct comparisons of heme vibrational modes), but time-resolved spectra of the MP8 model system will be free of changes due to the folding of the protein.

Results and Discussion

Static Raman and UV-visible Spectroscopy of Fe(II)-CO MP8 and cyt *c*

Dithionite reduction of MP8 in buffered aqueous solution saturated with CO results in a bright pink solution of Fe(II)-CO MP8. There are relatively few reports of the preparation of Fe(II)-CO MP8, however, the optical spectrum obtained here is qualitatively similar to that of Fe(II)-CO MP11 reported by Sharma et al.[19] The UV-vis absorption spectrum of Fe(II)-CO MP8 features an extremely narrow, intense, red-shifted Soret band typical of Fe(II)-CO hemes (λ_{max} = 412 nm, ε = 200 mM^{-1} cm^{-1}, Figure 7.1).[20] The static resonance Raman spectrum of this species (406 nm excitation) is similar to other ferrous carbonmonoxy hemes,[21] with an extremely intense ν_4 band at 1365 cm^{-1}, consistent with the presence of a strong π-acceptor ligand on the ferrous center (Figure 7.2).[22] Reduction of the ferric MP8 and its conversion to Fe(II)-CO MP8 appears to be quantitative, as there is no indication in the Raman spectra of any residual ferric MP8. A small shoulder appears on the short wavelength side of ν_4 indicating a small amount of photodissociation results from 406 nm excitation. The prominent band at 680 cm^{-1} is likely to be due to a C-S stretching mode (ν_{C-S}) associated with the thioether groups.[7] The addition of 4.6 M GdnHCl to the solution does not significantly perturb the Raman spectrum of Fe(II)-CO MP8: (ν_4 = 1365, ν_2 = 1585, ν_{C-S} = 683 cm^{-1}). The static resonance Raman spectrum of Fe(II)-CO cyt c_u in 4.6 M GdnHCl at 40° C is very similar

Figure 7.1: UV-visible absorption spectra of ferric (dotted line) and ferrous carbonmonoxy forms of MP8 (solid line) in 0.1 M phosphate buffer, pH 8. Extinction coefficients for Fe(II)-CO MP8 were calculated using an extinction coefficient $\varepsilon = 154$ mM^{-1} cm^{-1} for ferric MP8 assuming complete conversion to the Fe(II)-CO form.

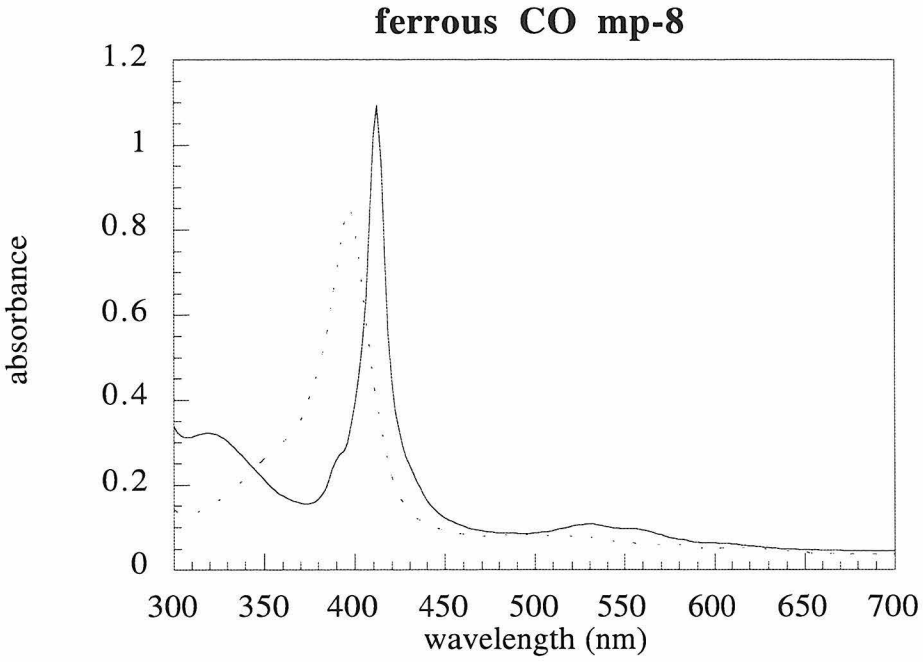
ferrous CO mp-8
absorbance
1.2
1
0.8
0.6
0.4
0.2
0
300
350
400
450
500
550
600
650
700
wavelength (nm)

Figure 7.2: Static resonance Raman spectrum of Fe(II)-CO MP8. 406 nm excitation, 60 s exposure time, 20 Hz repetition rate.

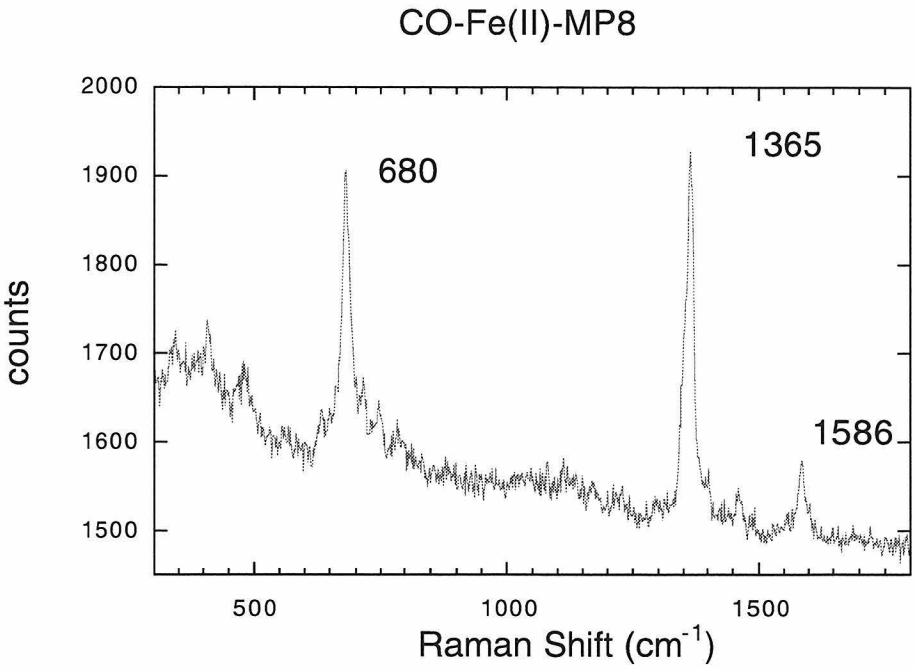
CO-Fe(II)-MP8
2000
1900
1800
1700
1600
1500
counts
680
1365
1586
500
1000
1500
Raman Shift (cm-1)

to that of Fe(II)-CO MP8, with ν_2 at 1366 cm^{-1} and an intense feature at 682 cm^{-1}.* For further reference points, static resonance Raman spectra were also collected of h-cyt *c* in oxidized and reduced, folded and unfolded forms.**

The resonance Raman spectrum of folded y-cyt *c* has been extensively assigned with the aid of isotopically labeled hemes.[7] The low frequency region of the spectrum features a large number of modes assigned to out of plane vibrations that are activated by the propeller-shaped distortion of the heme observed in the X-ray crystal structure of folded cyt *c*.[8] The resonance Raman of the partially acid denatured "A-state" of ferric cytochrome *c* has also been examined by resonance Raman methods.[23] Analysis of the high frequency marker region clearly demonstrates the presence of both high and low spin forms. The low frequency out of plane modes present in the folded protein are largely absent in the A-state, indicating a loss of heme distortion due to protein contacts as a result of the partial denaturation. These out of plane modes may therefore be useful indicators of cyt *c* folding.

Time-Resolved Measurements

Time-resolved resonance Raman spectra were collected using a pump-probe method in which the time-resolution is determined by a delay between the arrival of the pump and probe pulses at the sample. Superior results were obtained when 532 nm pulses were used, as shorter wavelength pump pulses (355 nm) appeared to result in fluorescence associated with the protein that causes severe baseline offsets. Time-resolved Raman measurements of Fe(II)-CO MP8 clearly show the formation of a deoxy-Mb like spectrum immediately after the pump pulse. The largest changes observed are in the ν_4 band, which shifts from 1366 cm^{-1} in the static spectrum to 1352 cm^{-1} in the transient spectrum. The

---

* The intensity of the 682 cm^{-1} feature was variable from sample to sample and may be related to the concentration of denaturant.

** While the trends in band position between oxidized and reduced agree well with other published studies, the presice positions of our bands differ systematically from those found by Spiro by an average of 5 cm^{-1}.

time evolution of the MP8 ν_4 and ν_3 bands is shown in Figure 7.3. The results are very similar to those observed for the photolysis of carbonmonoxy Hb and Mb.[15,24] The 1366 cm^{-1} band grows back in as the CO rebinds to the heme and the transient spectrum resembles the static spectrum at t = 5 ms. This is in good agreement with transient absorption spectra taken of Fe(II)-CO MP8 following flash-photolysis that indicated a large degree of CO recombination by 1 ms (estimated > 80%, Figure 7.4).

A series of time-resolved Raman spectra were then collected for Fe(II)-CO cyt *c*. The time evolution of the ν_4 and ν_3 modes of Fe(II)-CO cyt *c* Raman spectrum is shown in Figure 7.5. Spectra collected immediately subsequent to laser photolysis (t = 1.5 μs) are quite similar to those observed with Fe(II)-CO MP8, showing a large shift of ν_4 to lower frequency (1357 cm^{-1}), with a ν_3 mode at 1463 cm^{-1} consistent with the formation of the five-coordinate photolyzed intermediate. The time evolution of the cyt *c* spectra, however, appears to be qualitatively different from that of photolyzed Fe(II)-CO MP8; by t = 100 μs, the 1463 cm^{-1} ν_3 band has virtually disappeared into the baseline, even though the ratio of 1357 cm^{-1} (photolyzed five-coordinate heme, and six-coordinate non-CO forms) to 1369 cm^{-1} (6 coordinate Fe(II)-CO forms) signals remains roughly constant. At t = 500 ms, the apparent ratio of five-coordinate/six-coordinate ν_4 signals appears to be very similar to that seen in the MP8 photolysis at t = 500 ms, yet the ν_3 mode that persists at ~ 1463 cm^{-1} in MP8 is not detected in the corresponding cyt *c* spectra. This difference may suggest that a significant fraction of photolyzed Fe(II)-CO cyt *c* binds a sixth axial ligand other than CO between t = 1.5 and 500 μs. By t = 1 ms, the 1463 cm^{-1} mode is seen to grow back partially in the cyt *c* sample. Unfortunately, limited signal to noise in the marker band region makes definitive conclusions regarding the behavior of ν_3 difficult and absolutely precludes the observation of changes in other less intense marker bands (there is a possibility of a slight shift in the frequency of the ν_2 vibration at ca. 1585 cm^{-1} towards shorter wavelengths at $t \geq 100$ μs). The apparent observed time scale for ligand binding is similar to that observed by Jones et al. (using nanosecond transient absorption) for the

Figure 7.3: Static and transient Raman spectra of Fe(II)-CO MP8 in 4.6 M GdnHCl, pH 7. Top row: left: static spectrum, 20 Hz repetition rate; right: transient Raman at t = 1.5 μs; middle row: left: t = 200 μs, right 500 μs; bottom row: left, 1 ms; right: 5 ms.

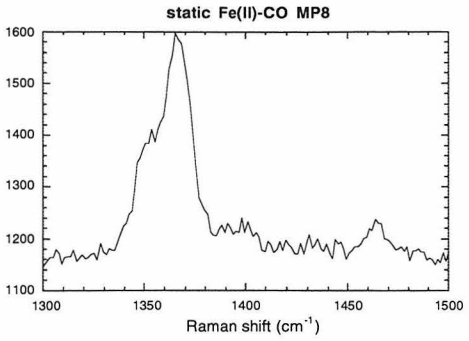
static Fe(II)-CO MP8
1600
1500
1400
1300
1200
1100
1300
1350
1400
1450
1500
Raman shift (cm-1)

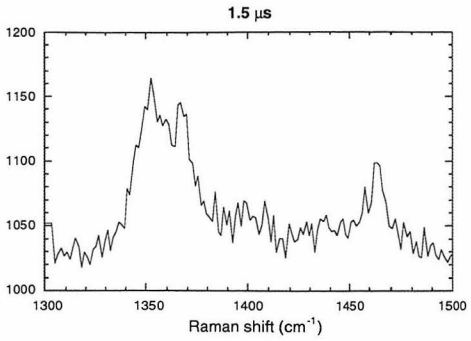
1.5 µs
1200
1150
1100
1050
1000
1300
1350
1400
1450
1500
Raman shift (cm-1)

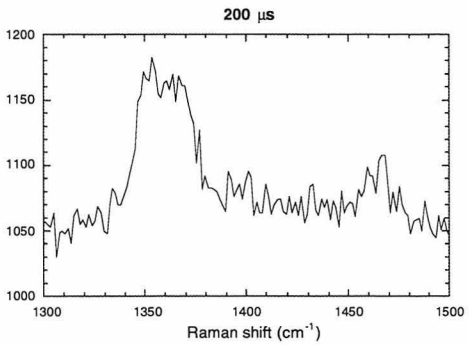
200 µs
1200
1150
1100
1050
1000
1300
1350
1400
1450
1500
Raman shift (cm-1)

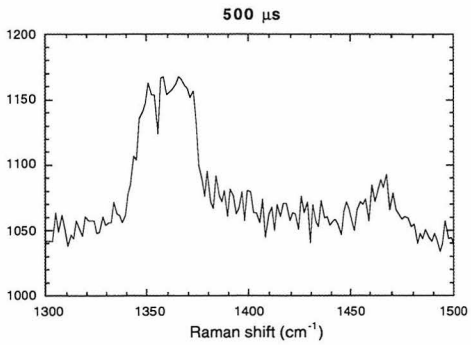
500 µs
1200
1150
1100
1050
1000
1300
1350
1400
1450
1500
Raman shift (cm-1)

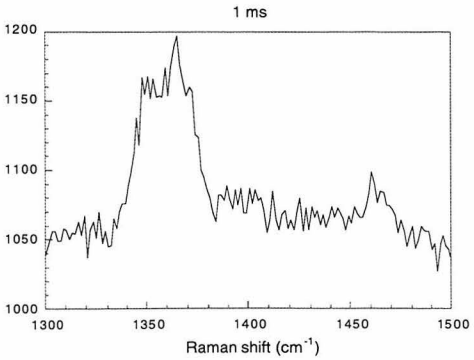
1 ms
1200
1150
1100
1050
1000
1300
1350
1400
1450
1500
Raman shift (cm-1)

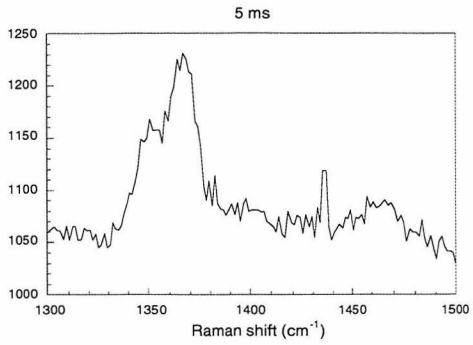
5 ms
1250
1200
1150
1100
1050
1000
1300
1350
1400
1450
1500
Raman shift (cm-1)

Figure 7.4: Transient absorption spectra obtained by photolysis of Fe(II)-CO MP8. Data collected by Jason Telford and Akif Tezcan using a 355 nm excitation (Spectra Physics Nd-YAG DCR-1) and a diode array detection system described in Chapter 4.

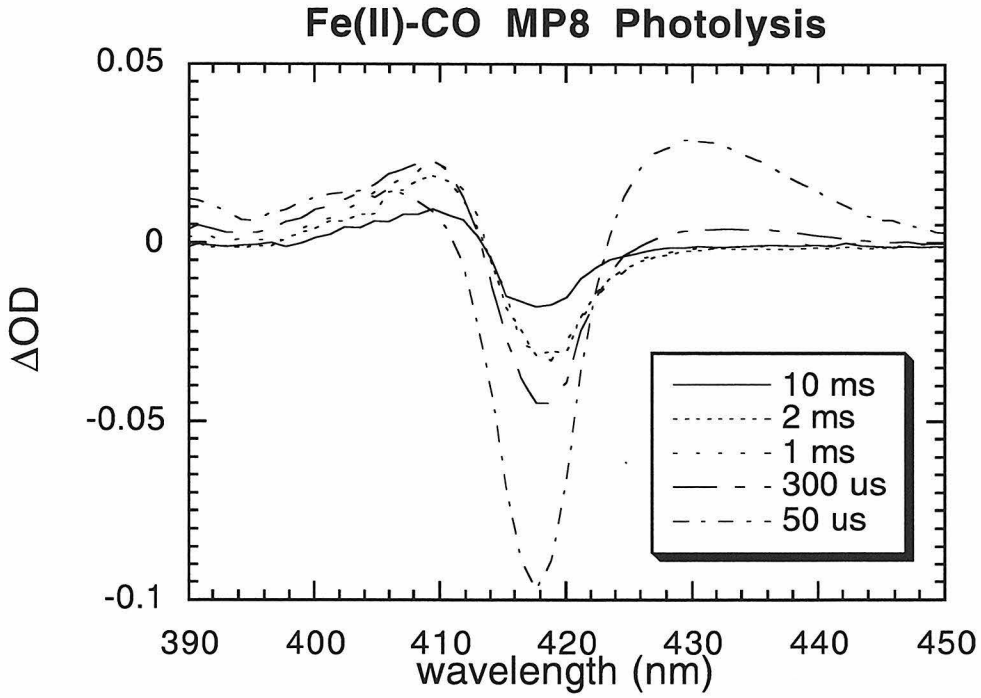
Fe(II)-CO MP8 Photolysis
0.05
0
-0.05
-0.1
ΔOD
390
400
410
420
430
440
450
wavelength (nm)
10 ms
2 ms
1 ms
300 us
50 us

Figure 7.5: Static and transient Raman spectra of Fe(II)-CO h-cyt *c* in 4.6 M GdnHCl. Top row: left: static spectrum, 20 Hz repetition rate; right; transient Raman at t = 1.5 μs; middle row: left: t = 200 μs, right 500 μs; bottom row: left; 1 ms; right: 5 ms.

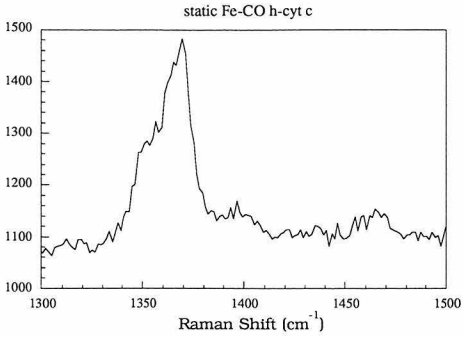
static Fe-CO h-cyt c
1500
1400
1300
1200
1100
1000
1300
1350
1400
1450
1500
Raman Shift (cm-1)

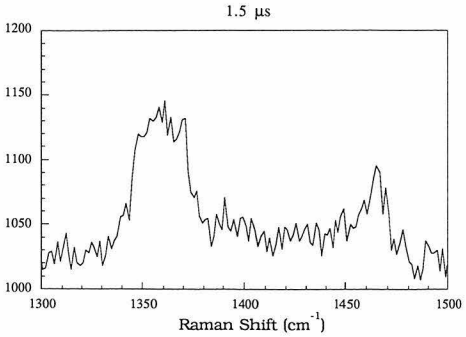
1.5 µs
1200
1150
1100
1050
1000
1300
1350
1400
1450
1500
Raman Shift (cm-1)

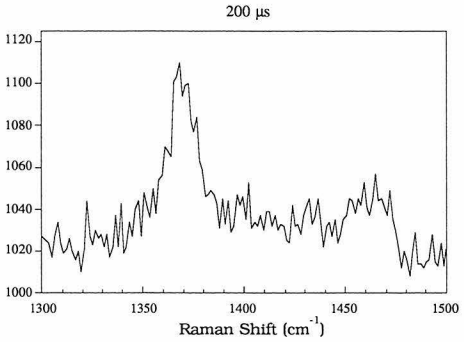
200 µs
1120
1100
1080
1060
1040
1020
1000
1300
1350
1400
1450
1500
Raman Shift (cm-1)

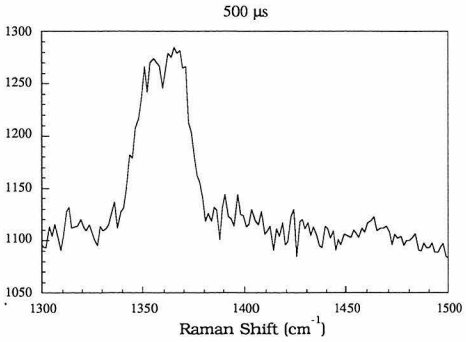
500 µs
1300
1250
1200
1150
1100
1050
1300
1350
1400
1450
1500
Raman Shift (cm-1)

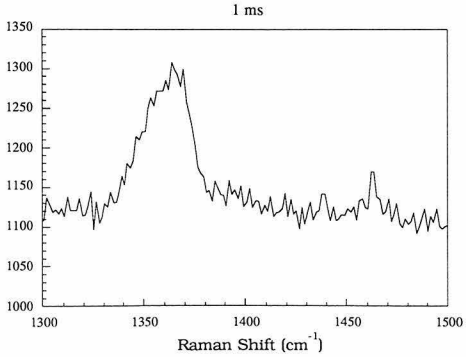
1 ms
1350
1300
1250
1200
1150
1100
1050
1000
1300
1350
1400
1450
1500
Raman Shift (cm-1)

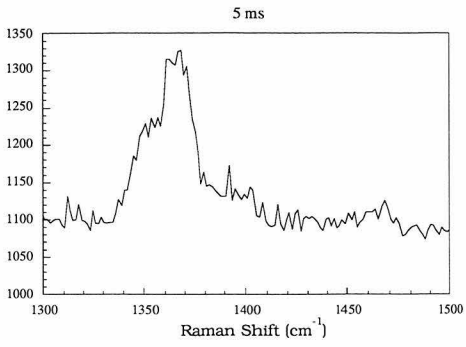
5 ms
1350
1300
1250
1200
1150
1100
1050
1000
1300
1350
1400
1450
1500
Raman Shift (cm-1)

addition of methionine and histidine side chains to the 5-coordinate heme iron.[2] Notably, the bis-histidine ferrous heme *c* of Fe(II) H23MP10 has relatively weak marker band intensities, and generation of a population of bis-histidine ligated forms is consistent with the loss of 1463 cm^{-1} intensity (see Chapter 5). The binding of exogenous ligands such as guanidine was not considered by Jones et al., however, in the absence of information regarding the binding affinity of guanadine for ferrous hemes, this possibility cannot be excluded on the basis of our data. The behavior the photolyzed Fe(II)-CO MP sample argues against simple water binding to the transient 5-coordinate species, since water binding should also occur in the case of the fully solvent exposed MP8 heme.

Conclusions

We have successfully prepared the ferrous carbonmonoxy form of MP8 for use as a model for cyt *c* folding initiated by CO photolysis. The UV-visible and Soret-excited resonance Raman spectra of Fe(II)-CO are similar to those of ferrous carbonmonxy heme proteins. We have applied the method of time-resolved resonance Raman spectroscopy to the study of the photochemistry of Fe(II)-CO MP8, and have achieved time resolution to 1.5 μs, with modest signal to noise. A comparison of the time resolved Raman spectra of samples of Fe(II)-CO MP8 and Fe(II)-CO cyt *c* in 4.6 M GdnHCl shows a small difference in the time evolution of the ν_3 marker band, which may indicate the binding of a sixth ligand. Time-resolved resonance Raman measurements, however, were plagued by poor signal to noise that precluded observation of all but the most intense Raman signals. Therefore, the many out-of-plane vibrations that are correlated with cyt *c* folding in the ferric state remain obscured, and significant improvements in signal to noise are required for their observation.

Experimental Section

Transient resonance Raman spectra were collected using a SPEX 750 M Raman monochromator with a cooled CCD array detector and 406 nm excitation from an excimer pumped dye laser as described in Chapter 5. For optical pumping to initiate CO photodissociation, 532 nm pulses were provided by a Nd-YAG laser (Spectra Physics DCR-1). The beams from the dye laser and the YAG were made coincident by using a mirror that transmits 532 nm light and reflects 406 nm light. The transmitted beam from the YAG and the reflected light from the dye laser were aligned manually. Raman light was collected as described in Chapter 5. The two lasers were synchronized by use of a photodiode that was set to be triggered by the 532 nm YAG pump pulse. The output from the photodiode was sent to a digital delay generator (EG&G) which was configured to send a trigger signal to the dye laser after a predetermined delay time. The minimum time delay between pump and probe was 1.5 μs. Samples of Fe(II)-CO cyt *c* were thermally equilibrated and kept at 40° C during data collection with a thermostatted cuvette cell. One of the walls of the cell was removed to facilitate right angle collection of Raman light. Typical exposure time for transient Raman measurements was 1 minute with laser repetition rates at 10 Hz.

References

(1) Pascher, T.; Chesick, J. P.; Winkler, J. R.; Gray, H. B. *Science* **1996**, *271*, 1558-1560.

(2) Jones, C. M.; Henry, E. R.; Hu, Y.; Chan, C.-K.; Luck, S. D.; Bhuyan, A.; Roder, H.; Hofrichter, J.; Eaton, W. A. *Proc. Natl. Acad. Sci. U.S.A.* **1993**, *90*, 11860-11864.

(3) Williams, S.; Causgrove, T. P.; Gilmanshin, R.; Fang, K. S.; Calendar, B. H.; Woodruff, W. H.; Dyer, R. B. *Biochemistry* **1995**, *34*, 691-697.

(4) Wang, Y.; Van Wart, H. E. *Meth. Enzym.* **1993**, *226*, 319-373.

(5) Spiro, T. G. *Adv. Prot. Chem.* **1985**, *37*, 111-159.

(6) Debois, A. *Biochimie* **1994**, *76*, 693-707.

(7) Hu, S.; Morris, I. K.; Singh, J. P.; Smith, K. M.; Spiro, T. G. *J. Am. Chem. Soc.* **1993**, *115*, 12446-12458.

(8) Hildebrandt, P. In *Cytochrome c: A Multidisciplinary Approach*; R. A. Scott and A. G. Mauk, Eds.; Univeristy Science Books: Sausalito, CA, 1996; pp 285-314.

(9) Kincaid, J. R. *Meth. Enzym.* **1995**, *246*, 460.

(10) Yeh, S.-R.; Takahashi, S.; Fan, B.; Rousseau, D. L. *Nat. Struct. Biol.* **1996**, *4*, 51-56.

(11) Roundhill, D. M. *Photochemistry and Photophysics of Metal Complexes*; Plenum Press: New York, 1994, pp 356.

(12) Gibson, Q. H. *J. Physiol.* **1956**, *134*, 112-122.

(13) Martin, J. L.; Migus, A.; Poyart, C.; Lecarpentier, Y.; Astier, R.; Antonetti, A. *Proc. Natl. Acad. Sci. U.S.A.* **1983**, *80*, 173-177.

(14) Lim, M.; Jackson, T. A.; Anfinrud, P. A. *Science* **1995**, *269*, 962-966.

(15) Terner, J.; Spiro, T. G.; Nagumo, M.; Nicol, M. F.; El-Sayed, M. A. *J. Am. Chem. Soc.* **1980**, *102*, 3238-3239.

(16) Srajer, V.; Teng, T. Y.; Ursby, T.; Pradervand, C.; Ren, Z. *Science* **1996**, *274*, 1726-1729.

(17) Adams, P. A.; Baldwin, D. A.; Marques, H. M. In *Cytochrome c : a multidisciplinary approach*; R. A. Scott and A. G. Mauk, Eds.; University Science Books: Sausalito, CA, 1996; pp 635-692.

(18) Austin, R. H.; Beeson, K. W.; Eisenstein, L.; Frauenfelder, H.; Gunsalus, I. C. *Biochemistry* **1975**, *24*, 5355-5373.

(19) Sharma, V. S.; Schmidt, M. R.; Ranney, H. M. *J. Biol. Chem.* **1976**, *251*, 4267-4272.

(20) Makinen, M. W.; Churg, A. K. In *Iron Porphyrins Part I*; A. B. P. Lever and H. B. Gray, Eds.; Addison-Wesley Publishing Company: Reading, MA, 1983.

(21) Rimai, L.; Salmeen, I.; Petering, D. *Biochemistry* **1975**, *14*, 378.

(22) Spiro, T. G.; Strekas, T. C. *J. Am. Chem. Soc.* **1974**, *96*, 338-345.

(23) Jordan, T.; Eads, J. C.; Spiro, T. G. *Protein Sci.* **1995**, *4*, 716-728.

(24) Woodruff, W. H.; Farquharson, S. *Science* **1978**, *201*, 831-833.